AIX-MARSEILLE UNIVERSITY

Doctoral School: Physics and Sciences of the Matter

LASERS, PLASMAS AND PHOTONIC PROCESSES (LP3) LABORATORY

A thesis submitted in fulfillment of the requirements for the degree of doctor at Aix-Marseille University

Discipline: Physics and Sciences of the Matter
Specialty: Optics, Photonics and Image Processing

Qingfeng LI

Title of the thesis: Double-pulse Laser-induced Forward Transfer

Thesis committee:

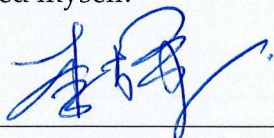|		
Prof. Craig ARNOLD	Princeton University, USA	Reviewer
Dr. Pere SERRA	Barcelona University, Spain	Reviewer
Prof. Maria DINESCU	INFLPR, Romania	Examiner
Dr. Marti DUOCASTELLA	Italian Institute of Technology, Italy	Examiner
Dr. Nicolas BONOD	Aix-Marseille University, CNRS, France	Examiner
Dr. Anne-Patricia ALLONCLE	Aix-Marseille University, CNRS, France	Examiner
Dr. David GROJO	Aix-Marseille University, CNRS, France	Co-Director
Dr. Philippe DELAPORTE	Aix-Marseille University, CNRS, France	Director

National number of the thesis: 2019AIXM0001/xxxxxx

Declaration of Authorship

I, Qingfeng Li, declare that this thesis titled, "Double-pulse Laser-induced Forward Transfer" and the work presented in it are my own. I confirm that:

- This work was done wholly or mainly while in candidature for a research degree at this University.

- Where any part of this thesis has previously been submitted for a degree or any other qualification at this University or any other institution, this has been clearly stated.

- Where I have consulted the published work of others, this is always clearly attributed.

- Where I have quoted from the work of others, the source is always given. With the exception of such quotations, this thesis is entirely my own work.

- I have acknowledged all main sources of help.

- Where the thesis is based on work done by myself jointly with others, I have made clear exactly what was done by others and what I have contributed myself.

Signed:

Date: 12/02/2019.

AIX-MARSEILLE UNIVERSITY

Abstract

Doctoral School: Physics and Sciences of the Matter

Doctor of Philosophy

Double-pulse Laser-induced Forward Transfer

by Qingfeng LI

To solve the limitations of Laser-induced Forward Transfer (LIFT), a double pulse LIFT (DP-LIFT) approach has been developed in this thesis. In this process, a first long pulse laser irradiation creates a melted metal pool and a second ultrashort pulse induces the fluid motion and initiates the jetting transfer. This thesis provides a detailed experimental study on the DP-LIFT process. The influence of double pulse parameters on the jetting phenomena has been carefully studied by means of various observation methods. To predict the jetting behaviors, an energy balanced model has been used. Moreover, we demonstrated that for some configurations of the respective diameters of the two lasers, focused nanojets are generated from the melting pool. Finally, from a fixed thickness of the donor film, debris-free single droplets with diameters ranging from 670 nm to 6.0 μm have been printed with high reproducibility. 2.5 D pillars matrix are printed to demonstrate the potential of the double pulse LIFT method for the fabrication of 3D microstructures.

Acknowledgements

Résumé de thèse en français

1, Résumé

Pour repousser les limites du procédé d'impression LIFT, pour Laser Induced Forward Transfer, une nouvelle approche baptisée LIFT à double impulsion (DP-LIFT) a été développée lors de cette thèse. Une première irradiation laser d'une durée de plusieurs dizaines de microsecondes fait fondre localement le film mince métallique appelé donneur sur toute son épaisseur afin de créer un bain de métal fondu de quelques micromètres de diamètre. Une seconde impulsion ultra-brève irradie ensuite le centre de bain de métal liquide pour induire le mouvement du fluide et initier le transfert d'un volume contrôlé de ce liquide sous forme de jet. Cette thèse fournit une étude expérimentale détaillée du procédé DP-LIFT. L'influence des paramètres d'irradiation sur les mécanismes et la dynamique d'éjection a été étudiée au moyen de différentes méthodes d'observation. Pour prédire les comportements de cette dynamique, un modèle de conservation de l'énergie a été utilisé. De plus, nous avons démontré que pour certaines configurations des diamètres respectifs des deux spots lasers, il était possible de générer des nanojets à partir du bain de fusion. Enfin, pour d'une épaisseur fixe du film donneur, des gouttelettes uniques d'un diamètre compris entre 670 nm et 6,0 μm ont été imprimées avec une reproductibilité élevée et sans débris. Des matrices 2,5 D de micro-colonnes sont imprimées pour démontrer le potentiel de la méthode LIFT à double impulsion pour la fabrication de micro-structures 3D

2, Introduction

Dans la perspective du développement des nouvelles technologies de fabrication additive (AM), la réalisation d'un processus d'impression sans contact avec une résolution submicrométrique et offrant une large fenêtre de procédé est un challenge primordial pour la nanofabrication 3D. Les récents résultats obtenus avec la technologie LIFT font émerger cette approche comme l'un des candidats pour relever ce défi. Son concept de base consiste en l'irradiation laser d'un film mince, le donneur, au travers d'un substrat transparent sur lequel il a été préalablement déposé, à l'état solide [8], de pâte [9] ou liquide [10], afin d'en transférer un petit volume sur un substrat récepteur placé à proximité. Depuis que cette technologie a été introduite par Bohandy et al. [11] en 1986, elle a démontré son fort potentiel pour l'impression de divers matériaux, notamment des métaux purs et des semi-conducteurs en phase solide, ainsi que des encres avec une large gamme de viscosité qui pour la plupart ne peuvent pas être déposées par des méthodes classiques telles que l'impression par jet d'encre. De plus, ce procédé laser permet d'imprimer certains de ces matériaux sous forme de pixels d'une taille minimale de quelques centaines de nanomètres [12, 13].

Ces propriétés uniques ouvrent le champ des applications de l'impression numérique aux domaines de la microélectronique [14, 15], des OLED [16, 17], des capteurs [18, 19], des MEMS [20] ou du génie biomédical [21, 22].

L'amélioration de la technique LIFT est un défi multidisciplinaire qui nécessite une compréhension détaillée : de l'interaction laser-matériau pour le contrôle des mécanismes d'éjection; des propriétés hydrodynamiques de la propagation du jet afin de prévoir sa rupture et la formation de gouttelettes; des propriétés chimiques et physiques du matériau donneur pour le choix des conditions d'irradiation appropriées. Afin d'étudier ces phénomènes, la technique d'ombroscopie résolue en temps est habituellement utilisée. Les limitations en termes de résolution spatiale n'ont cependant permis de n'étudier que des éjections réalisées à partir d'un film liquide épais ou en phase solide. Des tentatives pour visualiser l'éjection induite par laser à partir de films de donneurs minces ont été récemment réalisées [23], mais des études plus détaillées portant sur le transfert de volumes de pico-femto litres sont nécessaires pour optimiser l'impression de divers matériaux. De plus, plusieurs mécanismes à l'origine du processus d'éjection ont été proposés, [12, 13, 24], mais l'importance relative de ces différents mécanismes en fonction de la durée de l'impulsion laser et de l'épaisseur du film donneur n'est pas clairement déterminée. Sur la base de nos connaissances actuelles, nous avons donc proposé de développer une nouvelle approche d'impression de métal en phase liquide à partir d'un donneur solide. L'utilisation de deux lasers permet de contrôler indépendamment les propriétés du donneur et les mécanismes d'éjection. Les objectifs de recherche suivants ont été définis pour mener à bien cette thèse:

- Objectif 1: Etudier les mécanismes d'éjection en LIFT simple impulsion.
  Objectif 2: Développer un nouveau système LIFT double impulsion.
- Objectif 3: Etudier les mécanismes d'éjection en LIFT double impulsion.
- Objectif 4: Explorer la dynamique d'éjection du DP-LIFT et déterminer les paramètres contrôlant la qualité de l'impression.
- Objectif 5: Etudier la génération de nanojet métallique par le procédé LIFT double impulsion.

3. Matériel et méthodes expérimentales

Pour démontrer le potentiel de l'approche LIFT à double impulsion et optimiser son fonctionnement, une analyse complète du procédé DP-LIFT est nécessaire. Ainsi, plusieurs configurations expérimentales ont été conçues et mises en œuvre pour atteindre les objectifs décrits dans la section précédente. Dans cette section, le schéma général de la configuration DP-LIFT est présenté et les méthodes expérimentales mises en œuvre pour réaliser ces études sont décrites.

La figure 1 montre un schéma du dispositif DP-LIFT. Ce prototype a été conçu pour permettre des investigations flexibles des différents aspects du procédé DP-LIFT. Il

est composé de trois parties principales: la partie optique pour positionner précisément les différents éléments du dispositif tels que les faisceaux des deux lasers et la visualisation de l'éjection résolue temporellement; la partie mécanique pour le positionnement, relatif et absolu, des substrats donneur et récepteur; la partie électronique pour gérer la synchronisation des différents évènements.
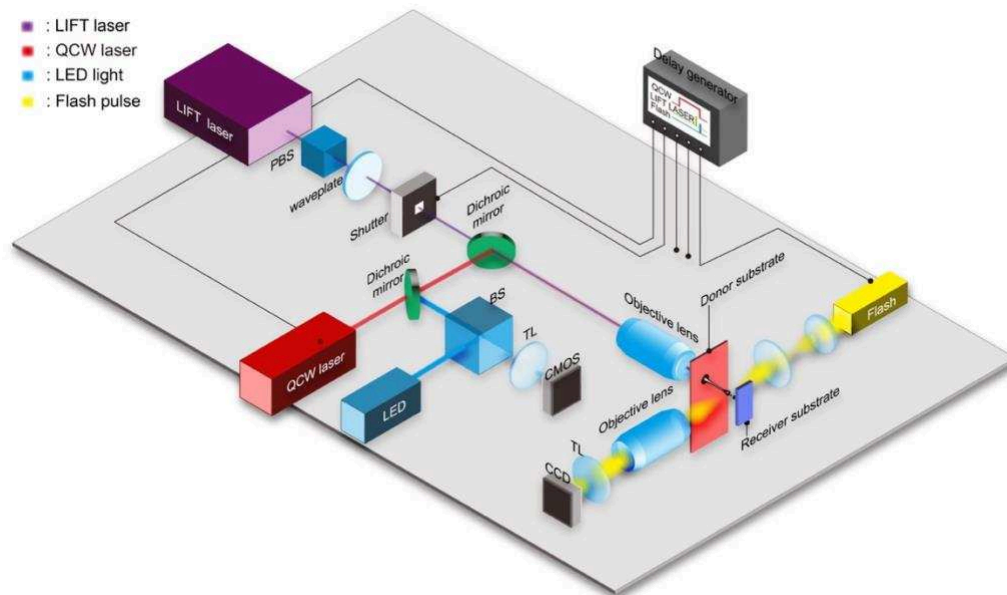

Figure 1 : Schéma du dispositif expérimental DP-LIFT qui consiste principalement de quatre trajets optiques pour positionner les éléments du système, de six axes de déplacements linéaires et d'une électronique de synchronisation de déclenchement des différents évènements du procédé.

Les faisceaux des lasers QCW et LIFT sont combinés par un miroir dichroïque et focalisés sur le substrat donneur par un objectif. Pour que ces deux faisceaux restent concentriques et précisément focalisés sur la surface du donneur, un microscope à lumière réfléchie utilisant le même objectif a été développé. Une diode électroluminescente (LED) est utilisée comme source de lumière de ce microscope, un séparateur de faisceau (BS) réfléchit les lumières LED et transmet l'image de la surface du donneur. Une lentille bi-convexe sert de lentille à tube et forme l'image sur une caméra CMOS THORLABS DCC1645C. Ce microscope « fait maison » permet de contrôler la qualité de la surface du donneur et la position relative des deux points laser focalisés sur cette surface.

Les visualisations des éjections de matière induites par DP-LIFT sont réalisées par la technique d'ombroscopie résolue temporellement. Dans cette thèse, une lampe flash impulsionnelle, d'une durée de 12 ns qui définit la résolution temporelle, est utilisée pour l'éclairage de la zone d'intérêt. Les images sont enregistrées par une caméra CCD montée sur un autre montage microscopique développé durant cette thèse. La synchronisation des deux lasers et de la lampe flash est gérée par un générateur d'impulsion.

Les films donneurs utilisés dans cette thèse ont été préparés soit à l'aide de l'évaporateur thermique au laboratoire soit par PECVD par un industriel. Ils avaient une épaisseur de 100 nm à 1000 nm et étaient déposé sur une lame de microscope d'une épaisseur de 1 mm.

4. Influence de la double impulsion sur le procédé LIFT

Dans cette section, le processus LIFT à double impulsion est expérimentalement étudié dans une configuration combinant une impulsion quasi continue et une impulsion picoseconde. Les dynamiques de la formation et de la propagation du matériau transféré par les procédés DP-LIFT et LIFT simple impulsion sont analysées par imagerie rapide. En comparant les résultats obtenus avec ces deux approches, les caractéristiques uniques de DP-LIFT sont mises en évidence. Ces études sont également étendues à divers matériaux donneurs pour démontrer l'universalité du processus DP-LIFT.

Premièrement, la caractérisation du procédé LIFT à double impulsion, est réalisée par une comparaison systématique avec le LIFT à impulsion unique pour différentes épaisseurs de film donneur, de 180 nm à 620 nm. La distribution de température induite par une seule impulsion picoseconde avec une durée d'impulsion de 50 ps est calculée grâce à une modèle à deux températures (TTM). Comme présenté par la figure 2, pour une fluence de 410 mJ/cm², le front de fusion atteint la surface libre d'un film donneur de cuivre de 180 nm d'épaisseur, alors que pour un film d'épaisseur de 620 nm et une fluence de 2 000 mJ/cm², le front de fusion n'atteint qu'une profondeur d'environ 300 nm.
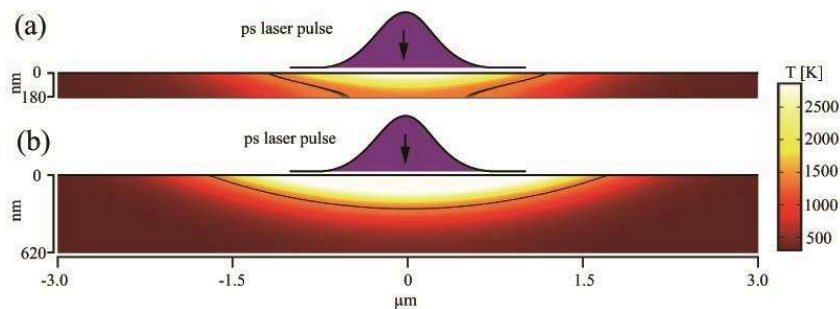
Figure 2 : *Simulation de la distribution en température dans le film donneur de cuivre induite par une impulsion laser picoseconde de 410 mJ/cm2 pour un film de (a) 180 nm d'épaisseur; (b) 620 nm d'épaisseur. Les flèches noires indiquent la direction de propagation du laser.*

En observant les images d'ombroscopie (figure 3) acquises pour différentes fluences avec un délai de 280 ns après l'éjection, la différence des comportements d'éjection dans les deux conditions est analysée. Les figures 3.(a1) – 3.(a3) présentent des éjections d'un film de cuivre de 180 nm induites par une seule impulsion picoseconde. Des éjections dans des situations similaires ont déjà été observées et expliquées [23]: pour les fluences faibles et intermédiaires (F ≤ 720 mJcm²), un pixel unique suivi de

gouttelettes est éjecté, puis le transfert se fait sous forme de jet pour les fluences intermédiaires. Pour les fluences élevées (F ≥ 1000 mJ/cm²), des processus de pulvérisation sont observés. Les mécanismes physiques correspondant à chaque régime sont les suivants: contrainte induite thermiquement pour le transfert d'un pixel, mouvement fluide de la couche fondue pour le régime en forme de jet et évaporation partielle pour le régime de pulvérisation [23]. À titre de comparaison, les figures 3 (a4) à 3 (a6) montrent les éjections induites par le LIFT à double impulsion correspondant à des conditions similaires à celles présentées pour une impulsion unique, à l'exception d'une pré_impulsion du QCW laser d'une durée de 120 µs et d'une énergie de 2,57 mJ qui est utilisé pour faire fondre le film avant l'éjection du matériau. Nous pouvons observer que la dynamique d'éjection est très similaire à celle générée par une seule impulsion laser, quelle que soit la fluence ps laser.
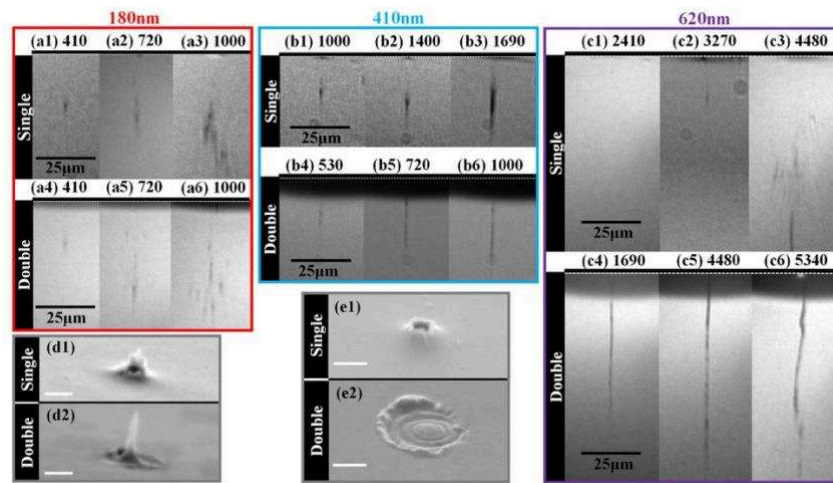

Figure 3 : Images de l'éjection induite par irradiation laser de films de cuivre de différentes épaisseurs: (a) 180-nm, (b) 410-nm, (c) 620-nm. (a1-a3), (b1-b3) and (c1-c3) sont les éjections générées par une impulsion ps unique et pour différentes fluences mentionnées en haut de chaque image. (a4-a6), (b4-b6) and (c4-c6) sont les éjections générées par une double impulsion (QCW + ps) et pour différentes fluences mentionnées en haut de chaque image. (d1), resp (d2), est l'image MEB du film donneur de 410-nm après irradiation par une seule (b1), resp (b6), impulsion (échelle: 1 µm). (e1) et (e2) sont les images correspondantes pour le film de 620nm après une seule (c2) et une double (c5) impulsion (échelle: 2µm).

Nous avons ensuite répété ces expériences avec un film donneur de cuivre d'une épaisseur de 410 nm. Les éjections induites en DP-LIFT, présentées par les figures 3.(b4) -3.(b6), se font sous forme de jets stables, uniformes et longs sur une plage de fluences laser de 530 à 1000 mJ/cm². L'image du donneur après irradiation[2] (figure 3.(d2)) montre un jet qui illustre les mécanismes de dynamique des fluides à l'origine de l'éjection dans cette configuration double pulse [52]. Toutes les images d'éjection ont été capturées avec le même retard de 280-ns, de sorte que jet avec l'énergie déposée. Dans le cas d'une irradiation avec une seule impulsion (figures 3.(b1) – 3.(b3)), nous observons également une éjection en phase liquide. Dans cette configuration, l'épaisseur du film de cuivre (410 nm) étant seulement 2,5 fois plus

grande que la profondeur affectée thermiquement avec une irradiation de 50ps, une valeur de fluence laser peut être trouvée pour induire d'une part la fusion de la couche sur toute son épaisseur et d'autre part la vaporisation d'une quantité appropriée de cuivre à l'interface avec le substrat de verre pour induire une force suffisante pour générer le mouvement du cuivre liquide. Le mécanisme, suggéré par M. Zenou et al. [24], repose sur la formation d'un cratère à la surface du donneur que l'on peut observer sur la figure 3.(d1). Il convient de noter que, même si nous qualifions le processus de transfert de jet, il s'agit en fait qu'une goutte plus ou moins allonger en fonction de la quantité de liquide éjecté.

Pour compléter cette étude, nous avons également utilisé un film de cuivre d'une épaisseur de 620 nm comme donneur. Comme présenté par la figure 2, une fluence laser de 410 mJ/cm², ne permet de fondre de la moitié de l'épaisseur du film, et l'ablation du film à l'interface n'induit pas une force suffisante pour ouvrir le cratère et éjecter le cuivre liquide. Pour une fluence de 3270 mJ/cm² (figure 3.(c2)), le transfert d'une goutte est observé et le cratère observé à la surface du film donneur dans ces conditions est présenté par la figure 3.(e1). Pour des fluences supérieures telles que 4400 mJ/cm² (figure 3.(c3)), le film est entièrement fondu, ce qui permet la formation d'un jet liquide partiellement visible au bas de l'image, mais l'énergie qui a été nécessaire génère également une grande quantité de cuivre vaporisé qui forme un spray derrière le jet. Dans ces cas, le dépôt devient difficilement contrôlable et des débris sont systématiquement retrouvés sur le substrat receveur. En revanche, dans la configuration DP-LIFT, l'énergie de l'impulsion laser picoseconde est systématiquement déposée dans une couche de liquide entièrement fondue grâce à l'irradiation avec la pré-impulsion laser QCW, et cela permet la formation de jets stables pour une large gamme de fluences, comme le montrent les images des éjections des figures 3.(c4) – 3.(c6). Ces jets sont observés avec des longueurs supérieures à 60 µm et la fenêtre de procédé en fluence est comprise entre 1690 mJ/cm² et 4480 mJ/cm². De plus, la figure 3.(e2) présente une image MEB du film donneur après cette double impulsion. Pour ces films épais, on observe les ondulations dues au mouvement du cuivre liquide qui met plus de temps à se solidifier.

L'utilisation de deux impulsions au lieu d'une seule permet donc d'augmenter les fenêtres de procédés en termes de fluence et d'épaisseur du film donneur, et de s'affranchir de la dépendance entre l'épaisseur du film donneur et la durée d'impulsion du laser. Cette technique d'impression DP-LIFT a également été appliquée avec succès pour d'autres métaux (Au, Ag, Ni) et pour des films composés de deux couches métalliques.

5, Dynamique du procédé LIFT double Impulsion

5.1, Influence de la température du film donneur

Dans la section précédente, le processus DP-LIFT a été appliqué avec succès pour générer des nano-jets liquides à partir d'un film donneur solide et imprimer des micro-pixels sur un substrat receveur sans générer de débris. L'optimisation de ce procédé nécessite cependant une étude plus approfondie des mécanismes physiques mis en jeu et de l'influence des différents paramètres. Dans cette section, nous nous sommes donc intéressés au rôle de chacune des deux irradiations sur le contrôle des mécanismes de transfert.

L'objectif de l'irradiation par une impulsion longue (laser QCW) est d'induire une fusion locale du film donneur. Le processus thermique induit dans ce film est décrit par l'équation générale de la chaleur qui donne la température T dans le film en réponse à une source de chaleur Q.

$$\rho C_p \frac{dT}{dt} - \nabla(k\nabla T) = Q, \tag{1}$$

En utilisant des méthodes de simulations numériques, l'évolution de la température du donneur induite par l'impulsion QCW est calculée de t = 0 µs à t = 500 µs et le résultat est présenté par la figure 4. Plus précisément, l'évolution de la distribution latérale de la température latérale dans la région irradiée est cartographiée (figure 4.(a)). Le film est suffisamment fin (1 µm) pour que la température soit uniforme sur toute son épaisseur. La courbe en trait plein sur ce graphique montre la ligne de contour de la région fondue.
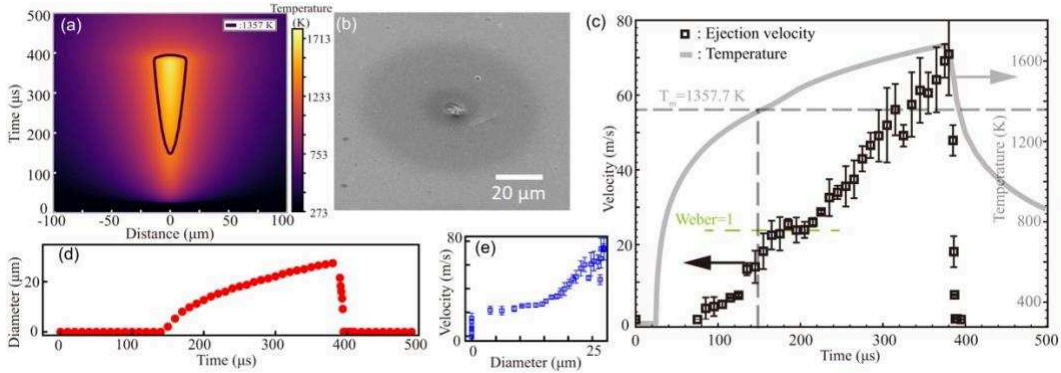
Figure 4 : *Caractéristiques spatio-temporelles du film de cuivre et des éjections durant le procédé DP-LIFT. (a) Evolution spatio-temporelle de la distribution de température dans le film induite par l'irradiation avec le laser QCW. (b) Image MEB du film de cuivre à la fin du procédé. (c) Evolution temporelle de la température calculée au centre de la zone irradiée et de la vitesse d'éjection mesurée pour différents délais QCW-fs. La température de fusion du cuivre (1357.7 K) est indiquée par la ligne horizontale. (d) Evolution temporelle du diamètre de la région fondue. (e) Vitesses d'éjection mesurées en fonction du diamètre de la zone fondue.*

Pour avoir une vue d'ensemble de la zone thermiquement affectée après DP-LIFT, une image MEB de la zone irradiée est présentée en 4.(b). Un disque gris clair de diamètre ≤ 60 µm correspond à la zone chauffée par le laser QCW et un disque gris foncé de diamètre ≤ 20 µm correspond à la zone fondue et resolidifiée. Au centre de cette dernière zone, on peut observer la modification de morphologie induite par la formation du jet. La figure 4.(c) présente l'évolution temporelle de la température du cuivre au centre du spot laser. En se référant au profil temporel de l'impulsion QCW, la température du film de cuivre commence à augmenter à t = 24 µs et la région centrale atteint le point de fusion à t = 150 µs. Sur la figure 4 (c), on peut voir que la température monte jusqu'à sa valeur maximale de 1689 K à t = 383 µs avant de chuter brusquement à t = 395 µs, ce qui conduit à la resolidification du film. Comme le montre la figure 4.(d), l'évolution temporelle du diamètre de la zone fondue au cours de l'irradiation est similaire. Le bain fondu commence à se former à t = 150 µs et le diamètre maximal de 27,4 µm est atteint à t = 383 µs, pour diminuer rapidement et disparaitre à t = 395 µs.

En associant la connaissance de la température du film donneur de cuivre et le diamètre de la zone liquide au cours de l'irradiation QCW, et les observations expérimentales de la dynamique de l'éjection, il devient possible d'étudier l'impact de ces paramètres (température, diamètre) sur les mécanismes d'éjection. Nous avons dons effectué des expériences DP-LIFT pour différents délais Δt entre les deux impulsions laser. Comme le montre la figure 5, les observations résolues en temps des événements d'éjection sont capturées avec des délais de 300 ns et 600 ns après la seconde irradiation laser.
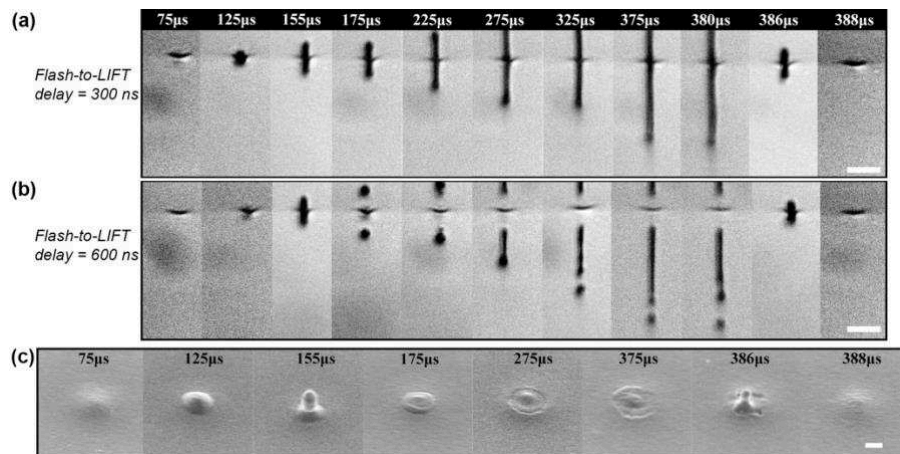
Figure 5 : Images d'ombroscopie des éjections pour différents délais entre les deux lasers acquises avec 300 ns (a) et 600 ns (b) après l'impulsion femtoseconde. Echelle spatiale : 10 µm. (c) Image MEB de la zone irradiée dur film donneur à la fin du DP-LIFT. Echelle spatiale : 2 µm.

Durant l'impulsion du laser QCW qui est utilisée pour chauffer le film de cuivre, le laser femtoseconde est déclenché, avec une énergie de 2 µJ, et un retard t par rapport à l'initiation de l'expérience. Le délai LIFT-flash a d'abord été fixé à 300 ns. Comme le montre la figure 5 (a), le jet semble apparaître à Δt = 125µs. De Δt = 175 µs à 380 µs, la longueur du jet augmente en raison de vitesses d'éjection plus élevées, puis diminue

rapidement jusqu'à ce qu'aucun jet significatif ne soit observé après Δt = 388 μs. Le deuxième délai LIFT-flash a été fixé à 600 ns. Premièrement, les images acquises pour ce retard montrent qu'il n'y a pas d'évolution pour des retards inférieurs à 155 μs ou supérieurs à 385 μs, ce qui signifie qu'il n'y a pas d'éjection se produisant pour ces conditions. Même si un jet semble être initié à Δt = 155μs et Δt = 386μs, il apparait qu'il ne peut pas s'échapper de la surface du donneur. De Δt = 175 μs à 380 μs, on observe une évolution de la morphologie des jets liée à leur rupture et à la formation de gouttes. Ces observations sont cohérentes avec les prédictions théoriques de Notz et al [127], même si le rayon du jet est à l'échelle du micromètre dans nos expériences. Pour faciliter l'interprétation de ces mécanismes, les morphologies de la surface du film du donneur après le processus DP-LIFT sont également présentées à la figure 5 (c). Sur la base des images nous avons également calculé la vitesse moyenne de l'éjection qui est tracée sur le graphique de la figure 4 (c) pour mettre en évidence la corrélation avec l'évolution de la température du film donneur.

Il semble donc que l'impact de la température du film de cuivre sur le processus ne se limite pas à une réponse binaire associée à des films en phase liquide ou non. Ce paramètre joue un rôle important dans la dynamique du processus d'éjection. On observe que la vitesse initiale d'éjection augmente avec l'augmentation de la température. Les paramètres optiques (réflectivité) et hydrodynamiques (tension superficielle et viscosité) étant liés à la température, nous avons utilisé un modèle de bilan énergétique, qui sera présenté dans la section suivante, pour corréler l'évolution de la température aux changements de vitesse d'éjection. Cependant, les variations de vitesse prédites par cette approche sont bien plus faibles que celles observées dans nos expériences (figure 4 .c). Ceci est très probablement dû à l'influence au diamètre de la zone fondue qui n'est pas pris en compte dans nos calculs. Pour établir la corrélation entre le diamètre du bain en fusion et la vitesse d'éjection, nous avons tracé (figure 4.e) les vitesses d'éjection mesurées en fonction des diamètres calculés de métal liquide. De 15 μm à 25 μm, les vitesses d'éjection sont linéairement proportionnelles aux diamètres du bain en fusion. Cela confirme l'importance du diamètre du métal liquide pendant le processus de chauffage par impulsions QCW. Ceci est intéressant sur le plan technique car l'évolution temporelle de ce diamètre au cours du processus DP-LIFT nous permet d'accéder à une large gamme de régimes d'éjection sans modifier les paramètres du laser (énergie, fluence, etc.) ou l'épaisseur du film donneur.

5.2, Influence de la fluence laser sur le DP-LIFT

Dans cette section, l'impulsion femtoseconde est déclenchée avec un retard fixe de Δt = 275 μs, le diamètre du bain fondu est de 20 μm et la température au centre du bain en fusion est de 1590 K selon le calcul numérique. La dynamique d'éjection et la morphologie des gouttes imprimées ont été étudiées pour différentes fluences du laser femtoseconde. Des matrices de gouttes ainsi que des matrices de piliers 2.5D ont été imprimées pour confirmer la reproductibilité du processus.

Afin de prédire l'évolution de la vitesse d'éjection en fonction de la fluence du laser femtoseconde, une équation de la conservation de l'énergie est proposée pour calculer la vitesse d'éjection V_{ej} en fonction des différents paramètres:

$$V_{ej} = \sqrt{\frac{2CA_{femto}[F_{abs}-\rho d_v L_m - \rho d_v C_p(T_v-T)]-\gamma\Delta A)}{\rho d_l A_{ej}}} \tag{2}$$

où A_{femto} est la surface irradiée par impulsion femtoseconde, F_{abs} est la fluence laser absorbée, T est la température du film donneur de cuivre au moment de l'irradiation fs, T_v est la température de vaporisation cuivre, C_p est sa capacité calorifique et L_m son enthalpie de vaporisation, ρ sa densité, d_l est l'épaisseur du film liquide et d_v l'épaisseur du film évaporé. Comme le montre la figure 6, la vitesse d'éjection prédite par ce calcul correspond à celle mesurée, en particulier lorsque la vitesse est suffisamment élevée pour échapper à la surface libre.
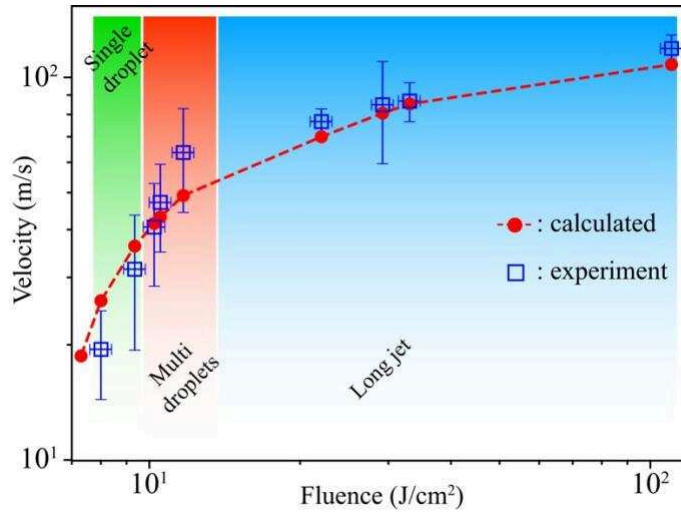

Figure 6 : *Evolution de la vitesse d'éjection en fonction de la fluence du laser femtoseconde.*

5.3 Impression de microstructures de cuivre

En plaçant un substrat de silicium à 50 µm du film donneur, les matériaux éjectés sont collectés pour former motifs 2D dont les diamètres des pixels sont contrôlés en faisant varier la fluence du laser femtoseconde.
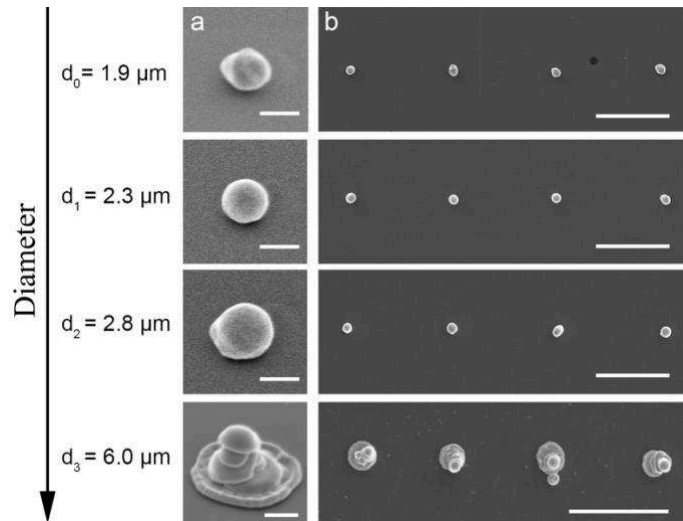
Figure 7 : *Evolution du diamètre des pixels imprimés en fonction de la fluence laser. (a) Images MEB des pixels imprimés pour différentes fluences. Echelle : 2 µm. (b) Images MEB de lignes de pixels. Echelle : 20 µm. Pour chaque ligne la fluence est constante.*

6, Nano-impression digitale

Dans ce chapitre, nous rapportons les phénomènes de nano-jets que nous avons réussi à générer par cette la technique DP-LIFT appliquée à un film de cuivre d'épaisseur micrométrique. La dynamique de ces nano-jets est étudiée par imagerie rapide et le diamètre des jets est estimé en mesurant les diamètres des gouttelettes imprimées. À notre connaissance, il s'agit de la première démonstration de l'impression contrôlée et reproductible par LIFT de gouttelettes de diamètre inférieur à l'épaisseur du donneur. Enfin, nous mettons en évidence que les mécanismes responsables de ce comportement d'éjection à échelle nano sont probablement étroitement liés au diamètre du bain de fusion induit par l'impulsion QCW. La matrice de gouttelettes imprimées est illustrée à la figure 8.
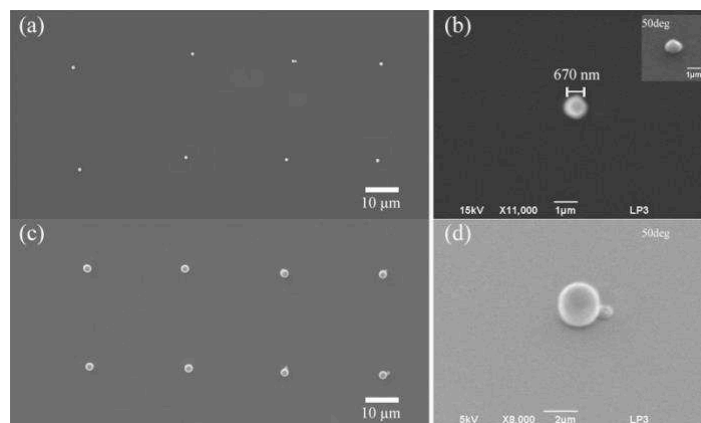

Figure 8 : *(a) Matrices de nano-gouttes et (b) image d'une nano-goutte imprimée avec une impulsion fs de fluence de 3.8 J/cm². (c) Matrices de nano-gouttes et (d) image d'un seul transfert composé une nano-goutte et une micro-goutte imprimées avec une impulsion fs de fluence de 4.8 J/cm².*

7, Conclusions et perspectives

Pour conclure, les objectifs définis au début de cette thèse ont été réalisés. Cependant, les développements ultérieurs de ce procédé D-LIFT reposent sur l'amélioration des connaissances en ingénierie et en physique. Les futures études devraient portées sur les deux points suivants.

- Le premier consiste à approfondir nos connaissances sur la physique du nanojet, car les mécanismes responsables de ce phénomène ne sont toujours pas clairs.

- Le second serait d'étendre l'utilisation de ce procédé à d'autres matériaux que les métaux purs afin d'explorer de nouveaux mécanismes et de pouvoir développer des applications en nano-photonique.

Enfin, d'un point de vue plus technique, le challenge de la nano-impression 3D ne pourra être résolu qu'en développant de nouvelles stratégies pour contrôler les déplacements du prototype (faisceaux et mouvements) afin d'améliorer encore la précision du dépôt d'énergie et la résolution d'impression.

Contents

Chapter 1

Introduction

This chapter mainly provides the research objectives and the outline of the thesis.

Contents

1.1 Microfabrication and Nanofabrication

Even though nano- sciences and technology are still promised to have a tremendous impact on future products, technological equipment, and more generally our daily life, more realistic and prudent projections should be considered for the timescale of this revolution and to bring those concepts into practice. From the experience of the last decades, one should realize that those promised potentials will largely rely on bridging "nano- manufacturing" and "macro- manufacturing" and to produce low- cost products. In terms of micro-products, the main mature developed categories including microelectronics, like micro- optical electronics systems, micro- electronics mechanical systems (MEMS), and micro- optical electronics mechanical systems (MOEMS), depending on their functionalities and working principles. Currently, there has been an enormous amount of literature dedicated to the manufacturing techniques of these micro-systems.

Among those manufacturing technologies photolithography is probably the most widely used to pattern surfaces at the nanoscale (down to 10 nm). In the same category of mask-based technology, nano-imprint lithography [1, 2], microcontact printing [3], and transfer printing [4, 5] appear to be high-resolution and relatively-cheap techniques to realize nanostructures from pre-defined molds or stamps. However, mask based technologies are generally costly, time-consuming processes.

In this thesis, the research is focused on a direct writing (DW) technology. As indicated by the nomenclature, DW methods are capable to perform material pattering without any mask. One conventional DW method is printing small droplets and photochemically solidifying them through cross-linking. Currently, this idea has been commonly used in inkjet printing technologies, which are able to provide droplets with a diameter of several microns. However, it would be difficult to generate small, detailed structures at the nanoscale [6]. Some DW methods are able to provide an ultra-high resolution (sub- 10 nm) such as electron-beam lithography or ion beam lithography [7], however they required expensive equipment, high vacuum environments and are time-consuming.

Indeed, the significant majority of DW techniques are laser- based. Laser-based additive manufacturing (AM) is growing rapidly thanks to the numerous industrial applications such as microelectronics, integrated optics, 3D printing. The implementation of those various demanding applications requires the transfer of a large variety of different materials with high resolution, high speed, high flexibility and full control of the deposited material quality, i.e. morphology and size. So far, several laser-based techniques were developed to address these challenges, such as selective laser sintering (SLS), laminated object manufacturing (LOM) and stereolithography (SL), however each process has its own advantages and disadvantages regarding flexibility, resolution and material limits.
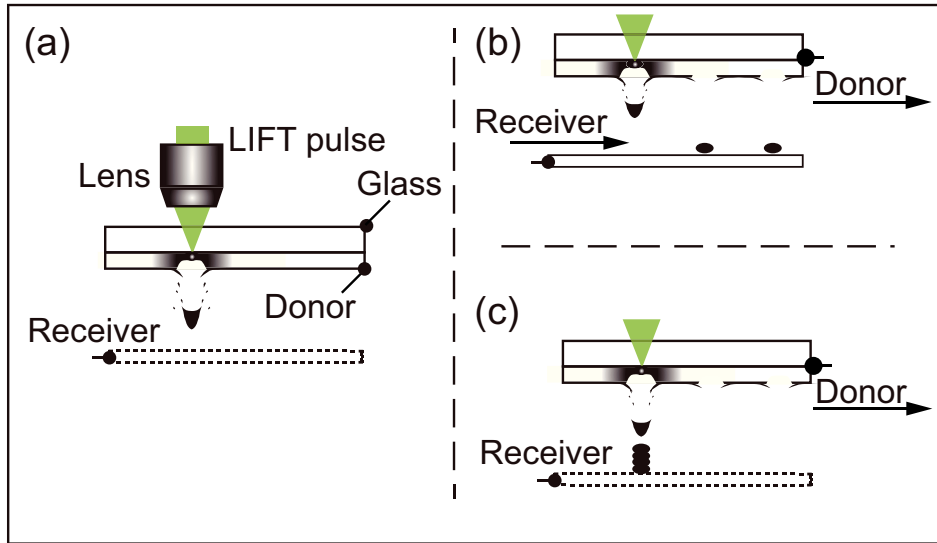
FIGURE 1.1: (a) Sketch of the LIFT process. (b) Printing of 2D array of droplets. (c) Printing 3D pillars

1.2 Laser-induced forward transfer

In the perspective of the AM technologies development, the need for a non-contact printing process with submicrometer resolution and large process windows appears as a key challenge of 3D nanoscale AM. The recent results obtained with the Laser-induced forward transfer (LIFT) technology highlight this approach as one of the candidates to address this challenge. Its basic concept consists in the backside laser irradiation of a thin donor film, in solid [8], paste [9] or liquid [10] state, coated on a transparent substrate to transfer a small volume of the donor material onto a receiver substrate placed nearby, leading to the printing of 2D and 3D structures on the receiver by a pixel-to-pixel approach (see figure 1.1). Since this technology has been introduced by Bohandy et al. [11] in 1986, LIFT has demonstrated its high potential for printing various materials including pure metals and semiconductors in solid phase or inks with a wide range of viscosities, which cannot be deposited using a conventional method such as ink-jet printing. Moreover, this laser printing process allows the deposition of some of those materials as pixels with minimum size down to a few hundreds of nanometers [12, 13]. These unique properties open the range of applications of digital printing to the fields of microelectronics [14, 15], OLEDs [16, 17], sensors [18, 19], MEMS [20] or biomedical engineering [21, 22].

1.3 Research objectives

The improvement of the LIFT technique is a multidisciplinary challenge which requires a detailed understanding of: the laser-material interaction for controlling the ejection mechanisms; the hydrodynamic properties of jet propagation for predicting the break-up of jet and the formation of droplets; the

chemical and physical properties of the donor material for choosing appropriate processing conditions. In order to address those problems, time-resolved visualization of the ejection process is an essential method to investigate the behaviors of the LIFT process and related physical mechanisms. However, due to the challenging visualization conditions in terms of special resolution, time-resolved visualization has only been achieved for the transfer from micrometers thick liquid-film or in solid phase. Attempts to visualize Laser-induced ejection from thin donor films have been recently achieved [23], but more detailed studies focused on the transfer of pico/femtoliter volumes are required to optimize the printing of various materials. Besides, different driving mechanisms of the ejection process have been proposed, depending on the combination of laser pulse duration and the donor film thickness [12, 13, 24]. However, it is not so clear under which conditions the different suggested ejection mechanisms occur. Then, based on our current knowledge, we propose to develop a new approach to print metal in the liquid phase from a solid donor. The use of two lasers allows to independently control the properties of the donor and the ejection mechanisms. Therefore, a list of research objectives is determined and will be investigated in this thesis:

- Objective 1: Investigate the driving mechanisms of single pulse LIFT.

  The LIFT of metal and semiconductor in liquid phase from a thin solid donor film has already been demonstrated and this approach led to the printing of submicrometer droplets [12, 13, 23, 24, 25]. However, the current explanation about the driving mechanisms that initiate the ejection varies from the expansion of the molten material [12], thermally induced stress and partial film vaporization [23, 25] to thermal-induced nozzle [24]. The relation between the donor film thickness and the laser pulse duration is of significant importance, and that strongly limits the process windows of the LIFT process, especially for the thin film required to achieve nano-printing. To have better control of the ejection mechanisms, independently of the film thickness, we proposed a new LIFT process based on a double pulse irradiation. Therefore, a second research objective has been identified as:

- Objective 2: Develop a new LIFT process by using double pulse.

  To overcome the inherent limitation of LIFT mentioned above, a number of complementary techniques have been developed, including the Dynamic Release Layer LIFT (DRL-LIFT), Laser Induced Thermal Imaging (LITI) and Blister-actuated LIFT (BA-LIFT). The main philosophy of those developments is to use an intermediate material to absorb the laser energy and to transform it into a mechanical force to propel the donor material. In this thesis, in order to get rid of the limitations linked to the donor film characteristics to initiate the liquid ejections from solid metal films, we followed a similar philosophy and we developed the double-pulse LIFT process, in which a first long pulse irradiation creates a molten metal pool, and a second short pulse induces the fluid

motion and the material ejection. When the first validation of this new idea is done, a more accurate understanding of the mechanisms behind the double pulse LIFT (DP-LIFT) is required. Therefore, a third research objective has been identified as:

- Objective 3: Investigate the driving mechanisms of DP-LIFT.

A clear understand of the driving mechanisms of DP-LIFT process is mandatory to perform the optimization on the printing performances. The first investigation is based on the comparison between the DP-LIFT process and the conventional single pulse LIFT process. From the unique features of the DP-LIFT experimentally observed and a numerical approach, the driving mechanisms of this technique are identified. However, the use of two lasers provides a high degree of control of the process which is then influenced by several critical parameters such as pulse duration, beam diameters, laser fluences or material properties. The impact of these parameters of the transfer process needs to be characterized and further investigation should be carried on. Therefore, a fourth research objective has been identified as:

- Objective 4: Explore the ejection dynamics of DP-LIFT and find the critical parameters for controlling the printing.

Even though the unique features of DP-LIFT are demonstrated, the awarenesses of the key parameters to control those features and to improve the laser-printing performances is required. As mentioned previously, time-resolved high-resolution observations on the pico/femtoliters liquid transfers have rarely been reported. In order to investigate the influence of both laser parameters on the transfer and the morphologies of the printed structures in DP-LIFT mode of operation, time-resolved observations of the ejection process have been recorded under different conditions. Finally, to downscale the size of the printed structures into the nanometers range, a fifth research objective has been identified as:

- Objective 5: Explore the way to generate a nanojet from a thick donor film through a double pulse LIFT process.
  In this thesis, we want to achieve the printing of nano-pixels from a donor film with micrometer thickness. Experimental studies, taking advantage of the control of the laser fluences, beam shapes, molten pool diameters and delay between the two pulses, have been carried out to reach this goal.

Research objective	Corresponding chapters
Objective 1: Investigate the driving mechanisms of single pulse LIFT.	5
Objective 2: Develop a new LIFT process by using double pulse.	5
Objective 3: Investigate the driving mechanisms of DP-LIFT.	5, 6, 7
Objective 4: Explore the ejection dynamics of DP-LIFT and find the critical parameters for controlling the printing results.	6, 7
Objective 5: Explore the way of delivering nanometers scale jet from a thick donor film through double pulse LIFT process.	7

TABLE 1.1: Summary of the listed research objectives and the corresponding chapters.

1.4   Outline of this thesis

Apart from the introduction provided by this chapter, this thesis is divided into seven additional chapters. Chapter 2 provides an overview of the previous works related to the topic of this thesis. Chapter 3 addresses the theoretical background of laser-material interactions and the numerical approaches related to the DP-LIFT process. Chapter 4 presents experimental setups and methods. A general description of the experimental setup of DP-LIFT process is presented and procedures such as sample preparations and analysis are detailed. As summarized by table 1.1, Chapter 5 to 7 is focused on the studies performed to reach the research objectives previously presented and provide detailed discussions in each chapter. Finally, chapter 8 gives a conclusion of the investigation carried out by this thesis and some perspectives on the future researches linked to the results obtained during this thesis.

Chapter 2

State of the art

This chapter[1] provides a short overview of the existing LIFT technologies based on both solid and liquid donor targets and presents a brief summary of the literature on the spatial and temporal light modulations techniques implemented for the LIFT process. It also discusses some modeling approaches and time-resolved imaging methods used in this thesis. Finally, it presents the motivation for developing the double-pulse LIFT technique.

Contents

---

[1]Parts of the work present in this chapter have been published in the following articles:

- Q. Li, D. Grojo, AP. Alloncle, B. Chichkov, and P. Delaporte, Digital laser micro/nano printing", Nanophotonics (2018) [**Accepted**].

As indicated in Chapter 1, this thesis is concentrated primarily on optimizing the LIFT process. This section provides an overview of the LIFT process and some of the related techniques that have been implemented to enhance the performances of this technology. Section 2.1 describes the basic concepts of LIFT as a function of the state of the state of the donor film: solid or liquid. Section 2.2 introduces some of the optical techniques that have been used to improve the LIFT performances for specific applications. Section 2.3 provides a review of the time-resolved imaging technique which is the main tool for investigating the LIFT process. Finally, section 2.4 presents some of the relevant attempts to model the LIFT process.

2.1 Review on LIFT

As shown in figure 2.1, the LIFT technique [11] relies on the irradiation, using a pulsed laser, of a thin film of absorbing material (the donor) previously deposited onto a transparent substrate (glass). This donor is irradiated through the substrate and the laser interaction processes occurring at the interface induce the ejection of a small amount of the irradiated material and its deposition onto a target substrate (the receiver) set in close proximity. The donor can be a solid film and the pixel is transferred in the solid phase, or a liquid film and a droplet are then deposited onto the receiver substrate. Both laser printing processes from solid or liquid films exhibit numerous advantages, but also some drawbacks which are more or less pronounced depending on the donor material properties. However, we can draw some very general features for each configuration.
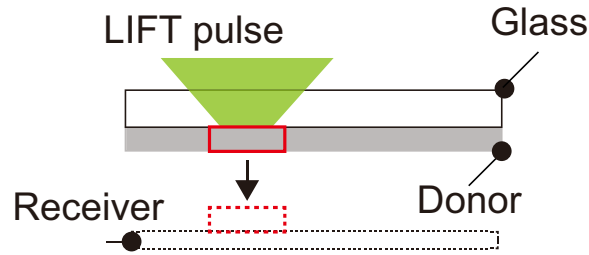
FIGURE 2.1: Schematic illustration of Laser-induced forward transfer technique.

2.1.1 LIFT in solid phase

The process of LIFT in the solid phase is shown schematically in figure 2.2. The physics of LIFT in solid phase relies on the fast heating of the donor film leading to a strong increase of the pressure in the confined volume of the irradiation zone, at the interface between the donor film and the transparent substrate. This effect induces mechanical forces that break the film and propel it towards the receiver, and this ejection dynamic has been extensively studied by means of time-resolved shadowgraphy technique [26, 8]. This approach has two main drawbacks. First, a shock wave is generated at the
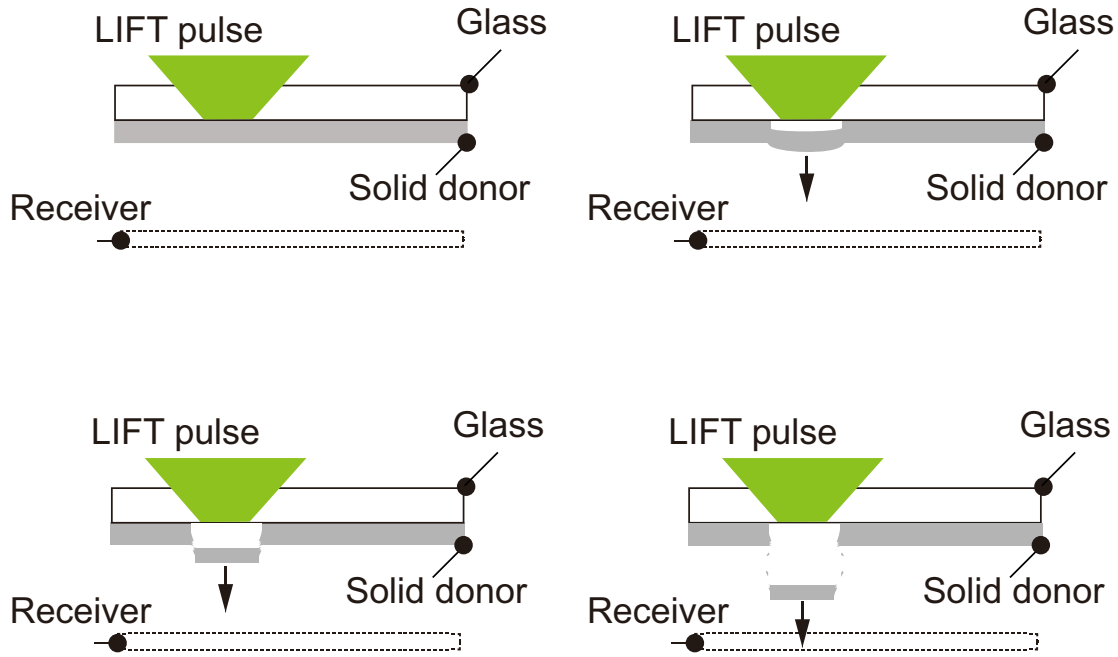
FIGURE 2.2: Schematic illustration of LIFT in solid phase.

surface of the film which propagates in front of the flyer, reflects onto the receiver and can destroy the flyer when crossing it [27]. Second, a significant amount of debris is induced by the laser-matter interaction process and it is also deposited onto the receiver. Different strategies have been developed to prevent the generation of debris and the modifications of the printed material properties induced by the laser irradiation. We can mention the use of an intermediate dynamic release layer (DRL) between the substrate and the donor film to reduce the laser-induced heating of the film [28, 29], or the use of smart beam shaping [30] with over intensity at the edges of the beam for the transfer of thick films. They appear quite efficient for the printing of organic materials [31, 32, 33] but didn't bring significant improvement in the case of inorganic compounds.

2.1.2 LIFT in liquid phase

As shown in figure 2.3, the mechanisms of LIFT in the liquid phase are quite different from those in the solid phase. The laser energy absorbed by the liquid film induces the formation of a cavitation bubble which first expands and pushes the liquid surrounding it. The bubble expansion being mainly oriented perpendicularly to the substrate the fluid motion around it leads to a high-pressure point at the top of the bubble and to the formation of a liquid jet which propagates towards the receiver and forms a droplet on it [10]. These mechanisms, theoretically suggested in 2004 by Pearson et al [34] for a free surface configuration, have been experimentally investigated by few groups by means of time-resolved imaging, or shadowgraphy, of the bubble formation, jet expansion and droplet deposition [35, 36, 37]. This approach allows printing well-resolved droplets down to 15 μm diameter with very good
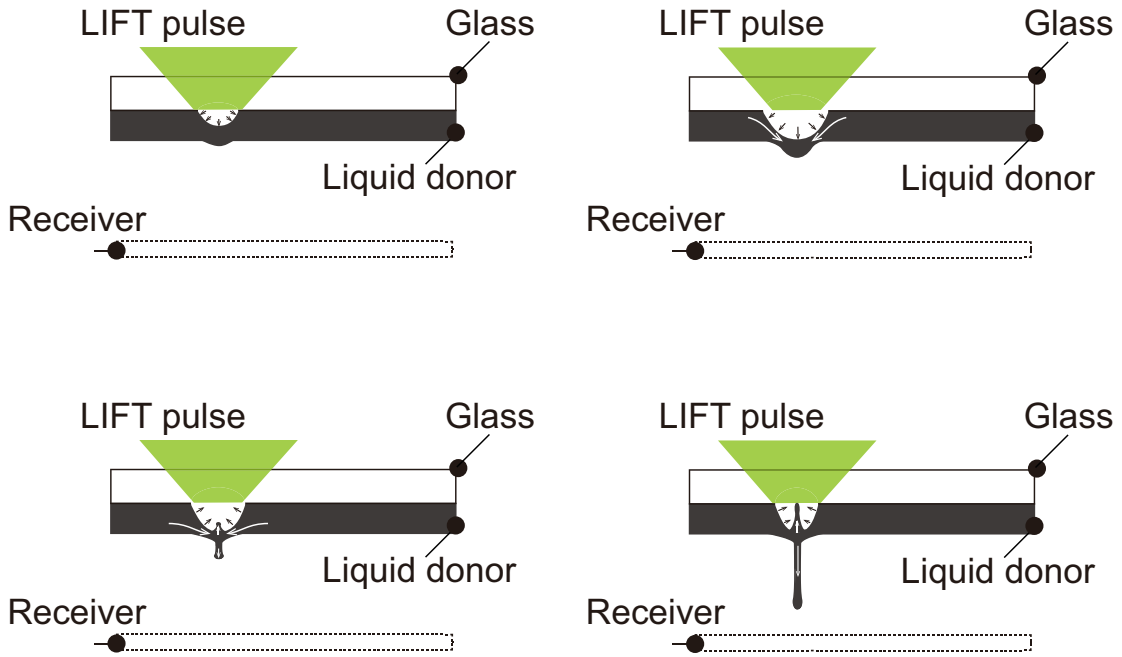
FIGURE 2.3: Schematic illustration of LIFT in liquid phase.

reproducibility and resolution. Moreover, the droplet characteristics are not modified when the distance between the donor and the receiver varies from few tens of micrometers up to two millimeters, and most important no debris is generated onto the receiver substrate. However, the transfer in the liquid phase has also some drawbacks. First, it is quite complex to maintain a liquid donor film with uniform properties (thickness, viscosity, density) during the process due to the evaporation mechanism. Then, a sintering or annealing step of the printed materials is needed when metal nanoparticle inks are transferred to stabilize them and to get their final properties (conductivity). At last, the printing of sub-micrometer droplets requires the reduction of both the laser spot size and the liquid film thickness, and that is almost impossible to obtain uniform liquid films thinner than few micrometers due to the dewetting process. The LIFT in liquid phase approach is especially relevant for printing biomaterial [21, 38, 39, 40, 41] and nanoparticle metal inks [42, 43, 44]. It is worth mentioning the Blister LIFT technique [45, 46] that uses a polyimide film coated between the transparent substrate and the donor film to absorb the laser energy. Basically, the absorption of the laser energy by this polyimide film leads to its fast deformation, without breaking, and that induces the fluid motion and the jet formation. This technique allows to print sensitive materials and to get rid of any risk of contamination from the DRL debris.

2.1.3   LIFT in liquid phase from solid donor

The table 2.1 summarizes the pros and cons of those two approaches of the LIFT process. Since few years researchers [47, 48, 49, 50, 51, 52, 53, 12, 54, 55, 24, 23] have investigated a new technique to combine the advantages of these

Donor film	Cons	Pros
Solid	Generation of debris. Shock wave interaction with pixel. Lack of adhesion. Low resolution of the pixel edges. Limited minimum lateral sizes.	Donor film: stable, easy to handle, very thin film. No post process. Single step printing of large area.
Liquid	Post process required. Donor properties vary over time (solvent evaporation). Ultrathin film not achievable.	Clean printing without debris. Velocity (lines from inks up to 17m/s). High resolution. Less dependence to donor-receiver gap. 3D printing (pastes).

TABLE 2.1: Summary for the pros and cons of the LIFT processes from solid and liquid donor film

two approaches and to address the challenge of digital micro/nano printing. As illustrated by figure 2.4(a), it consists in the irradiation by an ultrashort laser pulse of a thin metal donor film to first melt it and then induce its ejection in the liquid phase, and finally print a micro- or nano-dot on the receiver substrate. It has been observed that the diameter of the printed pixel decreases with the reduction of the donor film thickness [54, 55]. Depending on the laser pulse duration and the donor film thickness, different physical mechanisms are suggested to explain the ejection process. As the first step is the melting of the whole film thickness in the irradiated area, there is a strong relationship between the pulse duration and the film thickness defined by the thermally affected length l_{th}

$$l_{th} = 2\sqrt{D\tau}, \tag{2.1}$$

Where D is the thermal diffusion coefficient of the donor material and τ the laser pulse duration. This relation should not be considered for sub-picosecond pulse duration as the electron-photon relaxation time is of picosecond time scale in metals. So, for given pulse duration, there is only a range of film thickness that can be used to achieve a debris-free printing of micro- or nano-dots. The laser energy must then be tuned to melt the whole film thickness without vaporizing a too large volume of donor material at the interface between the donor film and the transparent substrate. By matching the donor thickness with the laser pulse duration, M. Zenou et al. [24] have achieved a stable and highly directional transfer of metal droplets over a rather large range of donor-receiver gap (> 400 μm) [56]. The driving mechanism they have proposed is called thermally induced nozzle (TIN). The main idea of this approach is to irradiate the film with laser energy allowing the melting of almost all the donor thickness, and then, the fast
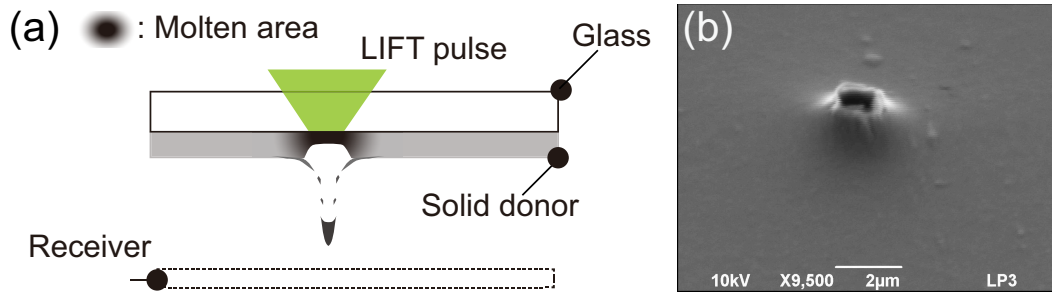
FIGURE 2.4: (a) Schematic illustration of LIFT in liquid phase from solid film. (b) SEM image of a copper donor film after an ultrashort pulse irradiation showing the formation of a thermally induced nozzle (TIN)

expansion of the heated metal breaks the non-melted surface of the film and forms a nozzle from which is ejected a liquid droplet. Figure 2.4(b) shows an SEM image of the donor film after the laser irradiation and the transfer process where the thermally induced nozzle is clearly visible.

R. Pohl et al. [23] also printed micro-droplets by means of picosecond laser irradiation of metal donor films with thicknesses of few hundred of nanometers. They suggested different ejection mechanisms depending on the laser fluence. At low fluence, a cap ejection is observed, driven by the relaxation of thermal stresses induced by laser-induced heating. When the laser fluence increases thermal processes prevail, leading to the liquid jet formation, and at last, for higher fluences, they observed the vaporization of the film and the uncontrolled generation of large amounts of droplets. Both, cap ejection and jet formation mechanisms are attractive to print metal structures, but it appears difficult to avoid the deposition of unwanted satellites around them.

2.1.4   Outlook

In order to fully benefit of all the advantages of LIFT from a liquid film, this thesis proposes a new method, the double pulse LIFT, which relies on the use of two lasers. As presented in figure 2.5, a first quasi-continuous wave (QCW) laser, operating in long pulse duration mode, irradiates the solid donor film through the transparent substrate in order to reach the melting temperature and thus to locally form a liquid film. Then, a second short pulse laser irradiates the central part of this area and that induces the formation of a liquid jet and the printing of a droplet on the receiver substrate. When cooling, this metal droplet solidifies on the substrate. Figure 2.5(b) presents an optical microscopy image of the processed area of the donor film after solidification, the bright contour indicates the solidified molten pool and the central dark spot indicate the area irradiated by the short pulse. This novel technique allows to independently control the phase change of the donor film with the QCW laser irradiation and the transfer process in a liquid phase with the ultrashort laser pulse.
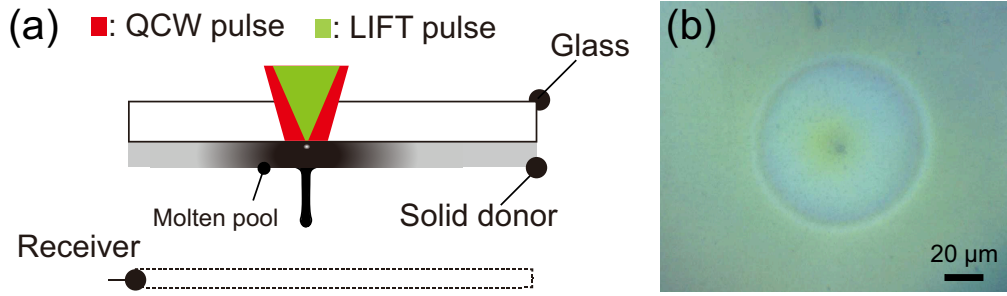
FIGURE 2.5: (a) Schematic illustration of double-pulse LIFT (DP-LIFT) technique. (b) Optical microscope image of the processed area on the donor film after DP-LIFT process.

2.2 Temporal and spatial light modulations and LIFT

The control of the LIFT process with a high degree of precision requires the development of irradiation strategies that permit the deposition of the laser energy at the desired temporal and spatial scales. Recent optical technologies allow flexible manipulation of laser pulse characteristics, including its temporal shape, spatial distribution, spectral content, and polarization state. This thesis is benefited from some of those concepts, therefore in this section, an overview of LIFT related temporal and spatial light modulations researches are provided.

2.2.1 Spatial light modulation for LIFT

Traditionally, LIFT is performed with Gaussian [57] or Top-hat beams [58] that enables the fabrication of patterns through the successive deposition of voxels with computer controlled positioning accuracy. However, it has also been demonstrated that one can deposit voxels with the specific shape of the incident beam. A basic setup of such configuration consists in a pulse laser, a mask, and a lens, which allows the mask pattern to be imaged on the donor layer and the transfer of a pixel with a predefined shape [30]. A more sophisticated way to shape the energy repartition in the laser beam relies on the use of spatial light modulators (SLMs). These devices provide accurate control of light, allowing the creation of two-dimensional light patterns with computer-control characteristics. Depending on the modulation mechanism, SLMs can modify either the phase or the amplitude of the light transmitted or reflected by the device. Currently, two types of SLMs are used for computer-controlled high-speed laser patterning. One is based on a MEMS technology with a large number of micromirror arrays [59], and the other one used a liquid crystal SLM (LC-SLM) technology [60].

These SLMs techniques have been applied for transferring solid films as well as paste films with any arbitrary 2D shapes and directly achieve the designed functionality. For instance, Auyeung et al used a Digital Micro-mirror Device (DMD) for spatial beam shaping, [61, 62, 63] to print pixels whose geometry was changed in real time between each laser shot. The application
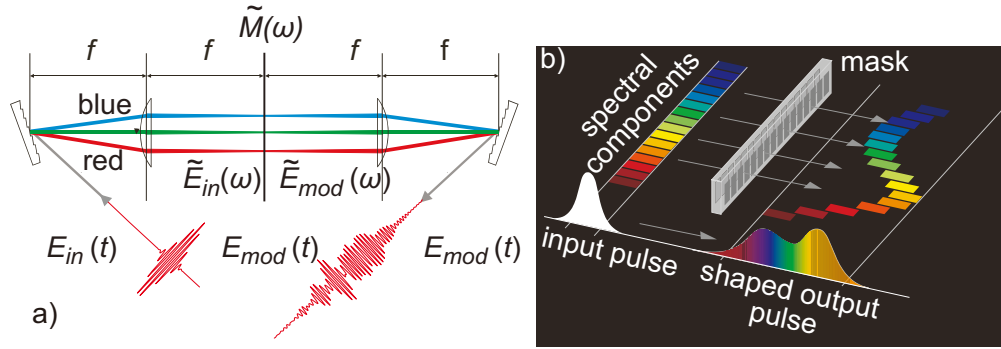
FIGURE 2.6: (a) Schematic illustration of Fourier transform femtosecond pulse shaping. (b) Schematic illustration of shaping the temporal profile of an ultrashort laser pulse by retardation of individual wavelength components of the spectrally dispersed beam. The LC-SLM is located in the Fourier plane. [66]

of Liquid- crystal spatial light modulator (LC-SLM) in LIFT domain has also been reported by Pohl et al [64]. In contrast to DMDs that only perform binary intensity modulation, an SLM offers full grayscale intensity modulation when used in a cross-polarization setup.

Besides, other beam shaping techniques such as Bessel and annular beams are also worth to take into account for LIFT applications [65]. For instance, the "non-diffracting" behavior of Bessel beams results in a long depth of field, which can be used to increase the tolerance of the focal plane position during material processing especially when a high numerical aperture (NA) lens is used and a smaller beam waist is required. Similarly, annular beams provide the advantage to create novel structures in materials and improve micromachining features.

2.2.2   Temporal light modulation for LIFT

Temporal shaping of laser pulses has been proven to be an effective technique to control a variety of physical and chemical processes [67]. During the laser material processing, primary processes induced by ultrafast laser radiation involve nonlinear electronic excitation, energy transfer to vibration modes, and phase transitions that occur on fast but material dependent time scales. Thus temporal energy control may facilitate synchronization between light and material response, leading to an optimized control of the laser energy deposition [66]. In practice, temporal shaping (tailoring) on a laser pulse can be achieved by programmable pulse shaping techniques [68], and the Fourier transform pulse shaper is a typical approach to achieve such temporal pulse modulation. As illustrated in Figure 2.6(a), the incoming ultrashort laser pulse is spectrally dispersed and the frequency components are re-collimated by a focusing optical element with a focal distance f. Therefore, the spectral components can be modulated individually by placing a linear mask into the Fourier plane. The laser pulse is reconstructed by performing an inverse Fourier transformation back into the time domain, resulting in modulated pulse temporal profiles as depicted schematically in Figure

2.6(b). Both LC-SLM and DMD can be used for manipulating the relative retardation of spatially dispersed frequencies. In the LIFT domain, Klini et al [69] have to use the temporally shaped femtosecond laser pulses to control the size and the morphology of micron-sized metallic structures obtained by LIFT process. Moreover, for nanosecond laser pulses temporal energy control in a longer timescale can also be achieved based on the master oscillator power amplifier (MOPA) techniques. With the temporal shaped pulse, more flexibilities have been provided to the laser-material-processing [70, 71]. In the LIFT domain, Narazaki et al [72] succeeded to use two nanosecond pulses to have more precise control of the temperature and the stresses induced by the laser irradiation in the donor film.

In this thesis, we have developed the double pulse strategy to provide an accurate control the temporal energy distribution (microsecond pulse + femtosecond & picosecond pulse), and its unique features on LIFT process will be discussed in the following chapters.

2.3 Time-resolved imaging

To investigate the transient dynamics process such as LIFT, time-resolved imaging techniques are required. To date, high-speed cameras and pump-probe imaging are two conventional techniques that can be applied. However, even though the theoretical maximum frame rate (100 Mfps) acquisition has been proven experimentally accessible [73], ultra-high frame rate (> 50 Mfps) cameras with acceptable spatial resolution is lacked on the market. Thus, pump-probe or laser-synchronized shadowgraphic imaging is widely used to investigate the dynamics of the LIFT process. The typical configuration of those experiments consists in a pump source which initiates the LIFT process and a probe source which is synchronized with the pump one by either an optical (fiber) delay line or an electronic delay generator. The probe-illuminated plane will be imaged by the combination of an objective lens and its tube lens or simply by a macro-lens on to the imaging sensor (CCD, CMOS). Thus the spatial resolution of such visualization setup is determined by the numerical aperture (effective numerical aperture) of the objective lens (macro-lens) as well as the pixel sizes of the imaging sensors. And the temporal resolution is determined by the pulse duration of the probe source. A short review of the relevant literature is provided in this section.

2.3.1 Review on LIFT related time-resolved imaging

For ejection processes of liquid phase LIFT from a solid donor, shadowgraphic investigations have performed by few groups recently.

Duocastella et al. [74, 10] investigated the ejection dynamics of the LIFT process of liquid donor film with a thickness of around 20 μm. A pulsed Nd: YAG laser (355 nm wavelength, 10 ns pulse duration) was used for LIFT processing. The time-resolved observation is based on a gated charged-coupled device (CCD) camera. The CCD camera (ANIMATER-VI from ARP France)

had a resolution of 288×385 pixels, 8 bits dynamic range, and it was intensified by a microchannel plate (MCP). Its triggering was delayed respective to the laser pulse by a pulse generator. A single image was taken for every laser pulse with an integration time of 100 ns which defines the temporal resolution of this experiment. These time-resolved images of the transfer process acquired from the side view have shown that first a vapor bubble is generated in the liquid layer by the laser irradiation and that the fast expansion of this bubble can evolve into different situations depending on various parameters such as laser fluence and liquid properties. In these experiments, ejection velocities varying from 25 m/s to 300 m/s are reported.

Papazoglou et al. [75] investigated the ejection dynamics of the LIFT process of solid InO_x with a thickness of 200 nm. The time-resolved observation was based on the digital synchronization of the pump and probe lasers. A KrF excimer laser (248nm), with a pulse duration of $\sim$0.5 ps and pulse energy of 10 mJ/pulse, was used as the pump laser. A second XeCl excimer laser, with a pulse duration of 30 ns and wavelength of 308 nm, was used as the probe laser. This 30 ns pulse duration of the probe laser defines the temporal resolution of this experiment. For LIFT in this solid phase, high-speed images of the transfer process suggest that the ejection is driven by a shockwave with velocities of 400 ± 10 m/s. Boutopoulos et al. [37] investigated the transfer of silver nanoparticle ink with a thickness of 5.5 μm. With a similar strategy of time-resolved imaging, the digital synchronization of pump and probe lasers were used. A pulsed Nd: YAG laser (266-nm wavelength, 10-ns pulse duration) was used to initiate the transfer and a second Nd: YAG laser (532 nm wavelength, 10 ns pulse duration) was used as the probe laser. In order to improve the image quality and avoid inference patterns, a fluorescence dye (rhodamine solution) set in a transparent container was used to convert the probe laser into an incoherent light emitted from the dye. This approach was introduced for the visualization of the LIFT process in the solid phase by Fardel et al. Fardel et al. [26]. High-speed images confirmed that the jetting behavior was initiated by an expanding cavitation bubble generated in the ink layer near the surface of the transparent substrate and expanding towards the ink-free surface. Ejection velocities from 9 m/s to 80 m/s were observed. With similar time-resolved imaging setup, Pohl et al. [23] investigated the ejection dynamics of pure metals such as copper and gold. Based on their shadowgraphic observation performed with a temporal resolution of 6 ns, a detailed classification of the different ejection regimes have been provided.

Brown et al. [76] investigated the ejection dynamics of blister-actuated LIFT (BA-LIFT) with a typical 10 μm thick ink donor film. Liquid ejection is initiated by focusing a pulse from a frequency-tripled Nd: YVO_4 laser (355 nm wavelength, 20 ns pulse duration) on the polyimide layer. The time-resolved observation was based on a fast plasma discharge lamp (HSPS Nanolite), whose 25 ns pulse duration defined the temporal resolution of the observations. The observation revealed that the expanding gas trapped between the polyimide layer and the donor substrate induces the displacement of the ink-free surface (135-200 m/s) and creates a high aspect ratio liquid

jets. With similar time-resolved imaging setup, Biver et al. [77] investigated the dynamics of the high-speed multi-jets formation from silver nanoparticles ink films.

At last, based on time-resolved shadowgraphy and scanning-electron microscope (SEM) images Unger et al. [51] investigated the femtosecond LIFT from a 60 nm thick gold film. The results suggest that the transfer dynamics is linked to the laser-induced detachment of a melted dome-shape film. When the deformation of the film occurs, lateral capillary forces drive the melted film toward the center and form a high-aspect ratio nanojet at the free-surface. This proposed explanation is supported by SEM observation that proves the existence of a counter-jet. The ejection dynamics occurs with a time scale of a few hundred nanoseconds.

2.3.2 Summary

Those presented literature above is not intended to be exhaustive but covers the typical time-resolved techniques that have been used to investigate the dynamics of the LIFT process. Spatial and temporal resolutions are critical to performing an accurate characterization of the ejection dynamics, especially when the ejection volume downscale into pico- femtoliters. Meanwhile, good contrast of the image is also required to perform quantitative measurements and gain a deeper understanding of the hydrodynamic processes.

2.4 Modeling

The LIFT process can mainly be described by physical phenomena related to two fields of physics: the condensed matter physics for laser-matter interaction and the fluid mechanics for the subsequent matter ejections. Therefore, several numerical simulations have been developed to investigate some steps of this process in order to obtain a better understanding of the relative importance of the various mechanisms of LIFT. This section provides an overview of those LIFT related modeling approaches.

2.4.1 Review on LIFT related modeling

To investigate the processes of heating and melting occurring in the femtosecond laser-irradiated metallic films (Au, Zn, Cr) under the conditions of stress wave generation, Shugaev et al. [78] proposed to analysis the dynamics at the early stages of LIFT process based on a two-temperature model (TTM) which takes into account the laser-generated stress waves. They have point out that melting by itself cannot trigger a fast directional transfer of matter from a donor substrate to an acceptor one, and that is the strong pressure waves caused by instantaneous heating and subsequent wave which finally results in the formation of tensile stress in the middle of the film that induces the film detachment. Their later works [79] proposed a thermoelastoplastic modeling to estimate the height of microbumps produced by nanosecond laser irradiation of solid thin films. Contrary to femtosecond laser pulses, in

nanosecond pulse regimes, stress waves across the film are weak and cannot induce film damage. The main role in laser-induced dynamics of irradiated films is played by radial thermal stresses which lead to the formation of a bending wave propagating along the film and driving the matter towards the center of the irradiation spot.

Also, by taking into account both thermal and hydrodynamics process in the nanosecond laser-irradiation regime, Seifert et al. [80, 81] reported a numerical approach targeting not only the early stages of the formation but also the ejection of liquid gold droplets using the Navier-Stocks equations. It has been shown that the formation of small metallic droplets is a hydrodynamic phenomenon that mainly depends on the amplitude of the inertial forces and surface tension acting on the Au droplets. Their further results show that the ejection and formation of the droplets not only depends on the ratio between the melting dynamics and the surface tension forces but also on the absolute value of the surface tension itself. If the latter is too low, growth does occur, but ejection does not. If the surface tension is too large, droplet formation cannot be considered. Willis et al. [82] introduced a two-dimensional ax-isymmetric numerical model based on the volume of fluid (VOF) method. This model took into account laser-induced heat transfer, phase change, and fluid flow processes in the thin film (1 μm). Time-resolved studies of the evolutions of melting front and of the profile of the free surface were modeled for a nanosecond (7 ns) regime LIFT condition. It was found that the volumetric expansion occurred shortly after the end of the laser pulse and subsequently induced the surface deformation. This expansion process leads to the formation of protrusions at the center of the laser spot which remains after solidification.

In femtosecond laser-irradiation regime, by taking the full laser-induced transfer process into account, Anisimov et al. [83] reported a numerical approach to simulate the mechanisms of film peeling induced by the irradiation with an ultrashort pulse ($\sim$10 fs to 1 ps) of a film with a thickness smaller than the laser heating layer. The model combines a two-temperature model (TTM) for the simulation of the absorbed energy redistribution from the skin layer across the film as well as the transition from a fast thermal stage to the dynamics of film detachment and the classical Molecular Dynamics (MD) method to model the dome growth. The latter approach took into account the capillary effects and the crystallization of the dome and then the one of the jet, as well as the competition between the jet crystallization process and jet breakup into droplets.

Considering the full LIFT process and with the objective to define a criterion that could characterize the printing behavior, Brown et al. [45] and Turkoz et al. [46] investigated the ink jetting behaviors of blister-actuated LIFT (BA-LIFT) based on the finite volume (FVM) and the volume-of-fluid (VOF) methods. It was reported that the driving mechanisms are initiated by the laser-induced rapid formation of blisters on polyimide films at the early times. Then, the blister boundary remains static and no longer exchanges energy with the fluid. However, the residual kinetic energy within the ink enables its forward flow and development into a free-surface jet. They also

characterized different ejection regimes (zero, single, or multiple drops) by using dimensionless parameters defined from the process parameters and measured ink rheology, which provide guidelines to achieve a controllable and reliable printing.

2.4.2 Summary

When we consider the different strategies developed to model the LIFT process, one can observe that depending on the LIFT conditions (pulse duration, donor thickness and etc.) the main physical mechanisms driving the material ejection are different and then the numerical studies developed to model the LIFT process take into account a large set of contributions. Moreover, as many alternatives to the original LIFT process were currently developed, some approaches might involve one or several dynamics processes and new parameters should be taken into account.

Chapter 3

Laser-material interaction and modeling

This chapter mainly provides an introduction of the laser-matter interaction in the framework of double-pulse LIFT. We discuss the governing physics that describes the absorption of laser pulse over a large pulse duration range, the subsequent thermalization of donor film and the resulting properties which influence the dynamics of the LIFT process. Finally, numerical models to simulate the thermal distributions induced by QCW pulse, as well as ultrashort pulse, are proposed.

Contents

3.1 Optical properties

3.1.1 Optical properties of solids

Laser-induced processing of materials always starts by light-matter interaction, and it is essential to describe this physical process with an appropriate approach in order to achieve a realistic simulation of the full process. For solids processed by ultrafast laser, light will generate elementary excitations including inter- and intra-band electronic excitations, phonon excitations and etc. Before any further discussions on the microscopic models that describe the optical phenomena observed in solids, it should be clarified that those models are often be classified into three general categories [84]:

- Classical

- Semi-classical

- Fully quantum

In the classical model, both the medium and the light are described with the classical physics approach. The light is treated as an electromagnetic wave and the atoms or molecules are modeled as classical dipole oscillators. This model provides a starting point to describe the general optical properties of a medium, especially the main effects due to the free electrons and the phonons.

In the semi-classical model the medium is described with quantum mechanics but the light is still considered as a classical electromagnetic wave. An example of this approach is the treatment of interband absorption, in which the absorption coefficient is calculated using Fermi's golden rule, which requires the knowledge of the wave functions of the quantum levels of the atoms, but treats the light-matter interactions as an interaction between the quantum levels of an atom and a classical electric field.

Finally, the fully quantum model is the realm of quantum optics. One uses this approach implicitly when referring the light as a beam of photons or draw Feynman diagrams to represent the interaction processes. However, in the equations used to describe the light-matter interaction process, the light is generally treated classically and only the atoms are described with the quantum model. Therefore, the quantitative description of light-matter interactions is performed with semi-classical modeling.

For solid materials, as shown in figure 3.1, highest valence band (VB) and lowest conduction band (CB) are considered. Absorption or emission of photons with different energies hv is indicated by straight lines. Oscillating lines indicate non-radiative relaxation processes. Inter-band transitions VB $\rightarrow$ CB take place if $hv \geq E_g$. For insulators, band-gap excitations are located in the ultraviolet (UV), and semiconductor band-gap excitations also cover the near-infrared (NIR) and visible (VIS) spectra. By applying the law of energy conservation to this interband transition process we have:

$$E_f = E_i + hv,\tag{3.1}$$
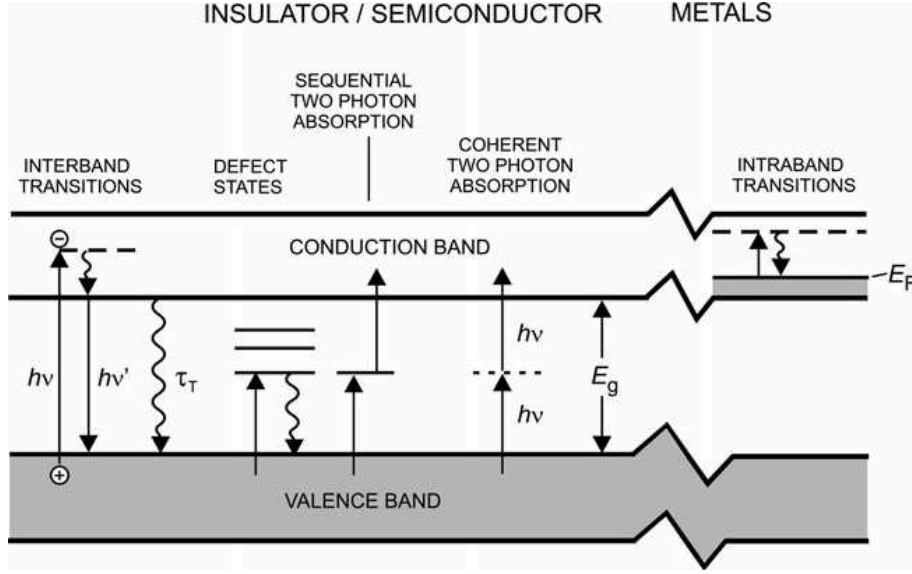
FIGURE 3.1: Schematic of different types of electronic excitations in a solid. [85]

where E_i is the electron energy in the lower band, E_f is the electron energy in the higher band, and hv is the photon energy. The excited electron occupies the final state ψ_f at energy E_f and leaves the initial state ψ_i at energy E_i unoccupied, which is equivalent to the creation of an electron-hole pair. And the quantum mechanical transition rate $W_{i \to f}$ for exciting an electron from ψ_i to ψ_f determines the optical absorption coefficient α of a photon with frequency of v. The transition rate is given by Fermi's golden rule:

$$W_{i \to f} = \frac{2\pi}{h} |M|^2 g(hv), \tag{3.2}$$

where M is the matrix element and $g(hv)$ is the density of states. The matrix element refers to the perturbation caused by the light wave on the electrons, and given by:

$$M = < f|H^{'}|i > = \int \psi_f^{\star}(r) H^{'} \psi_i(r) d^3 r, \tag{3.3}$$

where $H^{'}$ is the perturbation term, and r is the position vector of the electron. In classical electromagnetism, the presence of a perturbing electric field E causes a shift in the energy of a charged particle equal to $-p \cdot E$, where p is the electric-dipole moment of the particle. Here by applying the semi-classical approach, the quantum perturbation can be described as the electric-dipole interaction between the light and the electron:

$$H^{'} = -p_e \cdot E_{photon}, \tag{3.4}$$

where electron dipole moment $p_e = -e \cdot r$ and light wave $E_{photon}(r) = E_0 e^{ik \cdot r}$. Therefore the perturbation is written as:

$$H^{'} = e E_0 \cdot r e^{ik \cdot r} \tag{3.5}$$

And according to the Bloch's theorem, the wave functions can be written as a product of a plane wave and an envelope function that has the periodicity of the crystal lattice. So we have:

$$\psi_i(r) = \frac{1}{\sqrt{V}} u_i(r) e^{ik_i \cdot r} \tag{3.6}$$

$$\psi_f(r) = \frac{1}{\sqrt{V}} u_f(r) e^{ik_f \cdot r} \tag{3.7}$$

Considering the momentum conservation: $hk_f - hk_i = hk$, the matrix element can be finally written as:

$$|M| \propto \int_{unitcell} u_i^\star(r) x u_f(f) d^3 r, \tag{3.8}$$

in which light is defined to be polarized along the x axis. Then one can see that the evaluation of of the matrix element requires the knowledge of the envelope function of u_i and u_f, which are derived from the atomic orbitals of the constituent atoms. Therefore, each material has to be considered separately. Beside, the the joint density of states evaluated at the photon energy can be written as:

$$g(hv) = \begin{cases} 0 & : hv < E_g \\ \frac{1}{2\pi^2} \left(\frac{2\mu}{h^2} \right)^{\frac{3}{2}} (hv - E_g)^{\frac{1}{2}} & : hv \geq E_g \end{cases} . \tag{3.9}$$

And according to Fermi's golden rule given in equation 3.2, the absorption coefficient α is proportional to the joint density of states for $hv \geq E_g$:

$$\alpha(hv) \propto (hv - E_g)^{\frac{1}{2}}. \tag{3.10}$$

Therefore it is expected that the absorption increases as the photon energy increases. And for given photon energy larger than the band gap, according to the Kramers-Kronig relation, the refractive index increases as the band gap gets larger.

The above-mentioned approach provides an intuitive interpretation about how the absorption spectrum of a given material is related to its band structure, and in particular to the density of states of the transition. Moreover, thanks to the development of computational quantum mechanical modeling method such as density functional theory (DFT) [86], one can numerically calculate the frequency dependent linear optical dielectric function of any solid with satisfactory accuracy.

Of course, defects, impurities and surface states often permit sub-bandgap excitations with $hv \leq E_g$. On the other hand, the strong electric field associated with the high intensity available from a short pulse of light enables strong-field ionization (SFI) (or excitation) such as multi-photon and tunnel ionization (for a review see [87]). Once electrons are excited into the conduction band, they have the possibility to be accelerated by the laser field and to gain sufficient energy to enable excitation of other electrons from the

valence band by collisional excitation. And this gives the potential for an avalanche process. In 1965, Keldysh [88] proposed a quantitative model of the SFI which gives the strong-field excitation rate. Within the following years, several modeling approaches have been developed with more complete expressions for electronic excitation [89] and for impact ionization [90]. Accordingly, transient free-electron density can be consequently predicted. As soon as the density of conduction-band electrons becomes non-vanishing due to the electronic excitation, the dielectric material changes its optical properties dramatically. The 'free' electrons behave much like the conduction electrons of the metal, and the material acquires metal-like properties to the light response, such as a higher reflectivity and a finite penetration depth. An obvious way to describe the optical properties associated with the 'free' electron gas is the Drude model, and the dielectric function can be written as:

$$\epsilon_r(\omega) = 1 - \frac{\omega_p^2}{\omega^2 + i\gamma\omega}, \tag{3.11}$$

where

$$\omega_p = \left(\frac{Ne^2}{\epsilon_0 m_0}\right)^{1/2}. \tag{3.12}$$

ω_p is known as the plasma frequency, N is the carrier density and ϵ_0 is the electric permittivity. γ is the electron damping rate. By splitting $\epsilon_r(\omega)$ into its real and imaginary components that is: $\epsilon_r \equiv \epsilon_1 + i\epsilon_2$, we have:

$$\epsilon_1 = 1 - \frac{\omega_p^2}{\omega^2 + \gamma^2} \tag{3.13}$$

$$\epsilon_2 = \frac{\omega_p^2 \gamma}{\omega(\omega^2 + \gamma^2)}. \tag{3.14}$$

So when the electron density generated by SFI reaches a high density (e.g., $10^{21} cm^{-3}$), a large fraction of the remaining laser pulse will be absorbed.

3.1.2 Optical properties of metals

For metals, if we consider the polarization of the ion nucleus the above mentioned Drude model can be modified as:

$$\epsilon_r(\omega) = \epsilon_c - \frac{\omega_p^2}{\omega^2 + i\gamma\omega}, \tag{3.15}$$

The electron damping rate of metal $\gamma = \tau^{-1}$ is typically of order $10^{14} Hz$. And as list in table 3.1, the plasma frequencies ω_p of metals is in the ultraviolet spectral region. Therefore, for metals we have $\omega_p >> \gamma$.

Metal	$\omega_p/2\pi$ (10^{15} Hz)	λ_p (nm)
Cu	2.61	115
Ag	2.17	138
Au	2.18	138
Cr	2.60	115

TABLE 3.1: The plasma frequencies ω_p and the corresponding wavelength λ_p.

Reflection:

Then at low optical frequency condition, $\omega << \gamma$, one can write:

$$\epsilon_1 \approx -\omega_p^2 \tau^2 \tag{3.16}$$

and

$$\epsilon_2 \approx \frac{\omega_p^2 \tau}{\omega} \tag{3.17}$$

where $\tau = \frac{1}{\gamma}$. In this case, $\epsilon_2 >> \epsilon_1$, and we have

$$n = k \approx \sqrt{\frac{\omega_p^2 \tau}{2\omega}} \tag{3.18}$$

and the reflectance becomes:

$$R = 1 - \sqrt{\frac{8\omega}{\omega_p^2 \tau}}. \tag{3.19}$$

When $\gamma < \omega < \omega_p$, we have $\epsilon_1 \approx -\omega_p^2/\omega$ and $\epsilon_2 \approx \omega_p^2/\omega^3\tau$. Therefore the refractive index n and the extinction coefficient k can be written as:

$$n \approx \frac{\omega_p}{2\omega^2 \tau} \tag{3.20}$$

and

$$k \approx \frac{\omega_p}{\omega} \tag{3.21}$$

The wave is strongly damped under this condition. And a frequency independent reflectance is obtained:

$$R = 1 - \frac{2}{\omega_p \tau} \tag{3.22}$$

For high frequency ($\omega > \omega_p$), ϵ_1 is positive and quickly becomes bigger than ϵ_2, i.e.:

$$\epsilon_1 \approx \epsilon_c - \frac{\omega_p^2}{\omega^2} \tag{3.23}$$

and

$$\epsilon_2 \approx \frac{\omega_p^2}{\omega^3 \tau}. \tag{3.24}$$

The limiting high-frequency value of the reflectance is

$$R = \frac{(\sqrt{\epsilon_c} - 1)^2}{(\sqrt{\epsilon_c} + 1)^2} \tag{3.25}$$

For those above-mentioned situations, we only considered the contribution of free-electrons in metals. For light with a frequency smaller than the plasma frequency ($\omega << \omega_p$), the light is almost completely reflected. When the light frequency is comparable to the plasma frequency, it is partly absorbed and partly reflected from a metal surface. For the full information about the relation between optical frequency and reflectance for a large range of metals, we refer to Rakic et al [91]. Moreover, the temperature dependence of the contribution of free-electrons in metals is usually weak. This completely changes when interband transitions are involved.
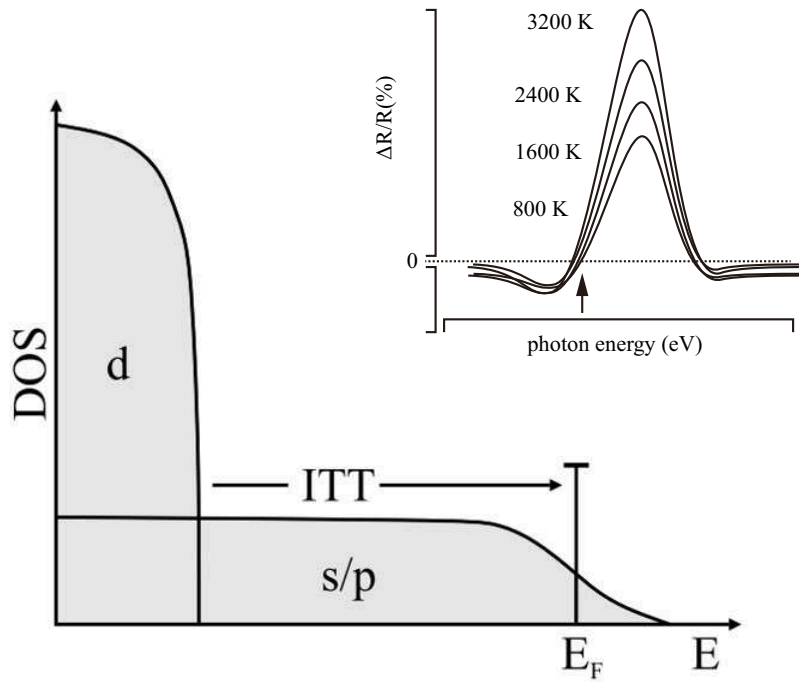
FIGURE 3.2: Schematic density of states for s/p band metals. ITT: inter-band transition threshold [92].

For noble metals such as copper and gold, the electronic configuration is described by the d-s/p band distribution as sketched in figure 3.2. The s/p band structures provide additional occupancies and therefore provides the possibility of interband transition from the filled d band to the unoccupied states in the s/p band above Fermi energy E_F. The electron transition refers to the photon absorption and therefore the decrease of reflectivity. Then, the broadening of the Fermi distribution at high temperatures will lead to an increase of the absorption for photons with energy $hv < ITT$, and a decrease

of the absorption for photons with energy $hv > ITT$. Those changes of the reflectivity have been computed by the model proposed by Jha et al. [93] and experimentally measured by Hohlfeld et al. [92]. For Cu, $ITT_{Cu} = 2.47\ eV$ and for Au, $ITT_{Au} = 2.20\ eV$. In this thesis, in order to avoid the influence of relative changes of the reflectivity under different temperatures, the wavelength of laser sources are chosen as 1070 nm (1.15 eV) and 355 nm(3.49 eV) and for the femtosecond laser with wavelength of 515 nm (2.41 eV) used in chapter 6, a Cr interlayer is coated between the substrate and the copper donor film. Therefore, the reflectivity changes induced by the temperature variation are neglected in further calculations presented in this work.

Absorption:

As the discussed above, the incident light will be partly reflected and partly absorbed by the metal layers. The attenuation of the optical intensity inside the bulk material follows Beer's law:

$$I(z) = I_0 e^{-\alpha_{opt} z} \tag{3.26}$$

and decays exponentially in the z penetration direction. This linear absorption coefficient α_{opt} is proportional to the extinction coefficient k with the relation $\alpha = 4\pi k / \lambda$. However, for ultrashort laser pulse the ballistic motion of the electrons leads to a decrease of the penetration depth and the absorption term is modified as:

$$\alpha_{tot} = \alpha_{opt} + \alpha_{bal}. \tag{3.27}$$

For thin film with thickness close to the penetration depth, multiple internal reflection should be considered in order to describe the effective absorption in the thin film. Therefore the absorbed energy density S is described as:

$$S(\mathbf{r}, t) = \frac{\alpha_{tot}(1 - R)I(\mathbf{r}, t)exp(-z\alpha_{tot})}{1 - exp(-d\alpha_{tot})}, \tag{3.28}$$

where d is the thickness of the thin film.

3.2   Ultrashort laser-metal interaction

The incoming photons are absorbed by the electronic subsystem, leading to the formation of gas of hot carries which transfer their energy to the ions through repeated emission of phonons. Ionic and electronic subsystems reach an equilibrium at the time scale of $\tau_E = 10^{-12} - 10^{-11}\ s$ [94]. This is a critical timescale for the laser-induced phenomenon as it sets the boundary between thermal and nonthermal routes, and a separation between "long" and "short" pulses [95]. When pulse duration $\tau_L \gg \tau_E$, the equilibrium between electrons and phonons is preserved throughout the heating stage and the electron temperature is equal to the target temperature. Then, the phase change can be considered as a slow thermal process occurring with quasi-equilibrium thermal dynamics. When the quasi-continuous (QCW) laser irradiates the donor

		10^{-16}	10^{-15}	10^{-14}	10^{-13}	10^{-12}	10^{-11}	10^{-10}	10^{-9}	10^{-8}	10^{-7}	10^{-6}	10^{-5}
Carrier excitation	Photon absorption												
	Impact ionisation												
Thermalisation	Carrier-carrier scattering												
	Carrier-phonon scattering												
Carrier removal	Auger recombination												
	Radiative recombination												
	Carrier diffusion												
Thermal and structural effects	Ablation and evaporation												
	Thermal diffusion												
	Resolidification												
Timescale (s)		10^{-16}	10^{-15}	10^{-14}	10^{-13}	10^{-12}	10^{-11}	10^{-10}	10^{-9}	10^{-8}	10^{-7}	10^{-6}	10^{-5}

FIGURE 3.3: Illustration of process taking place in the target following the absorption of the laser pulse. [96]

film, the above-mentioned dynamics dominate the thermalization process. In contrast, for ultrashort pulses ($\tau_L \leq 10^{-12}$ s), a high non-equilibrium state takes place in the target, and the time scale of the structural modification τ_M determines whether thermal mechanisms are involved ($\tau_M \gg \tau_E$) or not ($\tau_M < \tau_E$) [95]. The most important processes related to the absorption and the diffusion of the laser energy, and their corresponding timescale, are summarized in figure 3.3. Based on those phenomena, this section provides a brief description of the processes induced by the interaction of ultrashort laser pulse with metals.

3.2.1   Thermal process

The energy of the incident laser pulse absorbed by the metal leads to the heating of the electrons and brings the electron-subsystem into a strong non-equilibrium state. at this stage, two competing processes take place; the ballistic motion and the thermalization of the electron gas. The ballistic motion comes from the unhampered penetration of the heated electrons into the bulk material. The electrons penetrate into the bulk material with the Fermi velocity, and the ballistic range is controlled by the time-scale for the electron-subsystem to reach its thermal equilibrium and the Fermi velocity. The typical value of the ballistic range obtained by time-resolved measurements is in good agreement with the mean free path length of the heated electrons. Consequently, the ballistic range of noble metals is dominant. For copper, the typical value is found to be 117 nm. It worth to note that, this value is determined for femtosecond laser pulses. For picosecond pulses, the effect of ballistic motion is generally less pronounced when compared to the femtosecond laser pulses and it can be often neglected.

As we have discussed in section 3.1, the optical properties of the material are determined by the configuration of its electron subsystem. Due to the scattering process induced by ultrashort pulse irradiation, the thermalization of the heated electron subsystem during the first few 10s of femtoseconds transforms the initially deformed density of states (DOS) distribution in a Fermi distribution of DOS. A theoretical investigation on the distorted DOS and its effects on the physical properties has been presented by Rethfeld et al. [89]. It has been demonstrated that the DOS distribution is deformed by the optical excitation induced by the femtosecond laser pulse. Once the electron subsystem reaches the equilibrium conditions, the ongoing scattering processes between the electrons and phonons would finally lead to a thermal equilibrium between the electron and phonon subsystems. The scattering rate between the electrons and phonons are given by the electron-phonon coupling factor *g* which varies with the DOS. Due to the unbalanced heat capacities of the phonons and the electrons, the temperature rise of the phonons is significantly smaller than the one of the electrons and the temperature penetration depth in the phonon system is also smaller than for electrons. Therefore, the heat transport is dominated by the electron system and the heat conduction in the lattice of metal can be often neglected.

3.2.2 Laser-induced breakdown

If the laser fluence exceeds the threshold for evaporation, the latent heats of melting, L_m, and evaporation, L_v, should be taken into account. With an even higher fluence, a hot plasma of atoms, ions, and electrons, is formed above the surface. This plasma can emit specific radiative emissions and a characteristic acoustical shock wave can also be generated by the fast expansion of the plasma plume. In this thesis, the investigation of laser-induced plasma is limited to the very basic energy balance level, and the fluence threshold to generate a plasma is estimated by:

$$F_{pl} = \rho(L_m + L_v)\sqrt{D\tau_p} \tag{3.29}$$

where ρ is the material density, $D = \frac{K_{th}}{\rho C_p}$ is the thermal diffusivity of the material, $K_t h$ is the thermal conductivity, C_p is the heat capacity and τ is the laser pulse duration.

3.2.3 Modeling

To investigate the thermal response induced by the ultrashort laser pulse, a widely used model is the two-temperature model (TTM). Within several hundred femtoseconds thermal equilibrium among the excited electrons is reached. Once it is reached, this model allows describing the temperature evolution of the hot electron bath (T_e) and the cold lattice (T_l). The cooling of electron temperature T_e is induced by electron-phonon coupling and by diffusive motion. The temporal and spatial temperature relaxation can be described by two coupled diffusive equations. The first one represents the

heat conduction of the electrons and the second one describes that of the lattice. The two equations are connected by a term that is proportional to the electron-phonon coupling factor g and to the temperature difference between electrons and lattice. As originally proposed by Anisimov et al. [97], the main assumption of TTM is that the electron-phonon coupling can be united in a single linear coupling term with the form $g \times (T_e - T_l)$. The TTM can then be written as:

$$C_e(T_e)\frac{\partial T_e}{\partial t} = \frac{\partial}{\partial z}(K_e\frac{\partial}{\partial z}T_e) - g(T_e - T_l) + S(\mathbf{r}, t), \tag{3.30}$$

$$C_l\frac{\partial T_l}{\partial t} = g(T_e - T_l). \tag{3.31}$$

where C_e and C_l are the respective heat capacities of electrons and lattice, K_e the thermal conductivity of the electrons. And $S(\mathbf{r}, t)$ is the source term.

In order to numerically calculate the time-dependent temperatures of the electron-phonon subsystem, we define $C_e = A_e T_e$, where A_e is the electron specific heat constant. We also define $K_e = K_{e0}T_e/T_l$ as the thermal conductivity in metals which is dominated by the electronic structure. The enthalpies of melting and vaporization are incorporated by adding a Gaussian function to the lattice heat capacity C_l, and the heat conductivity in the lattice is neglected. The temporal evolution of the incident laser pulse intensity $I_0(t)$ is mathematically described as:

$$I_0(t) = \frac{2F\sqrt{ln2}}{\sqrt{\pi}\tau_p}exp(-4ln2(t/\tau_p)^2), \tag{3.32}$$

where F is the laser fluence and τ is the incident pulse duration. Then, according to equations 3.26, 3.28 and 3.32, the electron heating induced by the Beer-Lambert absorption of the incident laser pulse can be expressed as:

$$S(z, t) = \frac{2F\sqrt{ln2}}{\sqrt{\pi}\tau_p}\frac{\alpha_{tot}(1 - R)exp(-z\alpha_{tot})exp(-4ln2(t/\tau_p)^2)}{1 - exp(-d\alpha_{tot})}, \tag{3.33}$$

Initial and boundary conditions:

Both, the electron and lattice temperatures are initially in an equilibrium state and they have been set to standard room temperature $T_e = T_l = 293K$. A zero flux boundary condition for both interfaces is set, since compared to the thermal diffusivity of the donor substrate (soda-lime glass $\approx 10^{-6} \ m^2/s$) and the ambient atmosphere ($\approx 10^{-5} \ m^2/s$) it appears that the heat conduction occurs mainly in the donor layer (copper $\approx 10^{-4} \ m^2/s$). Therefore, in the model both the donor substrate and the ambient atmosphere are discarded from the geometry. And at each interface a zero-flux boundary conditions $C_e\frac{\delta T}{\delta t} = 0$ are applied.

Quantity	Symbol	Copper	Unit
Melting temperature	T_m	1357.7	K
Vaporization temperature	T_v	2835	K
Lattice heat capacity	C_l	$3.26 \cdot 10^6$	J $m^{-3}K^{-1}$
Melting enthalpy	L_m	$1.87 \cdot 10^9$	J $m^{-3}K^{-1}$
Electron specific heat constant	A_e	98	J $m^{-3}K^{-2}$
Electron heat conductivity	K_{e0}	401	W $m^{-1}K^{-1}$
Electron-phonon coupling factor	g	$10 \cdot 10^{16}$	W $m^{-3}K^{-1}$
Reflection coefficient	R	0.6	-
Absorption coefficient	α_{opt}	$6.33 \cdot 10^5$	cm^{-1}
Density	ρ	8960	kg m^{-3}
Thermal diffusivity	D	$1.1 \cdot 10^{-4}$	m^{2}s^{-1}

TABLE 3.2: Chemical composition of soda lime glass [98].

Material properties:

In this thesis, the modeling study is applied to copper and the data of the material properties come from the work of Hohlfeld et al. [92]. In table 3.2, those material properties which has been used for simulations are reported. For the 10s of picoseconds regime, the electron-phonon coupling factor is set as a constant.

Numerical solver:

The implicit approach is used to solve the two time-dependent heat conduction equations in the two temperature model, see equation 3.30 and 3.31, and to obtain numerical solutions. In this thesis, a commercial finite-element software COMSOL Multiphysics is used. In order to describe the heating process of a laser in the 10s of picoseconds regime with a sufficient precision, the time step is finally chosen as $100 \cdot 10^{-15}$. Taking into account the computational time cost and the requirement of achieving a numerically stable solution, a compromised mesh element dimension of 5 nm is chosen.

Validity of the model:

Figure 3.4 shows the evolution of the electron and the lattice temperatures at the glass-copper interface induced by a picosecond laser irradiation calculated with the model. The incident laser pulse $I_0(t)$ is also plotted on the same graph, and the maximum laser intensity is set at $t = 2\tau_p$ in order to make sure that the full energy of the laser pulse is taken into account in the simulation. The temporal evolution of the electron subsystem follows the evolution of the intensity of the incident laser pulse. When the laser pulse intensity reaches its maximum and starts to decrease, one can observe that the electron temperature continues to increase. This means that even after its maximum the incident laser energy still overcomes the losses due to the electron-lattice relaxation. Therefore, the maximum electron temperature arrives with a short delay after the peak of the laser intensity. Meanwhile, the
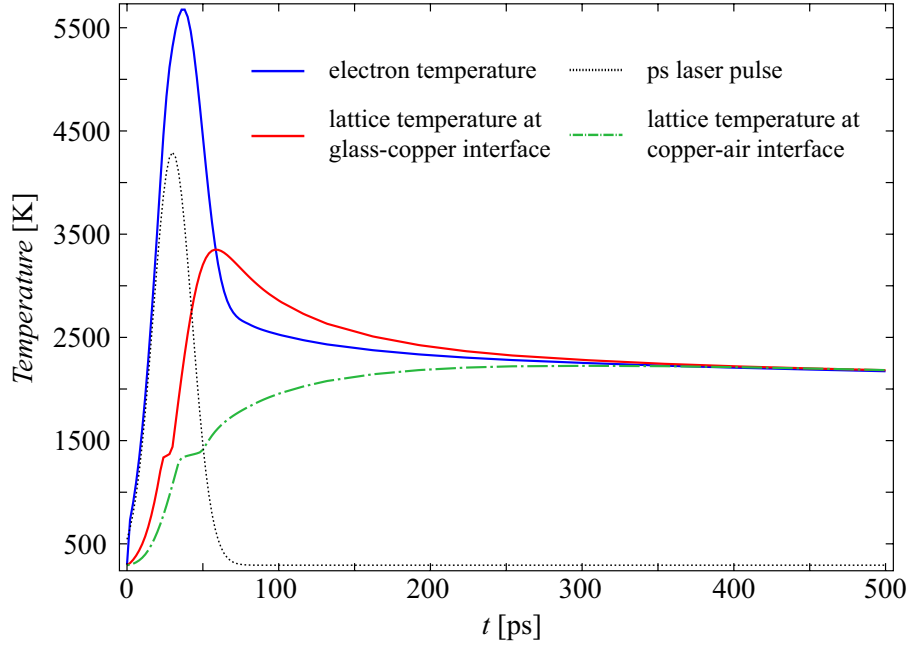
FIGURE 3.4: Evolution of lattice and electron temperatures at the glass-copper and copper-air interface. This evolution is calculated for a fixed laser fluence of 410 mJ/cm^2 with a 180 nm copper donor film. Besides, the temporal distribution of the incident laser pulse intensity is indicated by the black dotted line.

lattice temperature also increases. When it passes the melting temperature, a flat shoulder indicates that a phase change from the solid to the liquid. And finally, the equilibrium temperature is reached at ~ 300 ps.

To validate these numerical results, the lattice temperature is compared with a known analytical solution calculated according to the equation:

$$\Delta T = \frac{(1 - R)F - dL_m}{d\rho C_p} \tag{3.34}$$

where F is the laser fluence, L_m is the melting enthalpy of copper and C_p is the heat capacity of copper. The plot in figure 3.4 shows the temperature evolution induced by the laser pulse with a fluence of 410 mJ/cm^2. At $t = 350$ ps the electron-phonon subsystem has reached the equilibrium and numerically obtained lattice temperature under this fluence is 2202 K. In comparison, the value of the lattice temperature calculated according to the equation 3.34 is 2347 K. The temperature difference of 145 K (6.2 %) can be explained by the fact that the analytical model does not take into account the lateral heat diffusion during the heating process, therefore overestimates the temperature increase.

3.3　QCW laser heating of metals

As presented in figure 3.3, for laser pulse with a duration longer than 10^{-6} s (QCW laser pulse), the equilibrium between electrons and phonons is preserved throughout the heating stage and the phase change can be regarded as a slow thermal process occurring with an equilibrium thermal dynamics. Therefore, the heating process of the donor film induced by the QCW pulse can be described by the general heat equation:

$$\rho C_p \frac{\partial T}{\partial t} - \nabla(K(\nabla T)) = Q,\qquad(3.35)$$

which gives the temperature T in the system in response to a heat source Q. The enthalpies of melting and vaporization are incorporated to the model by adding Gaussian functions to the copper heat capacity C_p, centered at the equilibrium phase-change temperatures, with a standard deviation of 20 K.

　　Due to the Gaussian profile of the QCW laser intensity distribution at the donor surface, the heat source Q, due to the absorption of the QCW laser energy, is defined with a Gaussian distribution along the x-direction, parallel to the film surface, according to the Beer-Lambert law and taking into account the multiple internal reflections in the thin film.

$$Q = I_0(t)\alpha(1-R)exp(\frac{-2x^2}{\omega_0^2})exp(\frac{exp(-\alpha z)}{1-exp(-\alpha d)}),\qquad(3.36)$$

where R represents the reflection coefficient, α the linear absorption coefficient, d the thickness of the thin film, ω_0 the beam waist and z the absorption direction. The QCW laser pulse intensity $I_0(t)$ is described by a piecewise function to carefully represent the real temporal evolution.

$$I_0(t) = \begin{cases} \frac{2E_p}{\pi\omega_0^2\tau_{qcw}} & : & 0 \le t < \tau_{qcw} \\ \frac{2E_p}{\pi\omega_0^2\tau_{qcw}}exp(-\frac{(t-\tau_{qcw})^2}{40}) & : & \tau_{qcw} \le t < \tau_{qcw}+\Delta \\ 0 & : & t \ge \tau_{qcw}+\Delta \end{cases},\qquad(3.37)$$

where E_p is QCW pulse energy, ω_0 is the beam waist, τ_{qcw} is the QCW pulse duration and Δ corresponds to the falling edge of the pulse.

Material properties:

We mainly work with copper and, as for the other metals, its density ρ and thermal conductivity K are both temperature dependent [99, 100]. In table 3.3, the values of some relevant physical properties of copper are given for a range of temperature of interest for this study. Thus, the heat equation which describes this process is not linear and thus should also be numerically solved. In this thesis, COMSOL Multiphysics is also used to solve the non-linear partial differential equations.

T [K]	Thermal conductivity [i]	Heat capacity [ii]	Density [iii]
293	400	382	8960
573	381	413	8809
973	354	446	8598
1400	167	516	7907
1550	173	516	7796
1700	177	516	7686
1850	180	516	7576

[i]$K\,[W\,m^{-1}K^{-1}]$ [ii]$Cp\,[J\,kg^{-1}K^{-1}]$ [iii]$\rho\,[kg\,m^{-3}]$

TABLE 3.3: Temperature dependent thermodynamic properties of copper.

Initial and boundary conditions

Contrary to the ultrashort laser pulse excitation, the QCW laser pulse heating can be viewed as a slow thermal process and the thermal diffusions at glass-donor and donor-air interfaces should also be taken into consideration. Here, the thickness of the glass substrate is set as 1 mm as well as the thickness of the air layer above the copper film. The initial temperatures of all the materials are set to standard room temperature 293 K, and a zero flux boundary condition $C_p \frac{\delta T}{\delta t} = 0$ is set only for the outside interfaces of the whole system. Heat fluxes at glass-donor and donor-air interfaces are dominated by the general heat equations.

Chapter 4

Material and experimental methods

This chapter presents the experimental details of the double-pulse LIFT setups. Moreover, sample preparation methods and postmortem diagnostic techniques are presented.

Contents

4.1   Introduction

To demonstrate the potential of the double-pulse LIFT approach and to perform further optimization, a comprehensive investigation of the DP-LIFT process is required. Therefore, several experimental setups have been designed and implemented to reach the objectives described in section 1.3. In the following chapters, in order to reduce the cross-references and increase the readability, the description of each experimental setup will be repeated in a specific form according to the special question addressed in the chapter. Thus in this chapter, only a general sketch of DP-LIFT setup is described. Furthermore, the experimental methods for controlling the time-sequencing and the size of the donor-receiver gap are discussed. Finally, sample preparations and postmortem diagnostic methods that have been used in this thesis are presented.

4.2   Experimental setup

4.2.1   DP-LIFT setup

Figure 4.1 shows a sketch of the DP-LIFT setup, this prototype was designed to allow flexible investigations on the DP-LIFT process from various aspects. This setup is composed of three major parts: optical part for double-pulse positioning, LIFT processing, and time-resolved visualization; mechanical part for the donor-receiver positioning; electronic part for the synchronization.

   The laser source used to achieve the melting of the donor film is a so-called quasi-continuous wave (QCW) laser, consisting in a IPG PHOTONICS YLR-150/1500-QCW-AC-Y14 ytterbium fiber laser in combination with an IPG Photonics D25-F50 optic collimator. The laser source used to initiate the LIFT process is called the LIFT laser. In this thesis, different LIFT lasers have been used with wavelengths of 355-nm & 515-nm and with pulse durations of 50-ps & 500-fs. The details of those two lasers will be described in chapter 5 and chapter 6. A polarized beam splitter (PBS) and half-wave plate are used to adjust the input energy of LIFT laser, and a shutter (or Pockels cell) is used to select a single pulse from the train. The donor and receiver stages are positioned perpendicularly to the direction of the LIFT laser beam. A THORLABS TTR001 Tip, Tilt, & Rotation stage combined with two NEWPORT MFA-CC motorized linear stages and a NEWPORT M-UMR5.25 manual linear stage define the mechanical motion unit. It allows for adjusting the perpendicularity between the motion planes of the substrates and the LIFT laser beam. This motion unit can carry a vacuum chunk whose angular orientation is adjusted by a THORLABS KM100 Kinematic Mirror Mount. Thanks to this design, the angular orientation of donor and receiver substrates can be independently adjusted. Therefore, by taking the LIFT laser beam as a reference, the motion planes of both the donor & receiver stages and the donor & receiver substrates can be aligned parallel with respect to each other.

   For the double-pulse positioning, the beams of QCW laser and LIFT laser are combined by a dichroic mirror and focused onto the donor substrate by
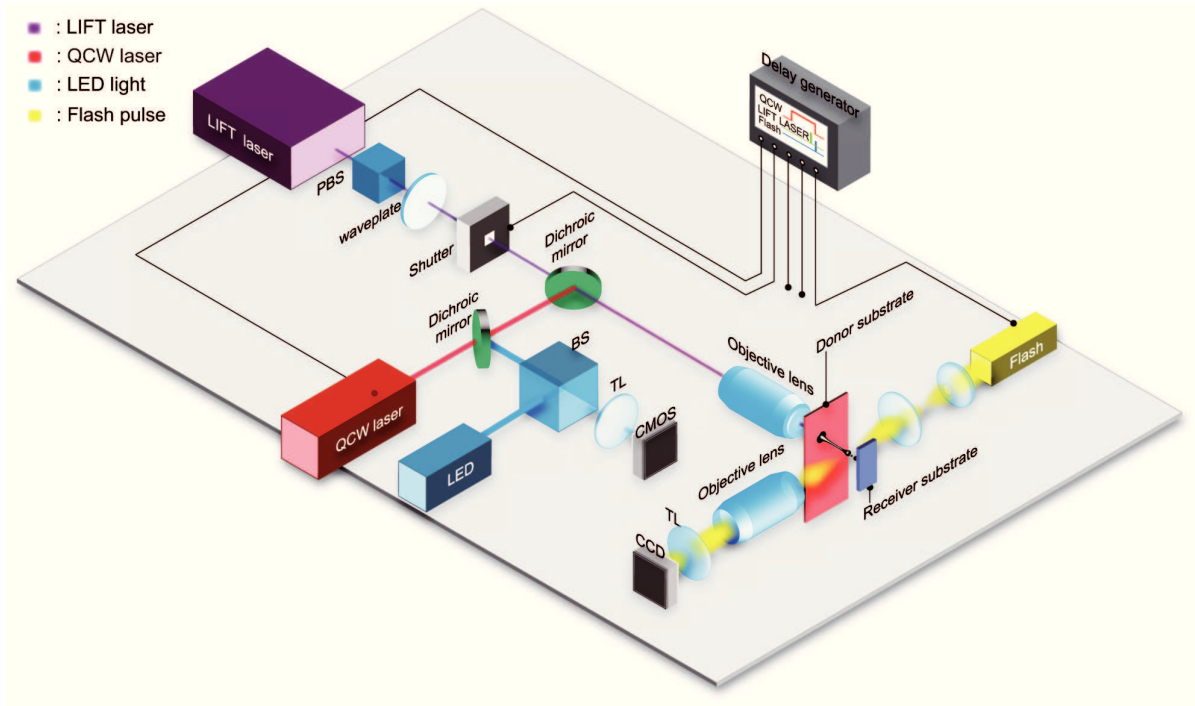
FIGURE 4.1: Sketch of a DP-LIFT platform which mainly consists of: four optical paths to implement the double-pulse positioning, the LIFT processing and the visualization; six linear translation stages (not shown in this sketch) to position the donor and receiver substrates with an adjustable separation; one delay generator to synchronize the above-mentioned processes.

an objective lens. In order to keep those two focused beams precisely concentric on the donor surface throughout the whole printing process, accurate monitoring is required. Thus, based on the same above the mentioned objective lens, a reflected light microscope is implemented. A light-emitting diode (LED) is used as the light source of this microscope, a beam splitter (BS) reflects the LED lights and transmits the image of the donor surface. A THORLABS LB1437-ML bi-convex lens is used as the tube lens and form the image on a THORLABS DCC1645C CMOS cameras. This homemade microscope allows us to monitor the donor surface quality and the relative position of the two laser spots focused on this surface.

In order to have visualizations of the material ejections induced by DP-LIFT, as illustrated by section 2.3, a time-resolved shadowgraphic microscope is required. In this thesis, a HIGH-SPEED PHOTO-SYSTEME KL-M NANO-LITE nanosecond flash lamp with a flash duration of 12-ns, which defines the temporal resolution, is used for bright-field illumination. The illuminated scene is recorded by a QIMAGING QICAM CCD camera mounted on another customized microscopy arrangement based on MITUTOYO M Plan Apo SL long working distance microscope objective lenses and a MITUTOYO MT-1 tube lens. The synchronization of both DP-LIFT processing and acquisition of the ejection images are realized by a STANFORD RESEARCH SYSTEMS DG645 delay generator. The details of the sequence diagram are discussed in the next subsections.

Parameter	IPG YLR-150/1500-QCW-AC	Continuum Leopard SS-10	Amplitude s-Pulse HP
M^2	1.04	-	1.13
Pulse duration	0.05-50 ms	50 ps	450 fs
Beam waist	8.9 mm	< 10 mm	3 ± 0.5 mm
Beam divergence	0.17 mrad	0.4 mrad	0.6 mrad
Fondamental wavelength	1070 nm	1064 nm	1030 ± 10 nm
Repitation rate	1-5000 Hz	10 Hz	1-100 KHz
Maximum pulse energy	15 J	80 mJ	1.10 mJ (1 KHz) 0.04 mJ (100 KHz)
Polarization	random	linear	linear

TABLE 4.1: Overview of the properties of the laser sources used in this thesis for DP-LIFT process.
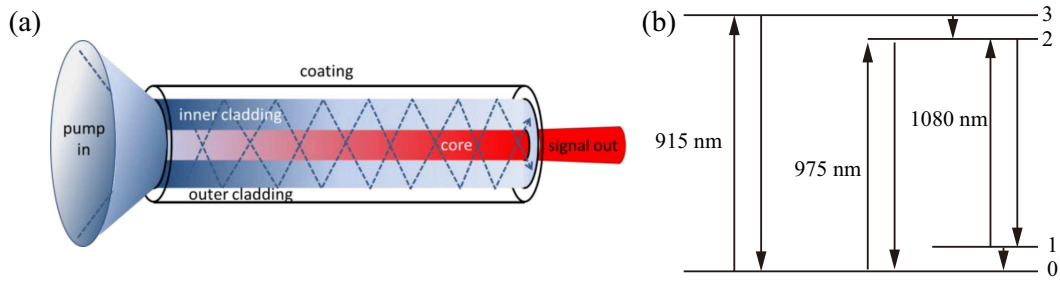
FIGURE 4.2: (a) Schematic diagram of a cladding-pumped fibre laser [101]. (b) A simplified 4-level scheme of Yb^{3+} ion.

4.2.2 Laser sources

Three different laser sources with a pulse duration in the microsecond, picosecond and femtosecond regime and wavelength from ultraviolet to near-infrared were employed for the investigation of the double-pulse LIFT process, see table 4.1. In this section, brief reviews for each laser source are provided.

High-power fibre lasers:

The optically pumped fiber-laser amplifiers have been widely used in fiber-communications over a long distance for boosting weak signals to extend the range of communication networks. However, the efficient coupling of the light emitted from the diode laser arrays into the narrow fiber core has been the main challenge to overcome to realize high power fiber lasers. As the diameters of the fiber lasers core are in a range of 5-12 μm, it is not possible to excite the active ions in rare-earth-doped fiber amplifier with a diode laser

using an end-on pumping geometry. To solve this problem, the cladding-pumped fiber laser was demonstrated by Snitzer et al. [102]. In this configuration, the active core is surrounded by two layers of cladding (see figure 4.2) and the inter undoped cladding layer has an intermediate refractive index. This intermediate cladding layer can be larger than 100 μm, therefore it becomes possible to inject divergent pump radiation from a semiconductor laser array. Most of the light coupled in this intermediate layer is confined inside the fiber core and contributes to the pumping the fiber laser. By adding reflectors at each end of the fiber, a powerful oscillator can be established. One of the most relevant doped systems is based on Yb^{3+} in germano-alumino-silicate glass since the absorption band of Yb^{3+}, centered at 915 nm, lies in a region where powerful semiconductor lasers are available. The QCW laser used in this thesis is a commercial high-power Ytterbium fiber-laser emitting at a wavelength of 1070 nm and the single-mode CW power is as high as 150 W (peak power: 1500 W in QCW mode). Thanks to the master oscillator fiber amplifier (MOFA) technique short-pulse can also be generated for fiber-laser. To do so, the excitation current of the semiconductor laser is modulated in order to achieve the required output pulse format. In this thesis, the output pulse duration can be varied from 50 μs to continuous wave.

High energy Picosecond Nd: YAG Laser:

As indicated in section 2.1.4, the transfer process of DP-LIFT is initiated by an ultrashort laser pulse. Of course, 'ultrashort' is a relative term and in this thesis, it refers to optical pulse shorter than 1 ns. For this study, we first investigate the DP-LIFT process based on a high energy picosecond laser.

To be more specific, we used a Leopard model picosecond laser from Continuum (see figure 4.3) which is a cavity dumped passive mode-locked system. The oscillator has a large mode volume and an intra-cavity spatial filtering system that allows getting high pulse energy with a smooth beam profile. The oscillator cavity uses the classical mode-locking system (acousto-optic for active mode lock and saturable absorber for passive mode locker) and the cavity dumping technique, which is recognized as one of the most efficient techniques for increasing the single pulse energy in picosecond solid-state laser, to extract one of the pulses from the train. The laser cavity dump consists of an electro-optic Pockels cell triggered by a photodiode. Another feature of the Leopard oscillator is the use of a GaAs wafer as a passive negative feedback element, which controls the energy extraction rate and provides the long flat pulse trains with a good pulse to pulse energy stability.

So when the lamps are flashed and lasing begins in the cavity, the acousto-optic mode locker (active modelocking) forms a pulse. This pulse is amplified in the cavity and shortened by the saturable absorber (passive mode-locking) at each round trip. And this trips continues until peak energy is achieved. When sufficient peak energy is reached, the two-photon absorption (TPA) process in the GaAs asserts itself, chopping of the end of the pulse [103]. Then, the pulse being shorter, the TPA critical intensity of the GaAs occurs at lower energy and shortens the pulse earlier. The pulse energy drops until a minimum pulse width determined by gain bandwidth and dispersion
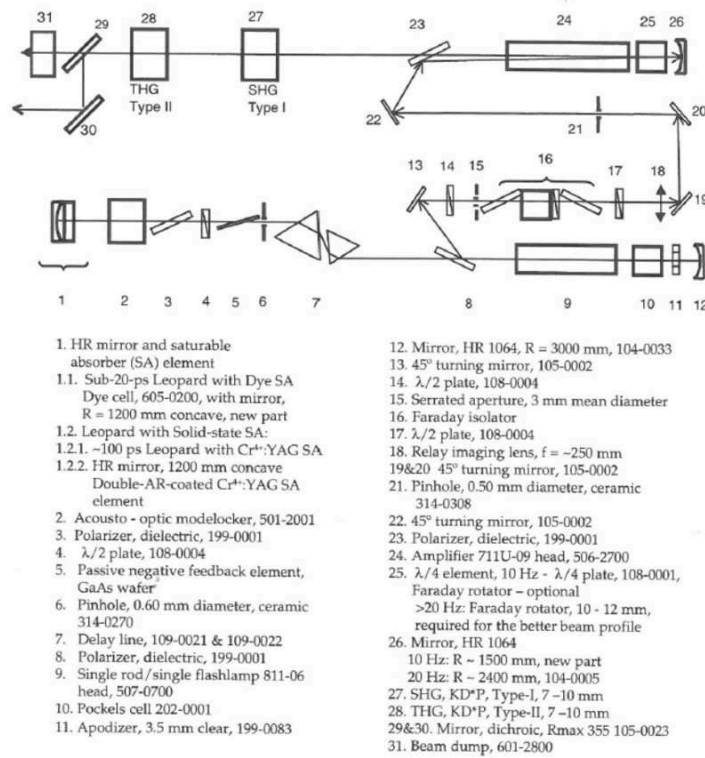
1. HR mirror and saturable
   absorber (SA) element
1.1. Sub-20-ps Leopard with Dye SA
   Dye cell, 605-0200, with mirror,
   R = 1200 mm concave, new part
1.2. Leopard with Solid-state SA:
1.2.1. ~100 ps Leopard with Cr⁴⁺:YAG SA
1.2.2. HR mirror, 1200 mm concave
   Double-AR-coated Cr⁴⁺:YAG SA
   element
2. Acousto - optic modelocker, 501-2001
3. Polarizer, dielectric, 199-0001
4. λ/2 plate, 108-0004
5. Passive negative feedback element,
   GaAs wafer
6. Pinhole, 0.60 mm diameter, ceramic
   314-0270
7. Delay line, 109-0021 & 109-0022
8. Polarizer, dielectric, 199-0001
9. Single rod/single flashlamp 811-06
   head, 507-0700
10. Pockels cell 202-0001
11. Apodizer, 3.5 mm clear, 199-0083

12. Mirror, HR 1064, R = 3000 mm, 104-0033
13. 45° turning mirror, 105-0002
14. λ/2 plate, 108-0004
15. Serrated aperture, 3 mm mean diameter
16. Faraday isolator
17. λ/2 plate, 108-0004
18. Relay imaging lens, f = ~250 mm
19&20 45° turning mirror, 105-0002
21. Pinhole, 0.50 mm diameter, ceramic
   314-0308
22. 45° turning mirror, 105-0002
23. Polarizer, dielectric, 199-0001
24. Amplifier 711U-09 head, 506-2700
25. λ/4 element, 10 Hz - λ/4 plate, 108-0001,
   Faraday rotator – optional
   >20 Hz: Faraday rotator, 10 - 12 mm,
   required for the better beam profile
26. Mirror, HR 1064
   10 Hz: R ~ 1500 mm, new part
   20 Hz: R ~ 2400 mm, 104-0005
27. SHG, KD*P, Type-I, 7 –10 mm
28. THG, KD*P, Type-II, 7 –10 mm
29&30. Mirror, dichroic, Rmax 355 105-0023
31. Beam dump, 601-2800

FIGURE 4.3: Schematic illustration of optical layouts of Leopard picosecond laser system.

is achieved. At this point, the energy in the cavity is clamped and keep the same as long as there is still gain left in the rod. And in this plateau, the pulse is cavity dumped out of the oscillator. Due to the clamping of the energy in the oscillator, a low energy output results. Therefore, it is necessary to double pass the amplifier to achieve maximum energy. The wavelength of the output laser pulse is at the Nd: YAG fundamental wavelength (1064 nm). Second (532 nm) and third harmonic (355 nm) can also be generated by frequency conversion in KD*P crystals.

In this thesis, to demonstrate the concept of DP-LIFT and to compare the ejection dynamics in single and double pulse LIFT, this 50 ps picoseconds laser with 355 nm in wavelength has been used.

Diode-pumped ultrafast amplified femtosecond Yb: YAG Laser:

To have a finer control about the volume of the propellant part during the DP-LIFT, according to the equation 2.1, shorter pulse for initiating the ejection is expected. Then, to make our second prototype of DP-LIFT system more universal in terms of material and thickness of the donor films, we have used a femtosecond laser.

The LIFT laser source is the S-Pulse HP femtosecond laser from Amplitude Systemes which is a diode-pumped ultrafast amplified femtosecond Yb: YAG laser system (see figure 4.4). One of the most important features of the femtosecond laser system is the so-called chirped-pulse amplification
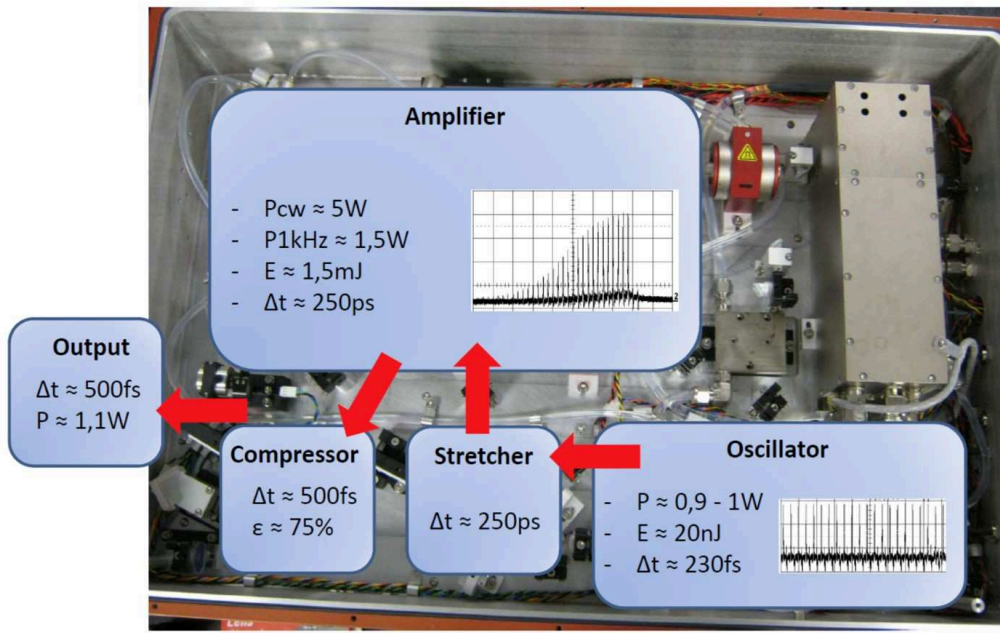
FIGURE 4.4: Schematic illustration of optical layouts of S-Pulse HP femtosecond laser system.

(CPA). The seed light generated by the oscillator has a typical pulse duration of 230 fs and pulse energy of 20 nJ. For such a short pulse, the energy needed to reach the saturation fluence would lead to a peak intensity above the damage thresholds of the amplifier rod or some other optical components. CPA technique is then required to amplify low-energy (20 nJ) pulses in order to achieve high-energy (1.5 mJ) pulses. This is performed in three stages:

- 1, The pulses are temporally stretched by passing through a pulse stretcher with a large group delay dispersion. Here the stretch factor is $\sim 10^3$.

- 2, The stretched pulses are amplified in a crystal without any risk of damage thanks to the lower peak intensity.

- 3, The amplified pulse is then compressed back to 500 fs through a pulse compressor.

After the above-mentioned process, a 500 fs pulse train with an average power of 1.1 W (1 kHz) and wavelength of 1030 nm are achieved. Second harmonic generation (515 nm) is performed outside of the laser system with a second harmonic crystal. The laser power of the two polarized lasers (Leopard and S-pulse laser) are adjusted by using an association of an half-wave plate and a polarizing beam splitter (PBS). For the random polarized fiber laser, an integrated control panel provides the ability to continuously adjusting its output laser power.

Beam waist:

The beam waist ω_0 of the focused laser beams were determined by the D^2 method [104]. The size of the ablation crater as a function of the fluence is
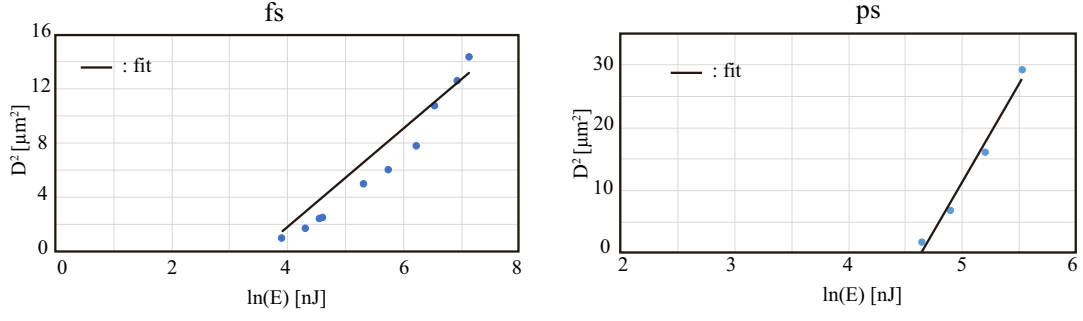
FIGURE 4.5: Schematic illustration of scanning electron microscope.

provided as:

$$D^2 = 2\omega_0^2 ln\left(\frac{F}{F_{mod}}\right) \tag{4.1}$$

where D the crater diameter and F_{mod} the threshold fluence. The variation of the squared crater diameter with respect to the laser fluence is presented in figure 4.5. And the beam waist of the focused laser beam is determined by the average slope of this measurement. The beam waist of the ps laser is determined to be 3.5 μm and the beam waist of the fs laser is determined to be 1.6 μm.

4.2.3 Electronic time-sequencing

Figure 4.6 shows the time sequence for triggering the different steps required to run the DP-LIFT process. The output signal of the LIFT laser, which operated at a given pulse repetition rate (PRR), is monitored by a THORLABS DET10A Si Detector. A pulse generator which provides a gate signal whose duration is equal to the inverse of the LIFT laser PRR is used to select one of photodiode signal from the pulse train. It is named the master pulse and used as a trigger for the whole process sequence. The delay between the LIFT pulse and master pulse can be set as $n \times \frac{1}{PRR}$ (n is an integer). In figure 4.6, n was set as 1. With the trigger signal as an input, a delay generator DG645 is used to synchronize all events of DP-LIFT process, including the time-resolved visualization to the ejection.

The first output of the DG645 pulse generator is used to trigger a THORLABS SH05 Beam Shutter (or Pockels cells) to pick out the LIFT pulse.

The second output is used to synchronize the QCW laser pulse and the LIFT pulse with an adjustable delay. The QCW laser pulse duration is previously set thanks to the panel control of the laser system.

The third output is used to trigger the nanosecond flash lamp to provide the bright field illumination at the different time of the DP-LIFT process.

The fourth output is used to trigger the camera shutter. By setting the delay and signal duration, the shutter opening time is set to allow the flash illuminated scene to be recorded.
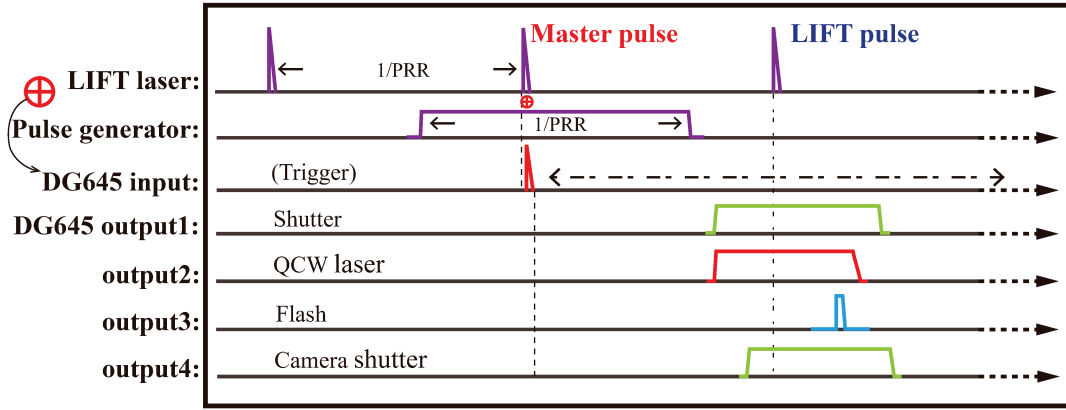
FIGURE 4.6: Time sequence of the different steps required to operate the DP-LIFT process.
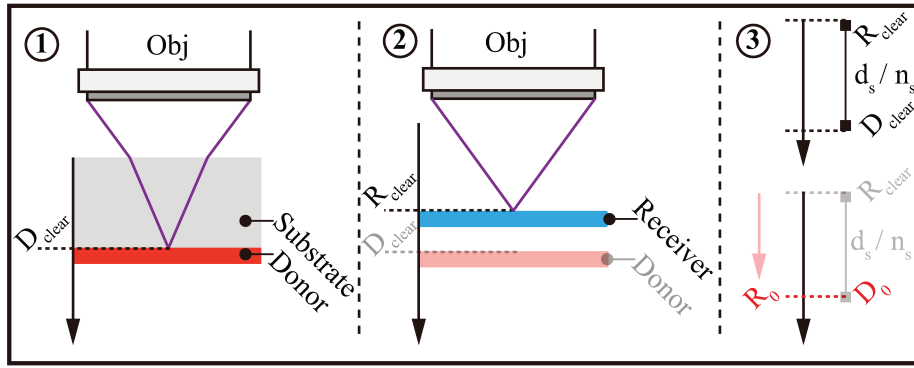

FIGURE 4.7: The position where donor and substrate interface is clearly visualized by the reflected light microscope is set as D_{clear} (1). The position where receiver surface is clearly visualized is set as R_{clear} (2). Refer to D_{clear} and R_{clear}, the zero position of donor and receiver: D_0 and R_0 are set (3).

4.2.4 Gap size determination

The adjustment and the measurement of the small gap size ($\sim 100\mu$m) between the donor and the receiver substrates is a technical challenge. Ideally, one can control the gap size on the basis of the micrometer thumbscrew of the translation stages unit (section 4.2.1). Based on the positioning system designed in this study (figure 4.1) one can define a "zero position" for both donor (D_0) and receiver (R_0) substrates thanks to the reflected light microscope which allows us to determine the "clear surface" at the focus position for both substrates. As illustrated by figure 4.7, one should remember that the position of the "clear surface" for the donor (D_{clear}) and for the receiver (R_{clear}) are different because of the refraction of the transparent donor substrate with refractive index of n_s and thickness of d_s. In order to compensate this difference, one can simply set D_0 and R_0 as:

$$D_0 = R_0 = D_{clear} = R_{clear} - \frac{d_s}{n_s}. \qquad (4.2)$$

However, this method does not provide accurate control of the donor-receiver gap. In order to precisely determine it, an optical metrology system, based on the modified microscope used for the shadowgraphy experiments, was employed. In this setup, instead of using the transmitted flashlight as the illumination source, a THORLABS QTH10 Quartz Tungsten-Halogen Lamp was used to illuminate the edge of the gap through the objective lens and visualize the small gap. To calibrate this reflected light microscope, a standard micro-rule with minimum grids of 100 μm was used (see figure 4.8 (a)). With this calibrated microscope, the accuracy of the receiver positioning based on the accuracy of the micrometer thumbscrew was investigated. Figure 4.8 (b) shows the donor and receiver, with different preset gap sizes ranging from 10 μm to 90 μm. The results show that even if equidistant steps were supposed to be used, the measured distance shows significant variations. The standard deviation is measured to be 7.4 μm, and this is most probably due to the accuracy of the thumbscrews. Thus, precise control of the receiver substrate positioning, needed to guarantee an accurate control of the gap length, requires an in-situ optical microscope monitoring before each experiment.
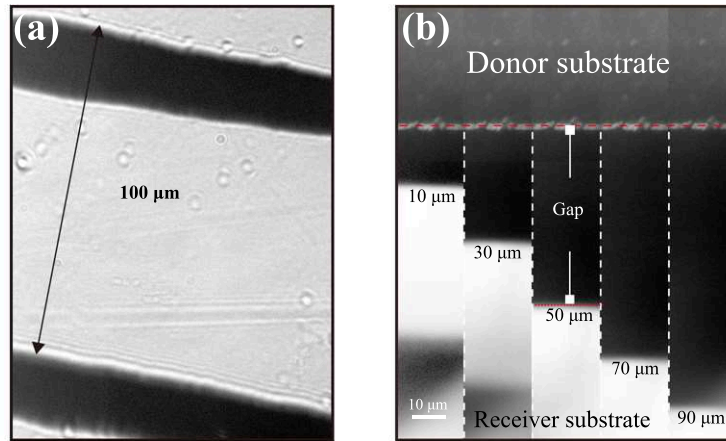
FIGURE 4.8: (a) Microscope image of a standard rule with a minimum grid of 100μm. (b) The microscope images of the donor-receiver gap with different sizes

4.3   Sample preparations

As described in chapter 2, the DP-LIFT process involves a donor substrate, coated with a solid donor film, and a receiver substrate. The physical properties and the chemical composition [105] of these substrates can have a significant impact on the ejection and deposition processes and then lead to uncontrollable results of the printed droplets. Thus, the preparation and the characterization of the properties of the donor layers and of the substrates should be detailed. In this thesis, the CORNING 2949-75×25 Microscope slides were used as donor substrates. The slide thickness was expected to be 1 mm but a variation of ±10% has been measured. The chemical composition of this substrate is detailed in table 4.2. Different donor thin films have been deposited on this glass substrate with various techniques. Before

Composition	Chemical	Proportion [%]	Boiling temperature [K]
Silicon Dioxide	SiO_2	68	2500
Sodium Oxide	Na_2O	15	2223
Calcium Oxide	CaO	5	3123
Magnesium Oxide	MgO	4	3870
Aluminum Oxide	Al_2O_3	3	3250
Barium oxide	BaO	2	2270
Boron oxide	B_2O_3	2	1860
Potassium Oxide	K_2O	1	decomposes at 623

TABLE 4.2: Chemical composition of soda lime glass [98].

material deposition, we use the ACXYS TECHNOLOGY atmosphere pressure plasma cleaner to treat the surfaces of each slide in order to increase surface energy and to enhance its adherence.

We first used the spin-coating technique in which a small amount of liquid material is deposited at the center of the substrate, and the substrate is then rotated at a high speed in order to uniformly spread the liquid by centrifugal force over the whole substrate surface. Many factors would affect the uniformity and the thickness of the film, i.e. solution concentration, substrate roughness, moisture and temperature of the room, etc. In this thesis, a LAURELL WS-400A-8NPP/LITE was used to coat silver nanoparticles ink with a silver solids content of 20 wt% and nanoparticle sizes around 100 nm. The solvents were ethanediol, ethanol, glycerine, and 2-isopropoxyethanol and the viscosity of the ink was 10 to 13 cps. With spin-coating conditions of 3000 rpm for 20 s, films of ink with a thickness of 5 μm have been prepared. Behaviors of LIFT induced jets from this silver nanoparticle ink film will be compared to those obtained with the DP-LIFT of metals.

Thermal evaporation was used to deposited thin metal film, as a donor, on the glass substrates. In the frame of this thesis, various metal sources such as copper, nickel, gold, and chromium were deposited using a EDWARD Auto 306 Cryo evaporator. Metal rods of 99.99% pure element (GOODFELLOW) is evaporated from molybdenum or tungsten boats at a pressure of $< 10^{-6}$ mBar. Donor layers with thickness varying from 150 nm to 800 nm are deposited at a rate of 1-10 Å/s. For donor layer thicker than 1 μm, a thin chromium interlayer (5-20 nm) was used for enhancing the adherence of noble metals.

4.4 Diagnostics

In order to investigate the DP-LIFT process, apart from the time-resolved shadowgraphy analysis of the ejection, the characterization of donor layers and of the deposits on the receiver after the printing process is necessary.

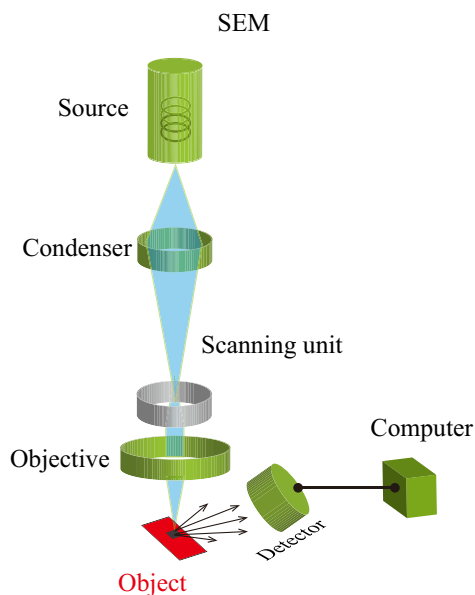To do so, several diagnostic tools were used during this thesis. Atomic

FIGURE 4.9: Schematic illustration of scanning electron microscope.

force microscopy (AFM) is a scanning probe microscopy developed to measure the surface topography at the nanoscale. In practice, AFM uses a micro-fabricated tip generally mounted at the end of a cantilever which acts as a spring. Atomic forces between the tip and the surface of interest lead to the motion of the cantilever, which induces some deflections of a laser beam being reflected on the cantilever. The measurements of these beam motions allow reconstructing the surface topography. AFM relies on the short-range repulsive force that develops when the tip approaches close enough (atomic-scale distance) to the surface. In this thesis, a PSIA XE-100 AFM was used to control the donor film thickness and also to measure the topography of printed micro- nanostructures.

Apart from AFM, a confocal and interferometry microscope (LEICA DCM 3D) was also used for the same purpose. As an optical imaging technique, it has a much shorter processing time compared to AFM. However, the resolution is lower and for some combinations of materials and substrates this measurement technique is not relevant, and the results need to be confirmed by AFM analysis.

Most of the characterization of the micro and nanostructures observed in the frame of this study, either printed on the receiver or formed on the donor, have been performed with a JEOL JSM-6390 scanning electron microscope (SEM). The electrons are emitted from the source filament, accelerated to the desired beam energy, ranging from 3 KeV to 30 KeV, and then focused by a magnetic "objective lens" on the sample surface. The incident electrons hit the sample and produce the secondary electrons which are detected by a detector set above the surface. As heavier elements are more effective at producing secondary electrons, SEM images show better contrast when a sample contains high-Z material such as Au on a substrate with low-z material such as Si. And by taking the surface flatness into account, in this thesis, to make the

observation easier, Si wafer substrate has been chosen as the receiver. In general, high accelerating voltages trend to improve the resolution, however, it also leads to more significant charging effects. Therefore, in this thesis, a relatively low accelerating voltage (5 KeV) was chosen, and for compensation, a small working distance (< 20 mm) was intentionally used.

Chapter **5**

Influence of double-pulse on LIFT

In this chapter[1] double pulse LIFT process is experimentally demonstrated in a configuration which combines a quasi-continuous pulse and a picosecond pulse. The dynamics of the formation and the propagation of the material transferred in double pulse LIFT and single pulse LIFT processes are investigated by time-resolved shadowgraphy studies. By comparing the results obtained with these two approaches, the unique features of DP-LIFT are highlighted. These investigations are extended to various donor materials to demonstrate the universality of the DP-LIFT process.

Contents

---

[1]Parts of the work present in this chapter have been published in the following articles:

- [106] Q.Li, A. P.Alloncle, D.Grojo, and P.Delaporte, "Generating liquid nanojets from copper by dual laser irradiation for ultra-high resolution printing," Opt. Express 25, 24164-24172 (2017)

- [107] Q.Li, A. P.Alloncle, D.Grojo, and P.Delaporte, "Laser-induced nano-jetting behaviors of liquid metals," Appl. Phys. A. 123, 0 (2017).

5.1 Introduction

As pointed out in section 2.1.3, in the context of the development of ultrahigh resolution laser patterning technologies, laser printing of sub-micrometric structures has been achieved by transferring melted materials from solid donor films with the single pulse LIFT technique. As previously mentioned in chapter 2, the transfer of solid material in liquid phase, when possible, requires a very specific combination of laser and material characteristics. For instance, femtosecond laser-induced jetting has only been reported with ultra-thin films of few tens of nanometers [51, 52], whereas successful transfer of nanodots in nanosecond regime requires thicker films of few hundreds of nanometers [50, 108]. This limitation arises because a single laser pulse must induce the conditions for both phase transformation and liquid jet or droplet formation. To overcome this limitation, we introduced the double pulse LIFT method [53] in which a sub-millisecond laser pulse irradiation induces the phase transformation followed by a picosecond laser pulse to provide the kinetic energy required for the formation and the propagation of the liquid jet. In this approach, the motivation of using first long pulse irradiation is to create a large, compared to the spot size of the short pulse, molten metal pool. Then, the short pulse irradiation of the liquid metal induces the fluid motion. Using time-resolved microscopy imaging, we investigated the influence of the donor film thickness on the ejection dynamics and on the related fluid motion mechanisms. For a wide range of laser fluences, we observed similar behaviors than those induced by single laser irradiation of liquid donor films. The use of a solid film allows reducing the film thickness and then the volume of transferred material, and we analyzed these results in the perspective of using this double pulse LIFT technique for additive manufacturing of nano-micro-structures with various materials.

5.2 Methods

5.2.1 Experimental setup

The experimental arrangement specifically designed and implemented in this chapter is presented in figure 5.1(a). It allows performing: single or double- pulse LIFT, time-resolved shadowgraphy of material transfer (lateral imaging) and precise positioning of laser beams and materials. The laser source used to melt the donor film is the quasi-continuous wave (QCW) laser (IPG Photonics, YLR-150/1500- QCW-AC-Y14) previously described. After the first QCW laser irradiation, a Nd:YAG picosecond laser (Continuum, Leopard S10/20) delivers, at 355-nm wavelength (third harmonic), a pulse of 50-ps duration (FWHM) which is focused at the center of the melted region to induce material ejections. To do so, both beams enter collinearly through the same microscope objective (Olympus, Plan Achromat, NA=0.40). The measured spot diameter of the picosecond laser beam at the copper-donor interface is $\sim 3.5\ \mu$m. To achieve a much larger melted area, the spot size of the QCW laser is increased by focusing the beam before the objective using
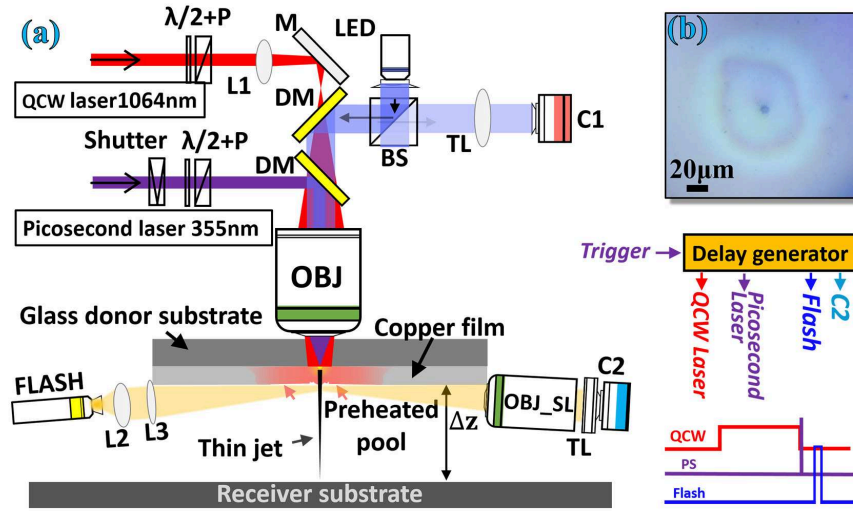
FIGURE 5.1: (a) Experimental arrangement. Beam paths of the pre-heating (QCW) and the picosecond lasers are displayed in red and purple respectively. $\lambda/2$, half-wave plate; P, polarizer; BS, beam splitter; TL, tube lens; OBJ, objective lens; FLASH, nanosecond flash lamp; OBJ_SL, super-long working distance objective lens; C1 and C2, cameras; L1, L2 and L3, lenses; DM, dichroic mirror; M, mirror. (b) Optical image of a modified region of a copper donor film after double-pulse processing. The timing sequence of the experiment has been set as that to synchronize the picosecond pulse with respect to the falling edge of the sub-millisecond pulse, and the flash illuminates the ejections with a tunable delay.

a lens. According to the observation of the modified regions, this spot diameter is about 130 μm at the copper film surface. The power of both lasers is independently adjusted using a half-wave plate and polarizer combinations. The positioning of the two beams and the systematic inspection of the donor film is facilitated by a customized reflection microscopy arrangement. As an illustration, an image of the donor copper film after double-pulse irradiation is shown in figure 5.1(b). On this image, one can see a central small dark spot corresponding to the residual crater left after the material ejection and a surrounding bright circular region corresponding to the zone pre-melted by the QCW laser pulse.

Time-resolved shadowgraphs of material ejections are recorded using a CCD camera (QImaging, QICAM) mounted on a second customized microcopy arrangement based on a long working distance microscope objective (Mitutoyo, M Plan Apo SL, NA=0.28) and a tube lens for 20$\times$ magnification. Bright-field flash illumination is provided by a NANOLITE nanosecond flash lamp (High-Speed Photo-Systeme, KL-M). The flash duration of 12 ns determines the temporal resolution of the acquisition system. A digital delay generator (Stanford Research Systems, DG645) is used to precisely synchronize, with adjustable delay, the double-pulse process with the acquisition of the time-resolved images. As shown with the inserted chronogram in figure 5.1 (bottom right), we set the double-pulse sequence by precise synchronization of the picosecond pulse with respect to the falling edge of the sub-millisecond pulse.
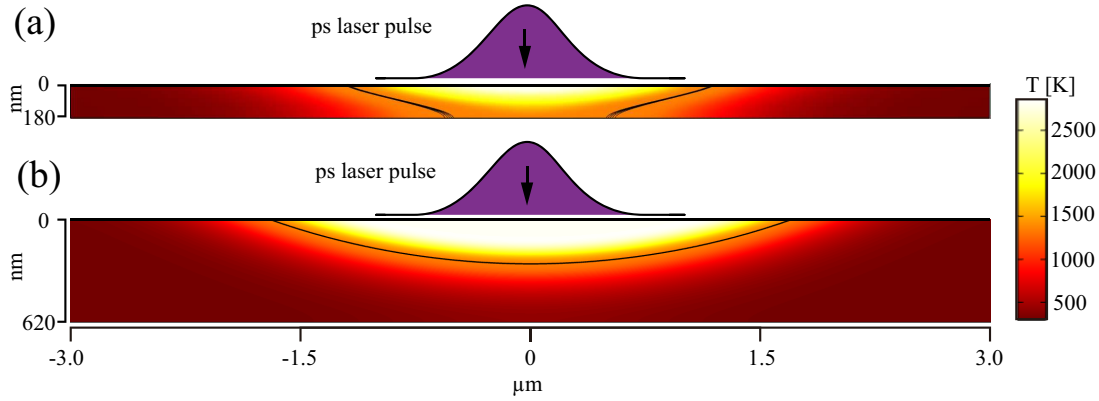
FIGURE 5.2: Single picosecond pulse (410 mJ/cm^2) induced temperature distribution at the end of the pulse within different donor films: (a) 180 nm copper donor film; (b) 620 nm copper donor film. The black arrows indicate the direction of the incident laser. The black contours on the temperature maps indicate the melting front.

5.2.2 Two-temperature model

The energy that initiates the material transfer is provided by the picosecond laser with pulse duration of 50 ps. As this laser pulse duration is of the same order of time scale than the electron-phonon relaxation time, the temperature evolution of the copper donor film should be calculated by the two-temperature model (see section 3.2).

5.3 Mechanisms of double-pulse induced transfer

5.3.1 Single-pulse induced temperature distribution

In this chapter, the characterization of the double-pulse LIFT behaviors is performed through a systematic comparison with the single-pulse LIFT for different donor film thicknesses, from 180 nm to 620 nm. The temperature distribution induced by a single picosecond pulse with a 50 ps pulse duration is calculated with the TTM. As presented in figure 5.2, for a fluence of 410 mJ/cm^2, the melting front has reached the free surface of the 180 nm copper donor film at the end of the pulse. However, for the 620 nm copper donor film and a fluence of 2000 mJ/cm^2, the melting front has only reached the depth of $\sim$ 300 nm at the end of the laser pulse.

5.3.2 Single- and double-pulse LIFT with different donor thicknesses

In practice, donor copper films with thicknesses from 180 nm to 620 nm are deposited on CORNING 2949-75×25 Microscope Slides by EDWARD Auto 306 Cryo evaporator. Figure 5.3 presents shadowgraphy images of material ejections from those films obtained for both single-pulse and double-pulse LIFT experiments while the laser fluence is varied. To compare the typical features

in each situation, the delay for shadowgraph imaging has been adjusted in the range 250-300 ns depending on conditions.

180 nm copper donor film

Figures 5.3(a1)-5.3(a3) show ejections from a 180 nm copper film induced by a single picosecond pulse irradiation. Ejections under similar situations have already been observed and explained [23]: for low and intermediate fluence regimes (F $\leq$ 720 mJ/cm^2), cap-like and elongated features (also called jet-like) are observed, and for the high fluence regime (F $\geq$ 1000 mJ/cm^2), un-controllable spraying processes occur. The physical mechanisms corresponding to each regime are thermally-induced stress for the cap-like regime, fluid motion of the melted layer for the jet-like regime and partial evaporation for the spraying regime [23]. For comparison, figure 5.3(a4)-5.3(a6) show ejections induced by double-pulse LIFT corresponding to conditions similar to those of the single-pulse experiments except that a first-pulse of 120 μs duration and 2.57 mJ energy (QCW laser) is applied to melt the film before the material ejection. We can observe that the ejection dynamics are very similar to those generated by a single laser pulse, whatever the ps laser fluence.
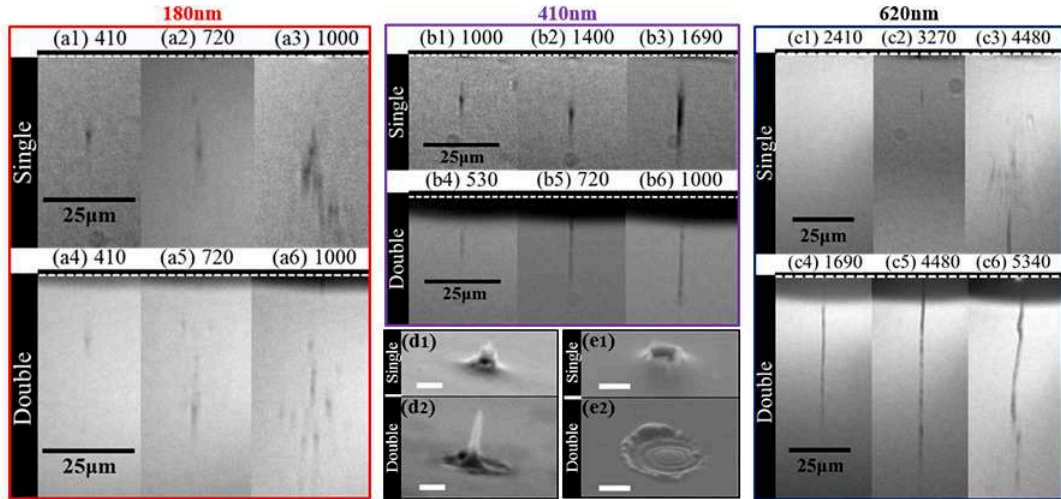
FIGURE 5.3: Shadowgraph imaging of the ejection from copper films of different thicknesses: (a) 180-nm, (b) 410-nm, (c) 620-nm. (a1-a3), (b1-b3) and (c1-c3) are ejections induced by single picosecond pulses with different fluences given at the top of each image (unit: mJ/cm^2). (a4-a6), (b4-b6) and (c4-c6) are ejections induced by double-pulse LIFT with different picosecond pulse fluences given at the top of each image (unit: mJ/cm^2) and a first pre-melting pulse with respective duration and energy of 120 μs and 2.6 mJ for 180-nm films, 200-μs and 4.3 mJ for 410-nm films and 250 μs and 13.4 mJ for 620-nm films. (d1) and (d2) are SEM images of the residual crater left on the 410-nm donor film after single (b1) and double (b6) pulse LIFT (scale bars: 1 μm). (e1) and (e2) are residual craters left on the 620-nm donor film after single (c2) and double (c5) pulse LIFT (scale bars: 2μm). For each ejection image, the white dash line stands for the location of the donor film and the shady region near the donor film is due to tilted imaging and laser-induced changes of the surface reflectivity.

To explain these observations, we must consider the depth of melted volume l_{th} induced by the picosecond pulse. According to TTM calculations presented in section 5.3.1, when a 180 nm thick copper film is irradiated with a 50 picosecond pulse and a fluence of 410 mJ/cm^2 the melting front reaches the free surface before the end of the pulse. Under this condition, it is possible to achieve the melting through its whole thickness of the donor film with or without the QCW preheating. And if the LIFT laser fluence can be properly chosen in order to get an ideal proportion of the vaporized propellants and the melted donors, controllable ejection can be expected.

410 nm copper donor film

To further investigate the differences, we have repeated the experiments with a 410-nm thick copper donor film. For the double-pulse LIFT ejections shown in figure 5.3(b4)-5.3(b6), the formation of stable, uniform and long jets is observed over a range of laser fluences from 530 to 1000 mJ/cm^2. The subsequent re-solidified jet at the donor substrate surface obtained in these conditions, shown in figure 5.3(d2), points out the motion of the melted copper at the donor free surface. This image confirms that the ejection mechanism is based on a fluid mechanic process [52]. All images of ejection have been captured at the same delay of 280-ns, thus the difference of lengths is related to the increasing jet propagation velocities with the deposited energy. For single-pulse LIFT [see figure 5.3(b1)-5.3(b3)], we observe when increasing the fluence, a significant elongation of the jet-like behavior. In this configuration, the copper film thickness (410 nm) is 2.5 times larger than the thermally affected depth in the picosecond pulse duration. Then, a laser fluence value can be found for inducing the melting of the whole layer together with the vaporization of a suitable amount of copper at the interface with the glass substrate to induce enough force for fluid motion and jet formation. As suggested by M. Zenou et al. [24], when the melted material front reached the free surface there exist some solid barriers around the central melted region leading to a so-called thermally induced nozzle (TIN) transfer. Figure 5.3(d1) shows such a quasi-nozzle at the donor surface that illustrates this process. It is worth noting that even if we qualify the process as jet transfer because of the elongated shape of the material seen in the shadowgraphy images, the jets are not as uniform and well-defined as those of the double-pulse LIFT [see figure 5.3(b4)-5.3(b6)] highlighting the differences of mechanisms occurring in single and double-pulse LIFT.

620 nm copper donor film

For further investigation and to enhance these differences, we also used a 620-nm thick copper film as a donor. As presented in section 5.3.1, under the laser fluence of 410 mJ/cm^2, the melting front can only reach a depth of ∼300 nm, when the vaporized propellants formed and started to push the transferring materials. Therefore, as transferring materials moved, they would encounter a thick (∼300 nm) solid barrier near the free surface. Due to
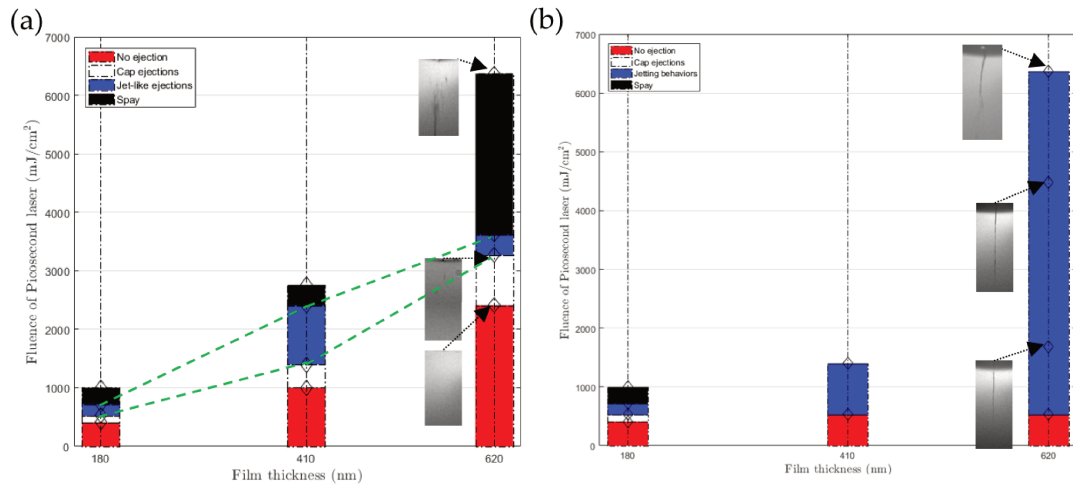
FIGURE 5.4: Regimes of ejection as a function of the ultrashort pulse laser fluence for the single pulse LIFT (a); and the double pulse LIFT (b) for three different thicknesses of the donor copper film.

those facts, it would be difficult to achieve stable transfers (less debris) under this condition.

For single-pulse LIFT, when the fluence is lower than 2410 mJ/cm^2 [refers to figure 5.3(c1)], the copper film is not fully melted or evaporated, as expected from the TTM model (see figure 5.2), and the deformation force generated in the confined interaction volume is not strong enough to induce any material transfer. For a medium fluence such as 3270 mJ/cm^2 [refers to figure 5.3(c2)], a TIN transfer is obtained. The corresponding quasi-nozzle on the donor film is shown in figure 5.3(e1). For higher fluences such as 4400 mJ/cm^2 [refers to figure 5.3(c3)] the free surface is melted leading to the formation of a well-defined liquid jet (partially visible at the bottom of the image), but the energy required to melt the full thickness also generates a large amount of vaporized copper which induces a spray-like ejection behind the jet. In these cases, the deposition becomes hardly controllable and debris are systematically found on the receiver substrate (not shown here). By contrast, in the double-pulse LIFT mode of operation, the energy of the picosecond laser pulse is systematically deposited in a fully melted liquid layer thanks to the irradiation with the QCW laser pre-pulse. This makes possible the formation of stable, uniform and long jets over a large range of fluences as demonstrated by the images of the ejections shown in figure 5.3(c4)-5.3(c6). These jets are observed with lengths exceeding 60 μm and the fluence process window for the jet formation with the picosecond laser ranges from 1690 mJ/cm^2 to 4480 mJ/cm^2. Moreover, figure 5.3(e2) presents an SEM image of re-solidified copper on the donor surface after such double-pulse LIFT. In this thick copper film case, the observed ripples are due to fluid motion in the melted copper pool and revealed here by the fast re-solidification process.
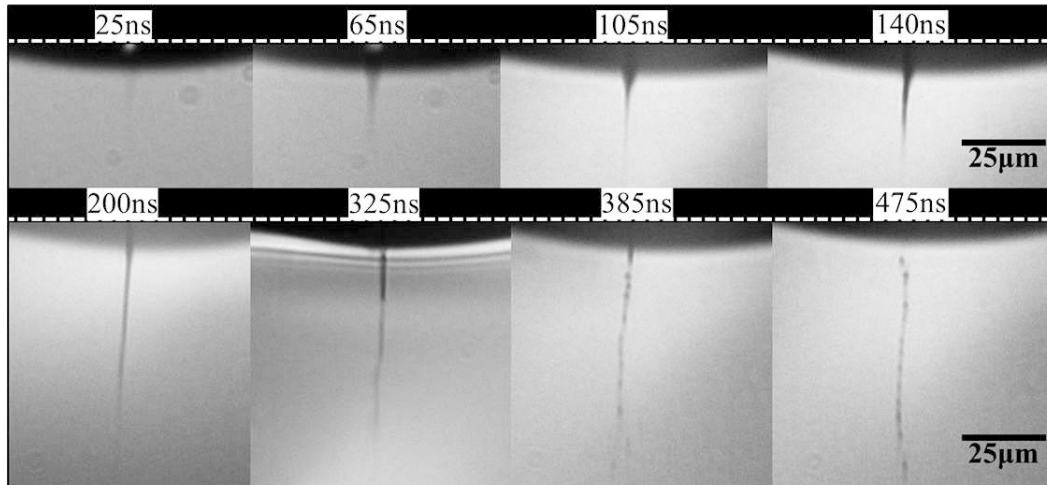
FIGURE 5.5: Time-resolved shadowgraphy images acquired for double-pulse LIFT with a 620-nm copper film.

Summary

Finally, the graph of the figure 5.4 summarizes the increase of the process windows in terms of laser fluence and donor film thickness when using the dual laser printing compared to the single laser printing. For this latter configuration, one can observe that the process window to form a stable liquid metal jet with a picosecond laser irradiation is optimum for specific film thickness, while stable jets are achievable for a large range of film thicknesses in double pulse LIFT mode of operation.

5.3.3 Time-resolved shadowgraphs of double-pulse induced copper jets

For further investigation of these jetting behaviors, time-resolved images of double-pulse LIFT from a 620-nm copper film are shown in figure 5.5. As for figures 5.3(c4)-5.3(c6), a first-pulse with 250-μs duration and 13.4-mJ energy pre-melts the copper film and a picosecond pulse with 3620-mJ/cm^2 fluence induces the transfer that is imaged for different delays from 25 to 475 ns. As previously observed [37], the transfer process starts with the surface deformation, that can be attributed to the generation and the expansion of a localized vapor pressure due to the evaporation of the copper at the film-substrate interface, inducing the fluid motion and the jet formation. This deformation has a triangular shape and can be observed until a delay of about 150 ns. Then, the jet progressively elongates reaching its longest and most uniform morphology at 200 ns. Eventually, for delays exceeding 325 ns, the jet detaches from the donor surface and furthers breaks up into droplets due to the Rayleigh-Plateau instability [109]. Therefore, when the gap between donor and receiver is large (> 50 μm in the discussed situation), this instability may result in pieces of the jet that break off and are deposited as satellite droplets on the receiver. This dynamics of the jet formation and expansion is similar

to the one observed for the LIFT of silver nanoparticle inks in the picosecond regime [77]. Interestingly, melted copper and silver inks exhibit both a viscosity of few millipascal-seconds [110] making reasonable the hypothesis of identical fluid motion mechanisms. It is worth noting that the fluences required to initiate these jets are more than one order of magnitude higher for melted copper than for silver inks. That is due to first the low evaporation temperature of ink solvents compared to bulk copper and second the higher material density of copper compared to silver inks containing only 20% of metal.

5.3.4   Printing results and discussions

When a single 50 ps picosecond laser beam irradiates the thick (e.g. > 180nm) solid metal film through the glass substrate, the temperature gradient induced in the metal can lead to the formation of three phases: a solid layer near the metal-air interface, a "vaporized material" layer near the donor-substrate interface and a liquid layer between the two previous ones. The thickness of each layer depends on the laser fluence and the time delay after the irradiation. The importance of these layers has been discussed in [23]. The pressure increase in the volume of the vaporized layer will provide the kinetic energy required to induce the fluid motion, and eventually to break the solid layer in order to form a thermally induced nozzle (TIN) as suggested in [24]. As a first conclusion, our observations suggest two critical prerequisites for the formation of liquid copper jets: first, the donor film must be melted over its full thickness; second, the local temperature and pressure conditions at the substrate-donor film interface must be high enough to induce a partial vaporization of the film and generate a sufficient deformation force. These criteria are obviously difficult to fulfill together with single pulse irradiation and, when successful, lead to very narrow and material-specific processing windows [51]. Interestingly, we show that the use of a QCW laser allows to locally rise uniformly the temperature of the film, and ultimately it is melting over its full thickness. Then, the subsequent irradiation with a short laser pulse brings the appropriate amount of energy required to induce the jetting mechanisms. This dual-laser method provides the freedom to accurately control the film properties and the material transfer independently. In double pulse LIFT mode, the picosecond laser irradiates a premelted liquid layer, and its unique purpose is to vaporize a sufficient volume of the layer near the substrate-donor interface in order to raise the pressure in this confined volume and provide the kinetic energy required to induce the fluid motion. In this configuration, the jet formation relies on the volume expansion of the vaporized metal and the mechanisms are similar to those described for the blister LIFT [45].

Finally, to demonstrate the potential of this double-pulse approach for the printing in liquid phase of initially solid materials, we have set a silicon receiver substrate at $\approx 55~\mu$m in front of the donor substrate and used the same conditions as those described in figure 5.3(b6) to form a uniform thin jet. In this experiment, we repeated the double-pulse LIFT at different locations of
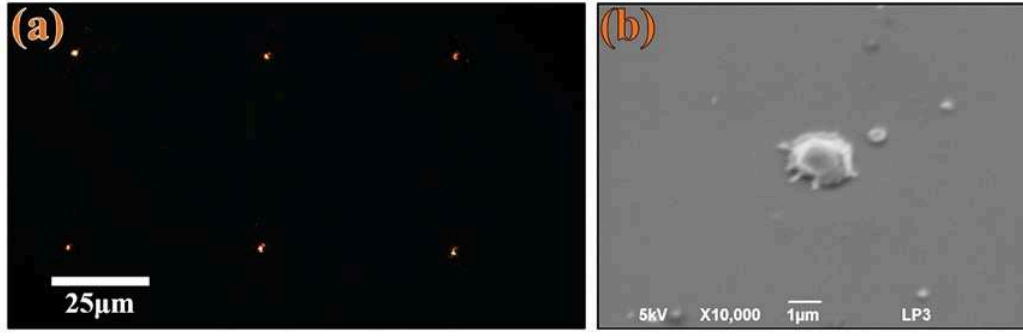
FIGURE 5.6: (a) Array of copper droplets printed by double-pulse LIFT from a 410-nm donor film. (b) SEM image of a single copper droplet of this array.

the receiver surface separated by 50 μm to print a regular array of copper droplets. Figure 5.6(a) presents an optical image of a region of the printed array. Because of the small size of the droplets, near the resolution limit for wide-field microscopy, we have used dark-field microscopy for contrasted imaging of the feature locations. Figure 5.6(b) is an SEM image of a typical solidified copper droplet printed on the receiver. Each droplet exhibits a diameter of around 1.5 μm. The process is not fully optimized, we can observe a few nano-droplets next to the main one. They are due to the breaking of the thin copper jet before reaching the surface. However, the transfer of the melted metal in jet ejection regime avoids the generation of debris generally observed with single pulse LIFT in the cap or spray ejection regime [25, 23]. The generation of long and stable liquid metal jets thanks to the double pulse LIFT approach will help the printing of debris-free structures.

5.3.5 Summary

In this section, the DP-LIFT process is first demonstrated. The features of DP-LIFT process have been investigated by time-resolved shadowgraphy and systematically compared to single-pulse LIFT. This study shows that the ejection mechanism is similar to the printing of inks with a single laser pulse and that the DP-LIFT approach applied to copper allows the formation of long and stable liquid metal jets with unprecedentedly wide process windows. These results also point out the current limitation of this setup to address the challenge of nano-printing. The transfer of sub-micrometer pixels should require the use of a thinner metal film, and in such conditions, the generation of a temperature gradient to vaporize only a small layer of the film makes the use of an ultrashort pulse, in the femtosecond regime, more relevant.

5.4 DP-LIFT with variable materials

5.4.1 DP-LIFT with Au donor films

In order to demonstrate the universality of DP-LIFT technique, we performed DP-LIFT experiments with different configurations of donor films such as Au

and Ni-Cu double-layer.

Gold jets induced by single femtosecond laser pulse have previously been reported by using an ultra-thin 60-nm donor film, and the maximum observed jet length was approximately 5 μm [51]. In this article, thanks to the double-pulse process, gold films with a thickness of 370 nm have been used to generate laser-induced long nanojets. The first pulse with 150-μs duration and 3.3-mJ pulse energy was applied for pre-melting the film. The picosecond pulse was then used to initiate jetting with different fluences: 520-mJ/cm^2, 860-mJ/cm^2 and 1380-mJ/cm^2. Figs. 5.7(a)-5.7(c) present the time-resolved shadowgraphy images of the jetting induced with these different laser fluences.

For low and intermediate laser fluences (520-mJ/cm^2, 860-mJ/cm^2) the jetting behaviors are similar to those previously discussed for the 620-nm Cu film. In this region stable jets as long as 35-μm has been observed. For delays longer than $\sim$ 440 ns the jets become too thin and, as for copper, pinch-off into droplets. For the highest tested laser fluence (1380-mJ/cm^2), the jet exhibits strong instabilities due to turbulence.

5.4.2   DP-LIFT with Ni-Cu double layer donor films

A major advantage of the proposed double-pulse LIFT methodology is its flexibility. As we have shown, it can be applied to pure metal films over a large range of thicknesses, but may also be considered for multiple layer structures. To investigate this aspect, we have performed experiments with double-layer films consisting of a 200-nm Ni layer deposited on a glass substrate and covered by a 400-nm Cu film. For pre-melting this structure, the first pulse with 50-μs duration and 1.1-mJ pulse energy was applied. To initiate the jet formation and propagation, different fluences for the second pulse have been used. Figures 5.8(a)-5.8(c) present the SEM images of the donor film after the process for these different laser fluences. The time-resolved shadowgraphy jetting images acquired for each fluence conditions are presented in Figs. 5.8(d)-5.8(f) correspondingly.

Near ejection threshold

By careful observations of the donor surface modifications with a scanning electron microscope (SEM), one can expect an ejection threshold of $\approx$ 1720 mJ/cm^2 for this Ni-Cu double-layer film. For laser fluences slightly above the ejection threshold, the limitations of our time-resolved imaging setup don't allow us to visualize any material ejection. However, as presented in Fig. 5.9(b), metal droplets are collected onto a silicon substrate (receiver) sets in front of the donor substrate with a 50-μm gap. These observations don't allow us to determine if the transfer occurred as an ultra-thin jet or as a droplet. However, the SEM image of the donor surface [Fig. 5.9(a)], showing a nano-droplet at the top of a bump suggests a different mechanism than the jetting observed for the other conditions (figure 5.5 and figure 5.7) where frozen jets or ripples are always present. So, we believe that the thermal stress induced in the liquid layer leads to its expansion and to the ejection of a droplet. In
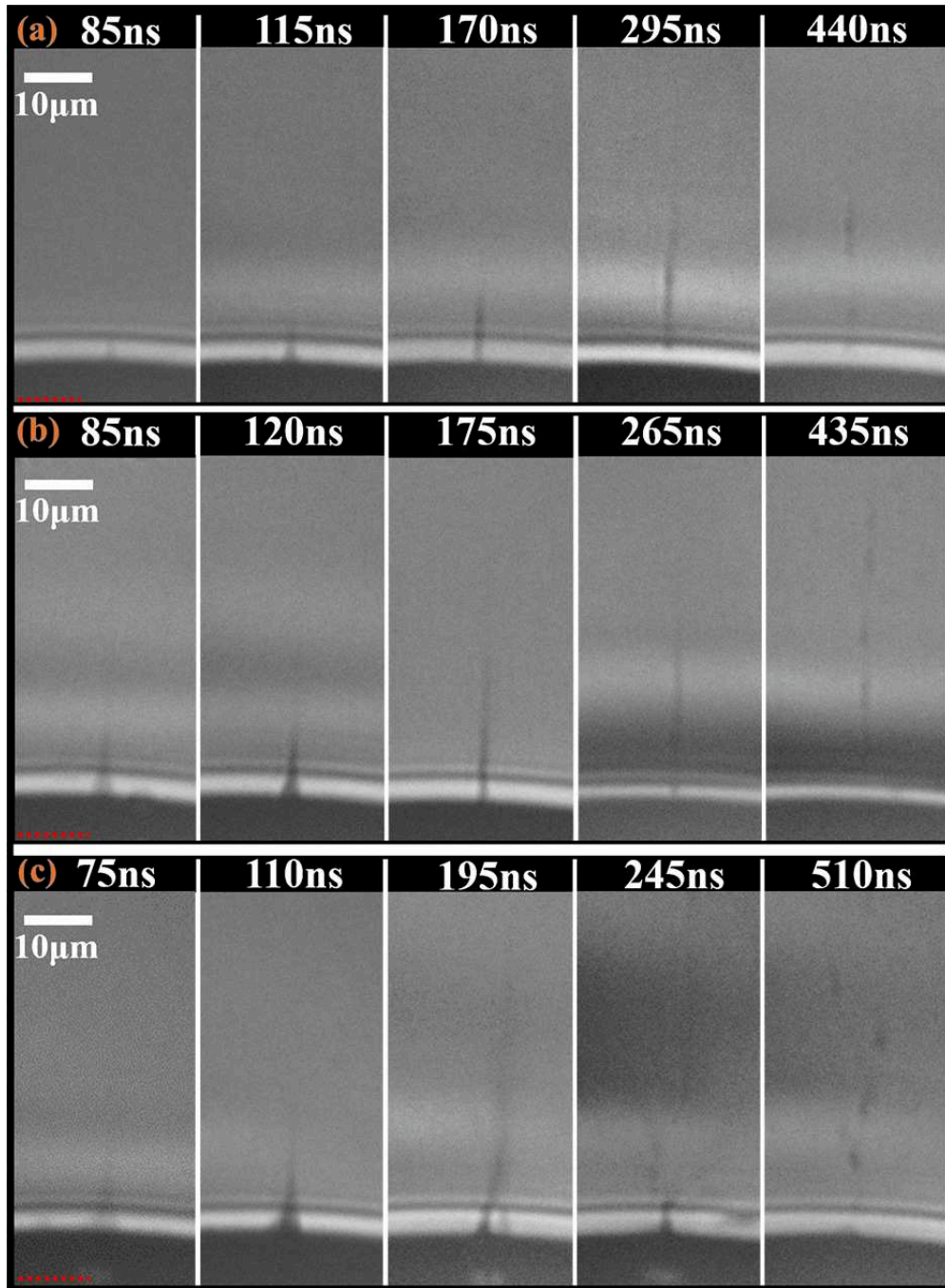
FIGURE 5.7: Time-resolved shadowgraphy of the material ejection induced by the irradiation of a 370nm thick gold film in DP-LIFT mode. Different laser fluences of the second pulse: (a) 520 mJ/cm^2, (b) 860 mJ/cm^2 and (c) 1380 mJ/cm^2 have been applied.
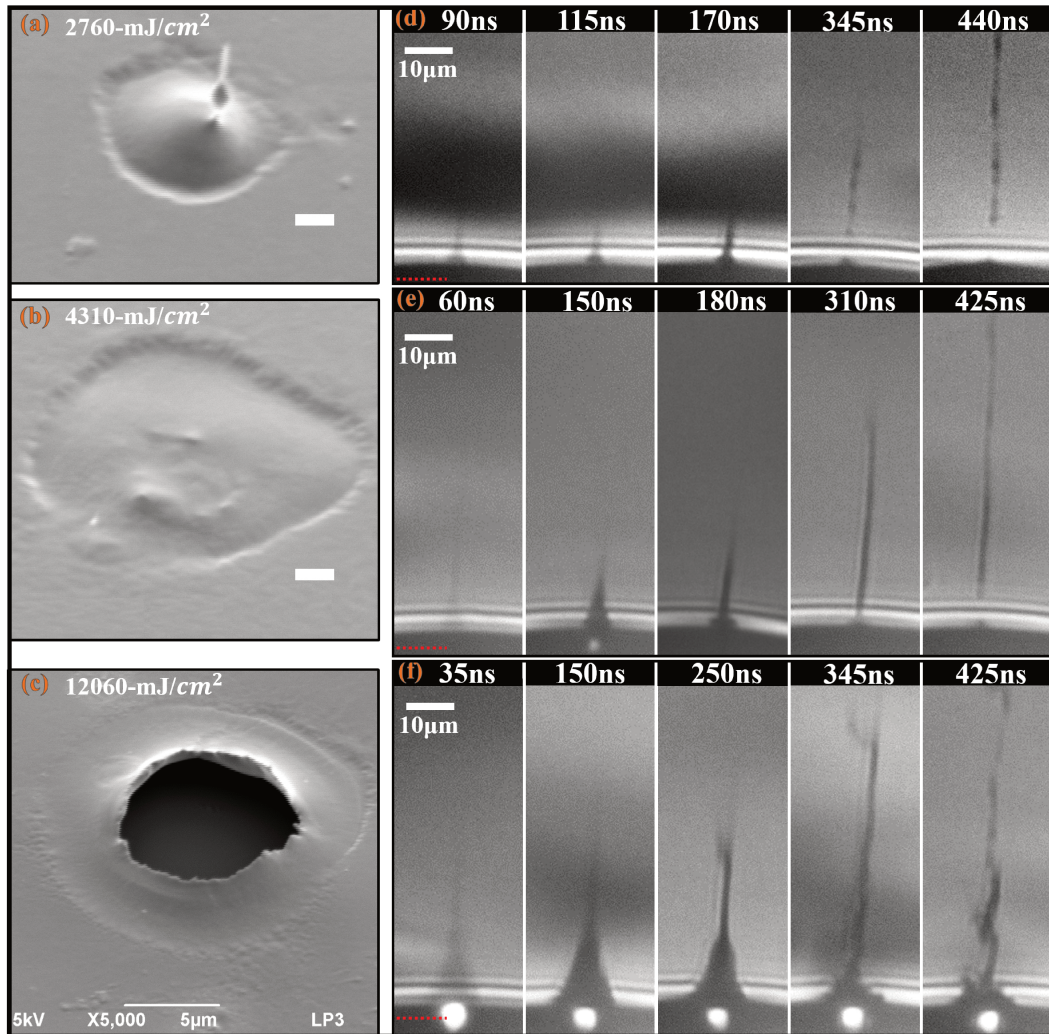
FIGURE 5.8: (a), (b), (c) SEM images of residuals left on Ni-Cu double layer donor films. Scale bars: 1-μm. (d), (e), (f) Time-resolved shadowgraphy of the jetting behaviors. Different laser fluence of the second pulse: 2.7 J/cm^2, 4.3 J/cm^2 and 12 J/cm^2 have been applied correspondingly.

order to characterize such ejection process which relies on a capillary-inertial energy balance [23], the threshold Weber number is used:

$$We_{ej} = \frac{\rho d_l V_{ej}^2}{\gamma} = \frac{E_{in}}{E_{cap}} \tag{5.1}$$

Where $d_l \sim 600$-nm is the thickness of the liquefied layer, V_{ej} is the ejection velocity and γ is the surface tension of the liquid copper. Material ejection only occurs if inertial energy is larger than capillary energy, i.e. $W_{ej} > 1$. As we are close to the threshold ejection, the corresponding Weber number is slightly higher than one and the corresponding ejection velocity is around 20 m/s. Within such short transfer distance, the air drag effect can be neglected and that allows assuming that the impact velocity on the receiver as $V_{im} = V_{ej}$. The diameter of the droplets d_{sp} are ~ 1 μm, thus the impact Weber number We_{im} can be approximated as:

$$We_{im} = \frac{\rho d_{sp} V_{im}^2}{\gamma} \approx 2 \tag{5.2}$$

With this low Weber number, the droplet can hardly spread [111] on the receiver and solidified as the shape of a pie.
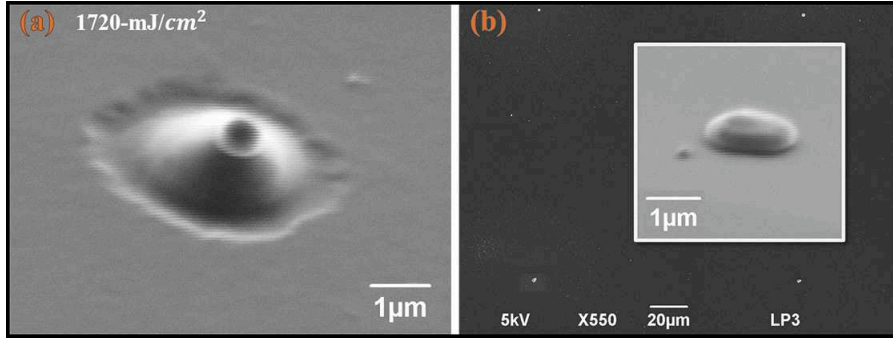
FIGURE 5.9: Characterization of the donor and receiver substrates after DP-LIFT process applied to a Ni-Cu double layer donor film with fluence of 1720 mJ/cm^2, slightly above the ejection threshold fluence (a) SEM image of the irradiated area of the donor film (b) Droplets collected on the receiver.

Laser-induced liquid alloy jetting

By increasing the laser fluence, more kinetic energy will be transferred to the liquid metals composing the film to break the capillary-inertial energy balance. For high laser fluences (≥ 2.58 J/cm^2), figure 5.8 shows that metal jets start to form from the surface of the donor film.

More precisely, in figure 5.8(d), a ps laser fluence of 2.7 J/cm^2 was applied. After this second pulse irradiation, the jet evolution is similar to what previously observed for gold and copper films. Before breaking the jet starts to pinch-off due to surface tension effects [112]. The optical resolution limit of our observation system does not allow us to fully resolve the features of

FIGURE 5.10: SEM images of droplets collected on the receiver under ejection fluence of 2760-mJ/cm^2 from Ni-Cu donor film. The scale bars of the left two side-view images are 1-μm. The right image shows a part of the printed droplets matrix.

the pinching. However, thanks to the rapid re-solidification of liquid donor metals, the jet morphology at the pinching time can be 'frozen' to provide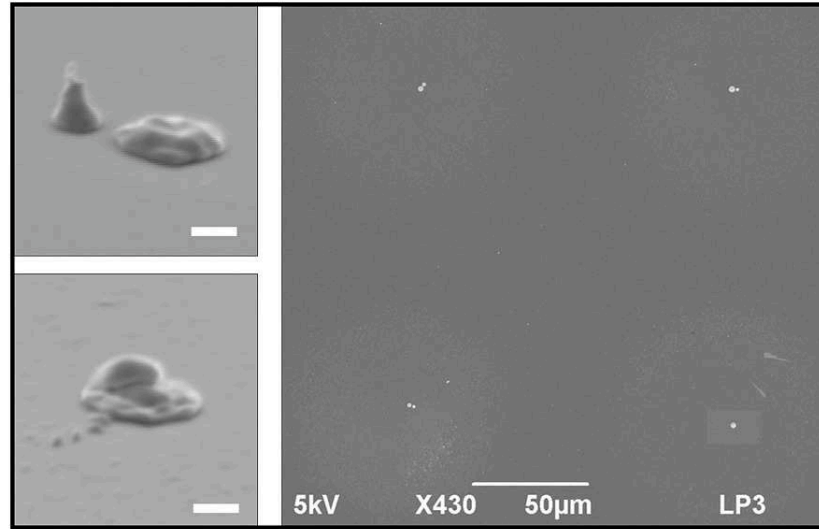 us with a chance for postmortem SEM analysis. In figure 5.8(a), the SEM image shows the so-called "bead-on-string" pinching phenomenon (stretch a glob of saliva between your thumb and forefinger, and you should see it). In fact, only a non-Newtonian fluid can expect such a viscoelastic effect [113], and this leads us to conclude that during the dual-pulse process the copper layer has mixed with a small amount of nickel to form a multicomponent liquid.

We can observe from figure 5.8(d) that when the length of the jet is $\sim 50\ \mu$m, it already starts to break. That means this breaking occurs before reaching the receiver substrate. SEM images presented in figure 5.10 shows how the liquid metal wets the receiver under this condition. As shown by the side-view images, thanks to the higher inertial energy, droplets spread further than the ones transfer at the threshold fluence [figure 5.9(b)]. However, multi-droplet deposition is also observed due to the jet break-up.

In figure 5.8(f), a high laser fluence of ≈ 12 J/cm^2 was applied, leading to high Weber number ejections ($We_{ej} > 125$). In this condition, the jetting behaviors are no longer stable. The SEM images presented in figure 5.11 show the transferred material collected by the receiver. The side-views of these printed structures show different wetting phenomena. It can be observed that the largest part of the transferred metal exhibits a strong spreading effect, due to its high inertial energy, while some droplets, coming from the breakup of the jet, have also been collected. Even if these high fluence conditions are not relevant to perform high-resolution printing, it must be pointed out that jets are still generated with fluences seven times higher than the threshold. The use of such strong irradiation conditions with pure metal films or nanoparticle ink donors would have led to spray-like ejection without the formation of a jet [37].
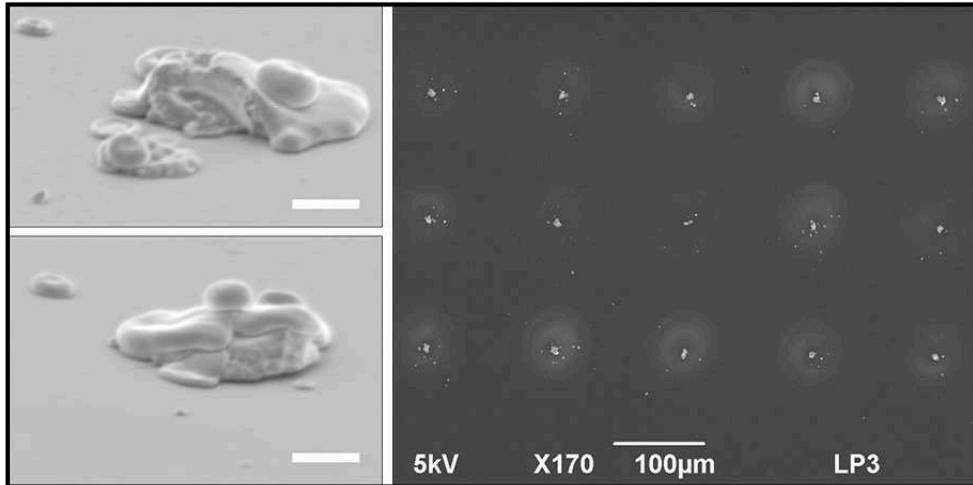
FIGURE 5.11: SEM images of droplets collected on the receiver nder ejection fluence of $\approx 12 \, \text{J}/\text{cm}^2$ from Ni-Cu donor film. The scale bars of the two left side-view images are 2-μm. The right image shows a part of the printed droplets matrix.

5.4.3 Summary

In this section, time-resolved studies of double-pulse induced jetting have been performed with different metals films and for increasing picosecond laser fluences. From the discussions of the jetting behaviors presented in figure 5.5, figure 5.7 and figure 5.8, it appears that they look very similar to those observed in blister mode in which the fluid motion is mechanically initiated [76]. This points out that in double pulse LIFT mode the initial fluid motion is less dependent on the material properties than in single pulse LIFT mode of a metal layer. Moreover, the use of thick layers and large melted pool, induced by the QCW irradiation, allows one to generate stable jets over distances of few tens of micrometers and then increase the process window of the printing technique. By analyzing the average ejection velocity, we also provide a relation between the laser fluence of the second pulse and the ejection Weber number We_{ej}. As a summary, this relation is presented in figure 5.12. It shows that the Weber number determined for the ejections generated from the Au film increase rapidly with the laser fluence. In contrast, the increase of Weber number for the ejections coming from the Ni-Cu double-layer film is much slower compared to Au or Cu films. Among the different reasons to explain this effect (optical absorption, density, surface tension...) we want to point out the specific mechanical properties of this two-layer film in the liquid phase which slow down the transfer. Despite the complexity of these aspects, these results can serve as a guide to help in finding the appropriate way of printing droplets of a chosen material and with a desirable shape.

5.5 Conclusion

In this chapter, we have reported the formation and expansion of liquid metal jets from a solid metal film thanks to a double-pulse irradiation process. Long
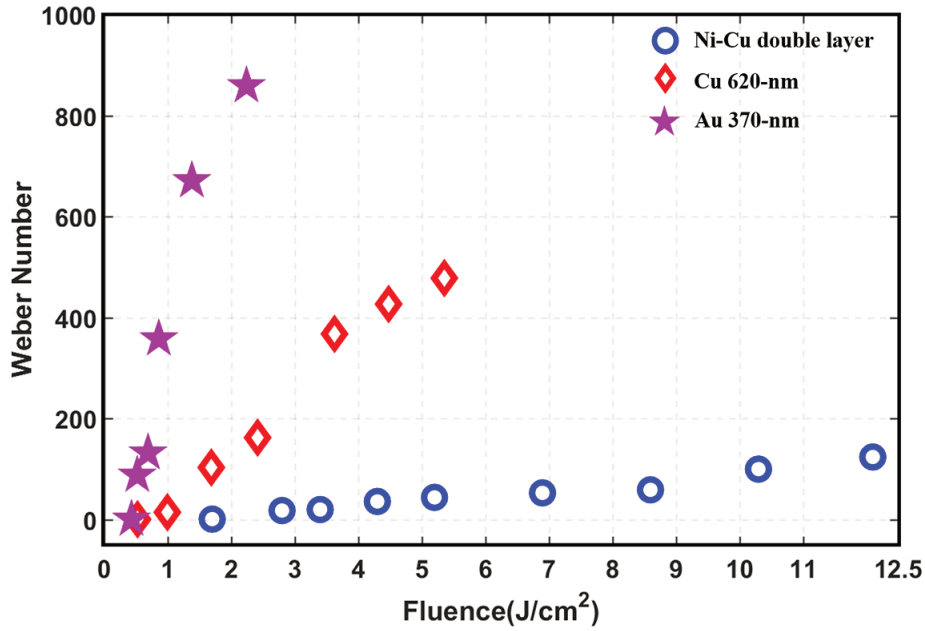
FIGURE 5.12: Relation between the laser fluence of the second pulse and the ejection weber number We_{ej} for different donor films.

and stable liquid metal jets have been observed for a wide range of irradiation conditions and film thicknesses. We have concentrated the demonstration on copper, gold, and bilayer of metals, but the concept is general and can be directly extended to any other pure metals, alloys, and semiconductors. With the use of shorter laser pulses, typically femtosecond ones, this approach becomes also compatible with the material transfer from ultra-thin films, which appears to be a challenging requirement for the reliable printing of nanodots [13]. This must open a way for the flexible synthesis of 3D microstructures (e.g. bio-inspired architectures) and ultimately advanced nanomaterials such as metasurfaces and 3D photonic crystals which are today not accessible by LIFT.

Looking at the future, those studies not only provide an interdisciplinary vision to investigate the sub-micrometric fluid phenomenon but also opens a way for the challenging fabrication of microdevices or architectured multi-materials. However, before jumping into the level of applications, further investigations on the driving mechanism of this novel process should be carefully addressed. Therefore, the next chapter is dedicated to studying the parameters that control the dynamics of the DP-LIFT process.

Chapter 6

Dynamics of DP-LIFT

In this chapter[1] dynamics of double pulse laser printing of copper is discussed. Temperature evolution of the thin copper film induced by the first-microsecond pulse is calculated. Characterizations of ejection events under different temperatures are discussed based on time-resolved image sequences and SEM images of the donor film. For a given copper temperature, visualizations of ejections reveal different ejection modes under different LIFT laser fluences. Governing physics are discussed based on energy balances.

Contents

---

[1]Parts of the work present in this chapter have been published in the following articles:

- Q.Li, D.Grojo, A. P.Alloncle and P.Delaporte, "Dynamics of double pulse laser printing of copper microstructures," App. Suf. Sci (2018) **[Under review]**

- Q.Li, D.Grojo, A. P.Alloncle and P.Delaporte, "Jetting regimes of double pulse laser-induced forward transfer," (2018) **[To be submitted]**

6.1 Introduction

In chapter 5, the DP-LIFT process has been successfully applied to generate liquid nano-jets without debris from solid donor film and consequently transfer various materials (Cu, Au, Ag, Ni) on a receiving substrate with well-defined and clean depositions. However, due to the complexity of the physics driving the double pulse process, the mechanisms governing this novel laser-induced jetting and deposition phenomenon are not fully understood, yet. LIFT related jetting phenomenon from low viscosity liquid donor has been extensively studied by several groups experimentally [10, 17, 114, 115] and numerically [45]. These studies point out that the jetting mechanism is initiated by the generation of a local overpressure at the interface liquid film and donor substrate. This leads to the fluid motion induces by the corresponding forces(cavitation bubble, deformation of an intermediate layer) that push the liquid towards the free surface. However, in the DP-LIFT situation, the typical thickness of the donor film is below 1000 nm, and thus, such a cavitation bubble driving mechanism would require a strong downscaling of the bubble size and make it unlikely. Besides, laser-induced nano-jetting from ultra-thin (< 1000 nm) solid donor films has been reported and investigated experimentally [116, 13, 49, 50, 51, 117, 118] and theoretically [83, 119, 120]. In these experiments, an ultrashort pulse irradiates the thin film with a Gaussian beam profile which induces a Gaussian distributed pressure force in a film melted over its full thickness in the irradiated area. Under appropriate conditions, the molten film can detach from the substrate with the shape of a dome shell. Within this dome shell, the normal component of the capillary force decelerates the normal velocity of the shell and the parallel component leads to the displacement of the shell material towards the center. Taken these effects altogether, a jet starts to form when the reverse motion of the shell begins [83]. A difference with the DP-LIFT situation is the diameter of the melted area which is only 1 to 2 orders of magnitude larger than the dimension of the ultrafast laser spot used in DP-LIFT. The larger liquefied areas (volumes) allow a stronger center-ward motion and make the jet initiation and pinching processes different from the above-mentioned configuration. For these reasons, the dynamical aspect associated with DP-LIFT remains unclear and requires further investigations. Looking at the already performed DP-LIFT experiments [69, 72, 53, 107], even though they have demonstrated the unique feature of DP-LIFT and the liquid metal jetting behaviors, they have not been performed to study the double-pulse laser printing dynamics. By comparing the calculated temperature dynamics initiated in the film with the pre-pulse and the experimental observation of both the ejection dynamics and the printed structures, we intend here to investigate the dynamical aspects involved in DP-LIFT to improve the physical understanding of the jetting behavior, as well as to optimize the performance of this process for digital micro- nano-printing.
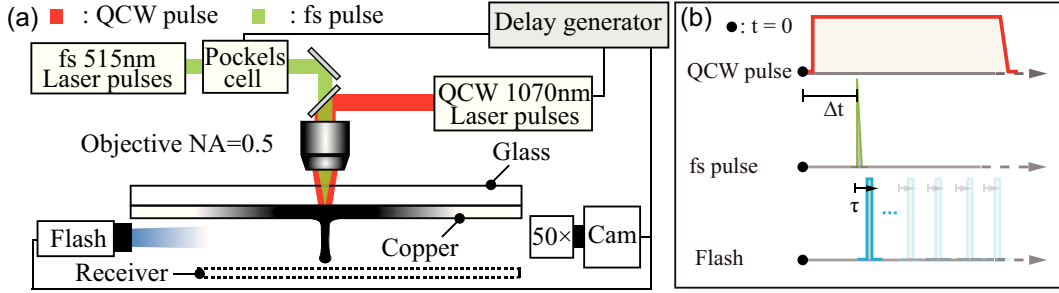
FIGURE 6.1: (a) Sketch of the experimental setup for DP-LIFT. The femtosecond LIFT laser beam is represented in green and the QCW laser beam in red. Illumination flash light is shown by the blue color. (b) Time chart of events for synchronization of the DP-LIFT and time-resolved observations.

6.2 Methods

6.2.1 Experimental setup

DP-LIFT experimental arrangement has been described in section 4.2.1. In this chapter, in order to investigate the various aspect of the DP-LIFT, the experimental arrangement is specifically designed and depicted in figure 6.1. The laser source used to achieve the melting of the donor film is the quasi-continuous wave (QCW) laser (IPG PHOTONICS YLR-150/1500-QCW-AC-Y14) emitting, at 1070-nm wavelength, pulses of variable duration from 50 μs to the continuous wave operation. Following this first QCW laser irradiation, a AMPLITUDE SYSTEMES S-Pulse HP femtosecond LIFT laser delivers, at a 515 nm wavelength (second harmonic), a 500 fs duration (FWHM) pulse focused at the center of the melted region to induce material ejections. To do so, both beams enter collinearly through a long working distance MITUTOYO M Plan Apo 50$\times$ (NA=0.55) objective lens. At the copper-donor interface, the beam waist of the femtosecond laser is measured as 1.6 μm, and the one of the QCW laser is measured as 9.7 μm. The power of both lasers is independently adjusted using the half-wave plate and polarizer combinations. The positioning of the two beams and the systematic inspection of the donor film is facilitated by a customized reflection microscopy arrangement which has been detailed in section 4.2.1 (not shown here). For experiments presented in this chapter, a 1000 nm copper film with 20 nm chromium interlayer (magnetron sputtering onto a 1-mm-thick glass substrate) is used as donor layer.

Time-resolved shadowgraphs of material ejections are recorded using a QIMAGING QICAM CCD camera mounted on a second customized microcopy arrangement based on a MITUTOYO M Plan Apo SL 50$\times$ (NA=0.4) super-long working distance microscope objective lens. Bright-field flash illumination is provided by a HIGH-SPEED PHOTO-SYSTEME KL-M NANO-LITE nanosecond flash lamp. The flash duration of 12 ns determines the temporal resolution of the acquisition system. As detailed in section 4.2.3 a digital delay generator (STANFORD RESEARCH SYSTEMS DG645) is used to precisely synchronize, with adjustable delay, the double-pulse process with time-resolved imaging. Meanwhile, the QCW pulse duration and the delay

T [K]	Thermal conductivity [i]	Heat capacity [ii]	Density [iii]	Viscosity[iv]	Surface tension[v]
293	400	382	8960	-	-
573	381	413	8809	-	-
973	354	446	8598	-	-
1400	167	516	7907	3.74	1280
1550	173	516	7796	3.00	1260
1700	177	516	7686	2.50	1240
1850	180	516	7576	2.14	1220

[i]K [$W\,m^{-1}K^{-1}$]   [ii]Cp [$J\,kg^{-1}K^{-1}$]   [iii]ρ [$kg\,m^{-3}$]   [iv]η [$mPa\,s$]   [v]γ [mN/m]

TABLE 6.1: Thermal and hydrodynamical parameters of copper. [110, 121, 122, 123]

between its rising edge and the femtosecond LIFT pulse can also be adjusted arbitrarily. Here, as illustrated in figure 6.1(b), the delay between the experimental initial moment (t = 0) and the arrival moment of the femtosecond laser pulse is noted as Δt, the femtosecond to flash delay is noted as τ.

6.2.2   QCW heating model

In DP-LIFT, the role of the irradiation of the first QCW pulse is to induce a local melting on the donor film. At fixed QCW power, when the femtosecond pulse irradiates the heated donor film with different delays Δt, the donor film exhibits different temperatures below or above melting. For copper, as shown in Table 6.1, the physical properties of the film are significantly temperature-dependent [110, 121, 122, 123]. Thus, it is worth to investigate the ejection dynamics of the liquid copper for different temperatures, controlled by varying the delay between the two laser pulses, since this hydrodynamic behavior depends on the fluid mechanics' characteristics of the film such as the dynamic viscosity and the surface tension. For the interpretation, the impact of the molten pool diameter should also be taken into account, as it will have an influence on the pressure distribution in the liquid film, which plays a key role in the ejection process. Accordingly, the space-time temperature evolution of the film induced by the QCW pulse irradiation should be first calculated.

As presented in section 3.3, the heating process in the donor layer induced by the QCW pulse is governed by the general heat equation:

$$\rho C_p \frac{\partial T}{\partial t} - \nabla(k\nabla T) = Q, \tag{6.1}$$

which gives the temperature T in the system in response to a heat source Q. For copper, the heat capacity C_p, density ρ and thermal conductivity k are temperature dependent [99, 100]. Thus, the heat equation which describes this process is not linear and it is numerically solved, as described in section 3.3. For the specific situation present in this chapter, the heat source Q is generated by the absorption of QCW laser, with a Gaussian profile along the

T [K]	Thermal conductivity [i]	Heat capacity [ii]	Density [iii]	Reflectivity[iv]
293	95	449	7119	0.65
573	82	526	7073	-
973	66	606	6983	-
1400	59	752	6895	-
1900	49	960	-	-
2130	40	1062	-	-
2400	33	756	6300	-

[i]$K\,[W\,m^{-1}K^{-1}]$ [ii]$Cp\,[J\,kg^{-1}K^{-1}]$ [iii]$\rho\,[kg\,m^{-3}]$ [iv]$R\,[1]$

TABLE 6.2: Thermal and optical parameters of chromium. [124, 125, 126]

x-direction, parallel to the film surface, according to the Beer-Lambert law, taking into account multiple internal reflections in the thin film,

$$Q = I_0(t)\alpha(1-R)exp(\frac{-2x^2}{\omega_0^2})\frac{exp(-\alpha z)}{1-exp(-\alpha D)},\qquad(6.2)$$

where R represents the reflection coefficient, α the linear absorption coefficient, D the thickness of the thin film, ω_0 the beam waist and z the absorption direction. For all the experiments presented in this article, the QCW laser and the sequence are driven by an electrical square pulse of 400 μs duration. Its raising edge defines the initial time (t = 0 μs). The optical output power of the QCW laser pulse would starts at t = 24 μs and is constant until it exponentially decays at t = 383 μs (see figure 6.1(b)), reaching zero at t = 400 μs. To fulfill the actual temporal evolution of the optical output, the QCW laser pulse intensity $I_0(t)$ is described by a piecewise function:

$$I_0(t) = \begin{cases} 0 & : & 0 \le t < 24\ \mu s \\ \frac{2E_p}{\pi\omega_0^2\tau_{qcw}} & : & 24 \le t < 383\ \mu s \\ \frac{2E_p}{\pi\omega_0^2\tau_{qcw}}exp(-\frac{(t-383)^2}{40}) & : & 383 \le t < 400\ \mu s \\ 0 & : & t \ge 400\ \mu s \end{cases},\qquad(6.3)$$

where E_p donated to the QCW pulse energy and measured as 770 μJ ($\pm$70 μJ), τ_{qcw} the pulse duration and measured as 376 μs (t =24 μs to t =400 μs).

6.3 Influence of donor temperatures

6.3.1 Temperature evolution

Using numerical simulations methods, the temperature evolution of the donor under QCW pulse irradiation is calculated from t=0 μs to t=500 μs and the result is shown in figure 6.2. More precisely, the evolution of the lateral temperature distribution in the QCW pulse irradiation affected region is mapped
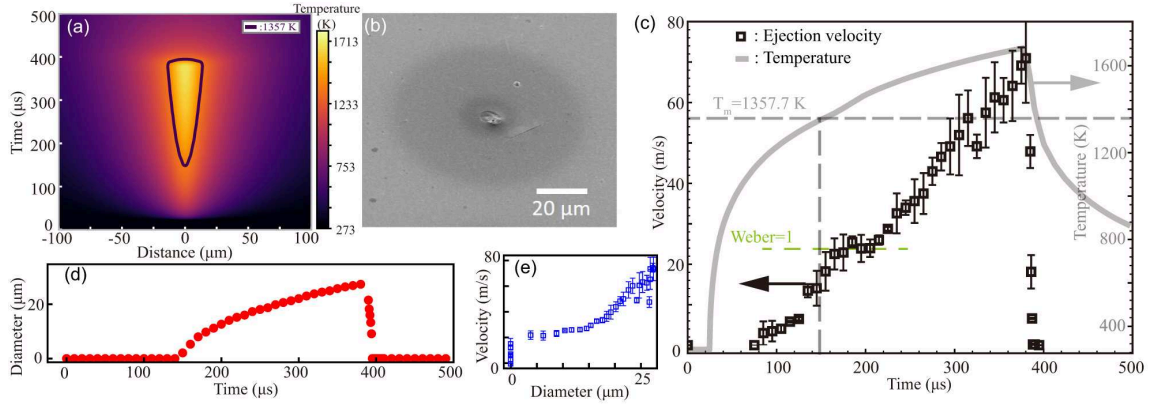
FIGURE 6.2: Space-time characteristics of the copper film and ejections during the DP-LIFT process. (a) Time-evolution of the lateral temperature distribution of the donor copper film under QCW pulse irradiation. (b) SEM image of the film after the DP-LIFT process. (c) Time-evolution of the temperature evolution in the central region of the QCW beam and the measured ejection velocities as a function of LIFT time (synchronization of the fs pulse). The melting temperature of copper under atmospheric pressure is 1357.7 K and shown by a horizontal dash line on the graph. (d) Time-evolution of the diameter of the molten film region. (e) Measured ejection velocities as a function of melting pool diameter.

as shown in Figure 6.2 (a). The donor film thickness is small enough (1-μm) to consider the temperature to be uniform in the z-direction (whole thickness). The solid line plot on this graph shows the contour line for the melted region (temperature above the fusion point). To have an overview of the heat affected area after DP-LIFT, an SEM image of the corresponding processed area on the donor film is presented in 6.2 (b). A light grey disk with diameter of ≈ 60 μm refers to the heat affected zone after the QCW laser irradiation and a dark grey disk with diameter ≈ 20 μm refers to the re-solidified material after melting. At the center of the molten pool, a vestige of surface pinching can be observed. This observation proves that a jet is initiated at the center of the QCW laser spot. As this central region also corresponds to the maximum temperature of the donor film, we plot its temporal evolution in 6.2 (c). Referring to the temporal profile of the QCW pulse described in Equation (6.3), the copper film temperature starts to rise at t=24 μs and the central region reaches the melting point at t=150 μs. From figure 6.2 (c), we can see that the temperature rises up to its highest value of 1689 K at t=383 μs before decrease sharply at t=395 μs leading to the re-solidification of the film. In 6.2 (d), the time-evolution of the molten pool diameter during this process is also presented, and one can observe that this parameter exhibits a similar evolution. The molten pool starts to form at t=150 μs and the maximum diameter 27.4 μm is reached at t=383 μs. After that, the molten pool diameter decreases sharply and at t=395 μs the molten pool has completely disappeared.

6.3.2   Ejections under different temperature

With the knowledge of the temperature of the copper donor film under the QCW pulse irradiation and the experimental observations of the ejection dynamics using the setup presented in figure 6.1, it becomes possible to investigate the impact of different molten pool temperatures and diameters on the ejection behaviors. We have performed DP-LIFT experiments for different QCW-to-fs pulse delays Δt (see figure 6.1(b)) without the presence of a receiver substrate. As shown in figure 6.3, the time-resolved observations of the ejection events are captured with LIFT-to-flash delays τ of 300 ns and 600 ns.

During the heating process, the femtosecond LIFT laser with the pulse energy of 2 μJ irradiates the middle of the heated zone with delay Δt with respect to the experimental initial moment (t=0). The LIFT-to-flash delay τ was first set at 300 ns in order to illuminate the ejection before any droplet develops. As shown in figure 6.3 (a), jetting seems to appear at $\Delta t = 125\mu$s. From $\Delta t = 175\mu$s to 380 μs the length of the jet increases, because of higher ejection velocities, and then diminished rapidly until no significant jetting is observed after $\Delta t = 388\mu$s. The second LIFT-to-flash delay τ was set at 600 ns in order to observe the ejection after the potential appearance of droplets. First, the shadowgraphy images acquired for this delay show that there is no evolution of the copper film motion between τ = 300 ns and τ = 600 ns for Δt delays shorter 155 μs or longer than 385 μs, which means that there is no ejection occurring for these conditions. Even if a jet seems to be initiated at $\Delta t = 155\mu$s and $\Delta t = 386\mu$s one should note that it cannot escape from the donor surface. From $\Delta t = 175\mu$s to 380 μs jets encounter different pinch-off processes and evolve into equilibrium spherical spheres, complex oscillators or the so-called endpinching depending on the initial aspect ratio of the jets. It is interesting to mention that these observations are consistent with the theoretical prediction of Notz et al [127], even though the jet radius is downscaled down to the micrometer scale in our experiments. To help in the interpretation of these mechanisms, the morphologies of the donor film surface after the DP-LIFT process are also presented in figure 6.3 (c) for each experimental condition. Based on the shadowgraphy images acquired at the two temporal delays, we have also calculated the average velocity of the ejection. This average velocity is plotted in the graph of figure 6.2(c) to highlight the correlation with the temperature evolution of the donor film.

According to these investigations, a first conclusion is that the impact of the copper film temperature on the process is not limited to a binary response associated with melted or unmelted films. This parameter plays a significant role in the dynamics of the laser-induced jetting process. When the donor film is melted, as the temperature increases, the initial ejection velocity increases. As both optical (reflectivity) and hydrodynamics (surface tension and viscosity) parameters are temperature related, we have tried first to correlate the temperature evolution to the ejection velocity changes using an energy balance model treatment (will be presented in section 6.4). However, the velocity variations that are predicted by this approach are not as large as those observed in our experiments and plotted in figure 6.2 (c). This is
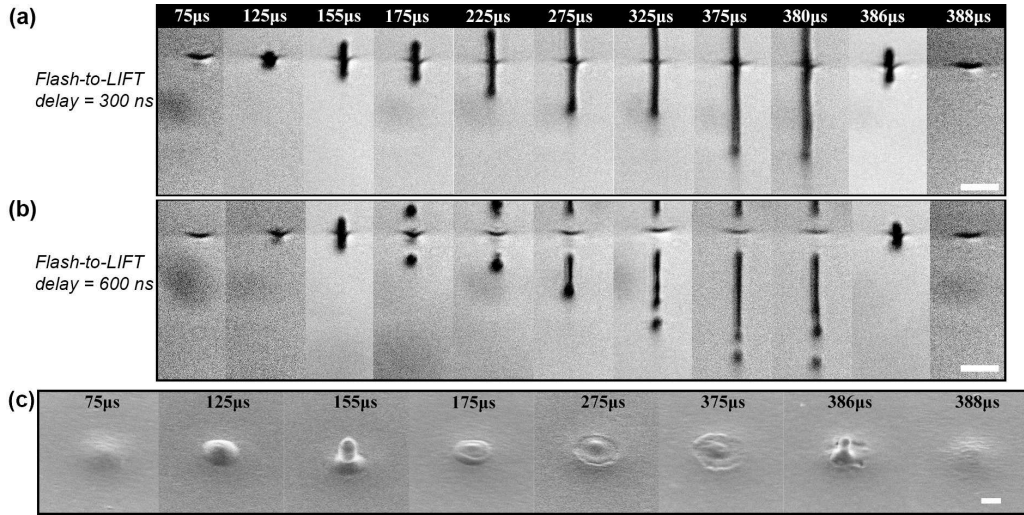
FIGURE 6.3: Shadowgraphy images of ejections at different LIFT moments during the QCW irradiation, with flash-to-LIFT delays of 300 ns (a) and 600 ns (b), scale bars: 10 μm. (c) SEM image of remaining structures on the donor film after the DP-LIFT process with different LIFT moments, scale bar: 2 μm.

most probably caused by the influence of the molten pool size ignored in our calculations. To establish the correlation between the molten pool diameter and the ejection velocity, we plot in 6.2 (e) the measured ejection velocities as a function of calculated molten pool diameters. From 15 μm to 25 μm the ejection velocities are linearly proportional to the molten pool diameters. This supports a first important conclusion on the importance of the molten pool diameter during the QCW pulse heating process. This is of significant technical importance as the temporal evolution of the molten pool diameter during the DP-LIFT process allows us to access in principle to a wide range of ejection regimes without changing neither the laser parameters (energy, fluence, pulse duration, etc.) nor the donor thickness.

6.3.3 Ejection regimes

Bump-like deformations

With the spatio-temporal evolution of the film temperature provided in figure 6.2, we determined that in DP-LIFT configuration with femtosecond LIFT pulse arriving with delay $\Delta t = 75\mu$s, the temperature of the donor film is high (> 1100 K at QCW spot center) but it still remains in its solid phase. Accordingly, as shown in figure 6.3 (c) (75 μs), there is no flow motion occurring at the free surface and finally, the femtosecond pulse locally induces an overpressure simply leading to a bump-like deformation of the donor film. At continuously increasing delays up to $\Delta t = 125\mu$s the temperature increases reaching about 1300 K near the melting point. For this condition, it can be seen in figure 6.3 that the femtosecond LIFT pulse produces a local expansion that can be observed at the early time ($\tau = 300$ ns) whereas this motion will be quickly stopped before τ=600 ns. This will finally lead to a bump-like

deformation with a higher aspect ratio on the donor film as shown in figure
6.3 (c) (125 μs).

Dynamics below ejection threshold

As the donor temperature continuously increases with delay, local melting
starts, and the liquid film motion induced by the femtosecond pulse irradia-
tion changes drastically. It can be observed that from Δt =125 μs to Δt =155 μs
the deformation velocity jumped from 7.4$\pm$ 0.5 m/s to 22.2$\pm$3.3 m/s. This is
due to the fact that the curve of the copper film temperature crosses the melt-
ing point (from 1303K to 1368K) and then the molten pool diameter jumps
from 0 to 3.8 μm. However, from figure 6.2 (c) and figure 6.3 (a-b) we can
see that, from Δt =155 μs to Δt =165 μs, the material does not escape from
the free surface. The SEM image shown in figure 6.3(c) (155 μs) also confirms
this behavior. In fact, this trapping can be explained by comparing the values
of the kinetic energy and the surface energy, as the ejection can only occur if
the kinetic energy of the ejected material exceeds its surface energy [45, 23].
Under those jetting regimes, the ejection kinetic energy is approximated as

$$E_{kin} = \frac{1}{2}\rho(T)d_l A_{ej} V_{ej}^2, \tag{6.4}$$

where $\rho(T)$ is the temperature dependent density, d_l is the liquid donor thick-
ness V_{ej} is the ejection velocity and A_{ej} is the surface area of ejection. And the
surface energy E_s is approximated as

$$E_s = \gamma(T)\Delta A, \tag{6.5}$$

where $\gamma(T)$ the temperature dependent surface tension of liquid copper and
ΔA the increase in surface area. By assuming that $A_{ej} = \Delta A$ and dividing the
kinetic energy E_{kin} by surface energy E_s yields

$$\frac{E_{kin}}{E_s} \approx \frac{\rho(T)d_l V_{ej}^2}{2\gamma(T)} = We_{ej}, \tag{6.6}$$

where We_{ej} is the Weber number. In the ejection threshold condition, using
$We_{ej} = 1$, the minimal escapable ejection velocity V_{ej_min} is determined by
equation 6.6. This minimal velocity is calculated at $V_{ej\_min} = 24\ m/s$ which
matches well with the value of the velocity (23.4 $\pm$2.3 m/s) measured at $\Delta t =$
175 μs and presented in figure 6.2(c).

Dynamics above escape threshold

From $\Delta t = 175$ μs to $\Delta t = 380$ μs the average ejection velocity increases from
23.4 $\pm$2.3 m/s to 74.5$\pm$3.4 m/s with a temperature increase from T = 1411 K
to 1689 K and a molten pool diameter increase from 8.8 μm to 27.4 μm. It is
worth to notice that, under those conditions, the average ejection velocity is
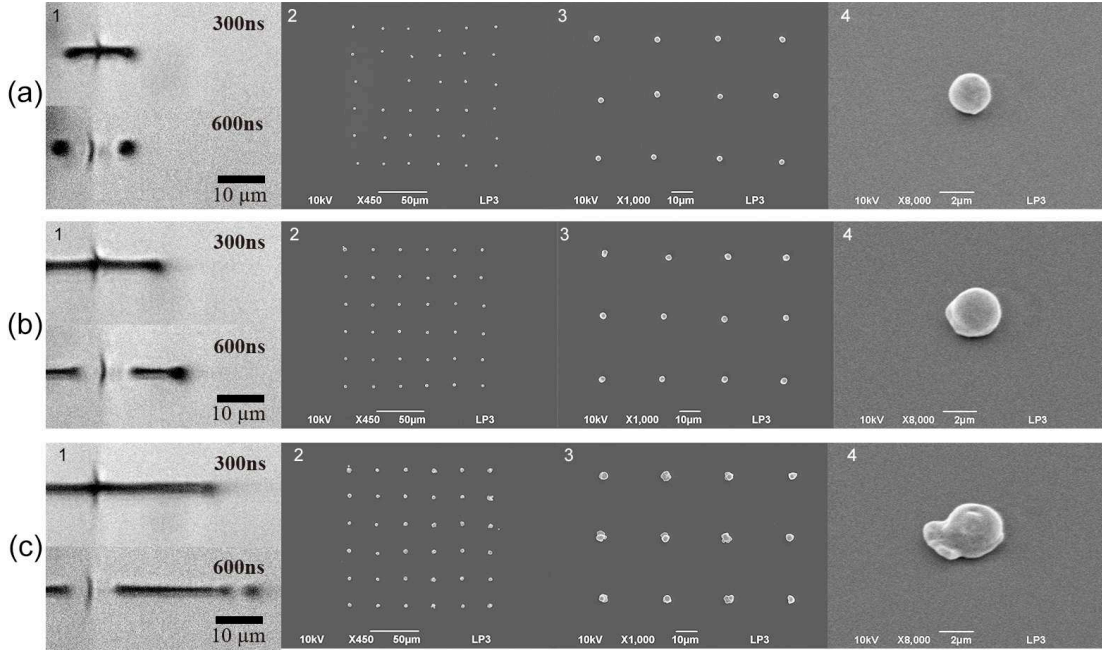proportional to the molten pool diameters. From SEM images presented in

FIGURE 6.4: Ejection induced by DP-LIFT process and the printed pixel matrixes with QCW-to-fs delays of 195 μs (a); 275 μs (b) and 375 μs (c).

figure 6.3 (c) one can also notice that there are no significant protrusion structures formed on the surface for these conditions, and only some ripples are observed. This is due to the higher temperature which leads to a longer time for the donor film to solidify. Shadowgraphy observations presented in figure 6.3 (b) show that the DP-LIFT generated jets pinch off at the surface for these conditions. Interestingly, these surface pinching and protrusion free features are different from most of the reported laser-induced nano-jetting phenomenon generated from ultra-thin metal films [116, 128, 49, 50, 51, 117, 118]. In those cases, the jetting mechanisms rely on the competition between inertia-capillary dynamics and crystallization, in which the jet elongates and breaks up into droplets due to the Plateau-Rayleigh instability and the formation of a neck occur in the solidification zone between the crystalline and liquid parts of the jet [83].

6.3.4 Printed copper microstructures

Droplet arrays printed under different QCW-to-fs delays

According to the previous discussions, the ejection behavior depends on the QCW-to-fs delay. A direct benefit from this finding is that it allows us to perform pixel-to-pixel printing with designed pixel shapes and sizes. By placing a silicon receiver substrate at 50 μm distance in front of the donor film, ejected materials can be readily collected. Then, by repeating the DP-LIFT process and controlling the motion of the receiver and donor substrates, 2D patterns with arbitrary design can be printed on the receiver. In this study, as a demonstration, we printed three 6×6 pixels matrices with a period of 30 μm for three different QCW-to-fs delays. As shown in figure 6.4(a1), for a

QCW-to-fs delay $\Delta t = 195$ μs, the ejection of the liquid copper have evolved into an equilibrium spherical sphere at $\tau = 600$ ns after a travel distance of ~ 8 μm. Thus, an average flying velocity of V_f = 13 m/s can be approximated. Under this condition, due to the low initial aspect ratio, the droplet will keep its spherical shape once the equilibrium is established. Due to the short transfer distance of 50 μm, the air drag effect can be neglected in these conditions which allow to assume that the impact velocity on the receiver is $V_{im} = V_f$. When the droplet reached to the receiver, its diameter d is ~ 2.5 μm and the impact Weber number We_{im} can be approximated as:

$$We_{im} = \frac{\rho d V_{im}^2}{\gamma} = 2.6 \tag{6.7}$$

Thus, as presented in figure 6.4(a4), when the droplet wets the receiver with such a small Weber number it can hardly spread and finally solidifies with a spherical sphere [111]. In figure 6.4(a2) and 6.4(a3), the repeatability is demonstrated by printing a matrix. The average diameter of the printed droplets is measured as 2.40 μm with a deviation of ± 0.23 μm.

For Δt = 275 μs, as shown in Figure 6.4(b1), the material is ejected as a jet which has traveled a distance of ~ 18 μm at $\tau = 600$ ns. When this ejection reaches the receiver the impact Weber number We_{im} is approximately 13.7, and under these conditions, as presented in figure 6.4(b4), the printed droplet starts to spread on the receiver. And compared to the previous case, it has a less smooth contour and exhibits discontinuities at the surface. This feature indicates that the pinch-off of the jet must have started before the material reaches the receiver, and the re-solidification stage suffers the merging of segmented droplets. In figure 6.4(b2) and 6.4(b3), a printed pixel matrix under these conditions is shown. The average diameter of the printed droplets is measured as 2.77 μm with a deviation of ± 0.12 μm that correspond to features larger than those of the previous case but with similar repeatability. For Δt = 375 μs, as shown in figure 6.4(c1), this long liquid jet starts to pinch-off followed by a so-called endpinching mechanism at $\tau = 600$ ns with a travel distance of ~ 36 μm. When the ejected material reaches the receiver the impact Weber number We_{im} is approximately 54.8. As presented in figure 6.4(c4), the corresponding printed droplet not only has a rough contour and discontinuities but it is somehow squeezed with a flatter shape. In figure 6.4(c2) and 6.4(c3), a printed pixel matrix is also shown, and the average diameter of the printed droplets in this condition is measured as 4.22 μm with a deviation of ± 0.48 μm.

High-aspect ratio copper microstructures

As presented in the last section, that is for the condition with Δt = 275 μs that the printed droplets have the smallest deviation. Thus, using this printing condition, we have demonstrated the ability to build microstructures in the third dimension by repeated debris-free droplet micro-printing with DP-LIFT technique at the same location. In figure 6.5(b), we show the structure obtained after printing four droplets while the receiver is kept at the same
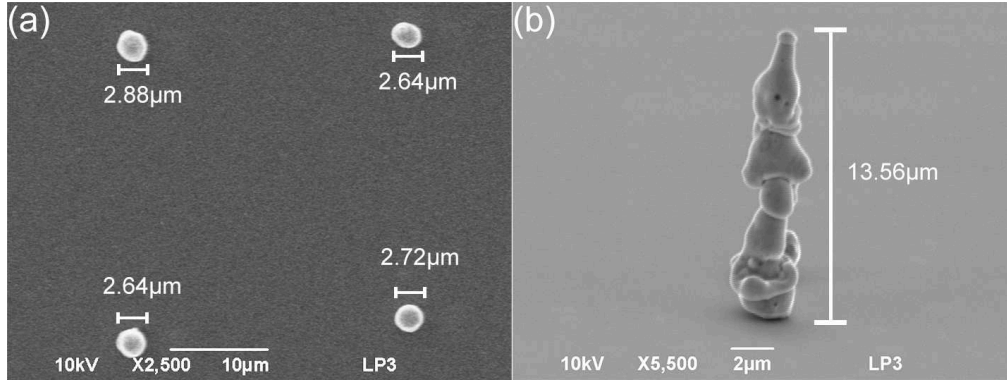
FIGURE 6.5: (a) Feature of four droplets in the array of printed pixels with an interval of 30 μm. (b) A micro-column stacked by four droplets.

location. The droplets are piled one by one on top of each other to finally form a micro-column with a height of $\sim 13.6\mu$m without any debris around the structure. This represents a critical step for technological considerations.

6.3.5 Summary

In this section, the space-time temperature evolution of the donor film induced by the quasi-continuous wave (QCW) laser used as a pre-pulse has been numerically investigated. By illuminating the heated film with identical femtosecond pulses at different delays, different ejection regimes have been observed. By correlating thermal simulations of the film temperature with time-resolved imaging of the laser-induced ejection we conclude that the main parameter governing the ejection dynamics is the size of the melted region rather than the copper film temperature. A technological benefit of these results is the possibility to achieve multi-scales printing without changing either the laser parameters (energy, fluence, pulse duration, etc.) or donor thickness. Droplet matrices with pixel diameters from 2.40±0.23 μm to 4.22±0.48 μm have been successfully printed as well as a micro-column with a height of 13.6 μm without any debris to show the potential of this DP-LIFT approach for the development of true-3D laser nano-printing technology. In the next section, the influence of the LIFT laser fluence on the jetting behaviors will be further studied.

6.4 Influence of LIFT laser fluence

In the previous section, we have determined the spatial and temporal evolution of the temperature of the donor film induced by the irradiation with the QCW laser pulse as well as the corresponding evolution of the molten pool diameter at the same time scale. Moreover, we showed that the jetting behaviors are strongly dependent on this pool diameter.

In this section, the femtosecond pulse is triggered at a fixed delay of $\Delta t = 275\ \mu$s, the molten pool diameter is $\sim 20\ \mu$m and the temperature at the center of the molten pool is 1590 K according to numerical calculation. Under these
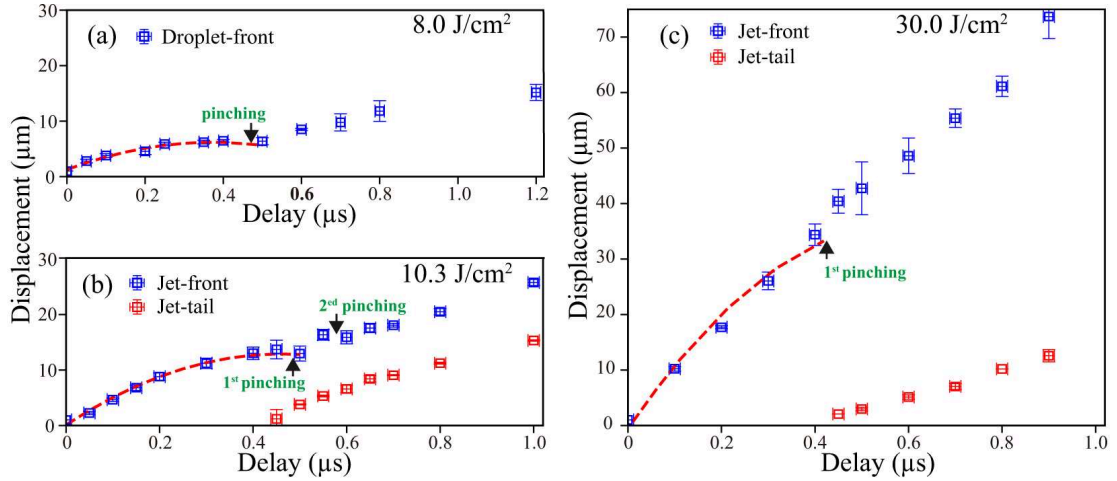
FIGURE 6.6: Displacement evolutions of ejection fronts as well as tails under different femtosecond laser fluence: (a) 8.0 Jcm^2; (b) 10.3 Jcm^2; (c) 30.0 Jcm^2.

conditions, liquid copper jetting behaviors induced by different femtosecond laser fluences are studied. Droplets matrix, as well as 2.5D pillars matrix, have printed on the receiver to confirm the reproducibility of the printing process.

6.4.1 Ejections under different LIFT laser fluences

According to the time-resolved shadowgraphy observations (not shown here, similar observations as those presented in figure 6.7), copper jetting starts by the formation of a conical liquid protrusion, as already observed in the case of micrometer thick liquid donor films. We first analyzed the impact of the femtosecond laser fluence on the initial ejection velocity of the protrusion. To determine this velocity, the displacements of the ejection fronts are plotted as a function of τ, and the slopes of the curves provide the ejection velocities at different ejection moments. As shown in figure 6.6(a), with the laser fluence of 8.0 J/cm^2, the increasing length of the ejection front displacements saturated at $\tau \sim 450$ ns meanwhile the ejection separates from the free surface and the initial ejection velocity of the protrusion at 100 ns is measured as 19.2$\pm$5 m/s. After this first pinching, the increasing of the ejection front trends to keep constant.

Under the fluence of 10.3 J/cm^2, as depicted by figure 6.6(b), the curve also exhibits a deceleration process of the ejected material until it escapes from the free surface at $\tau \sim 450$ ns. However, during the following step, the ejection exhibits a complex break-up process. Some fluctuations appear in the values of the displacement of the ejection front and tail from $\tau = 400$ ns to $\tau = 700$ ns, and those fluctuations are caused by the oscillation process which happens after the material flies out from the free surface and before its final breakup. After this period, the increasing of the displacements keeps as constant. The initial ejection velocity at $\tau = 100$ ns, is measured as 40.1$\pm$12 m/s. At last, for the fluence of 30.0 J/cm^2, as shown by figure 6.6(c), the ejection velocity at $\tau = 100$ ns is measured as 83.7$\pm$20 m/s. And the ejection also
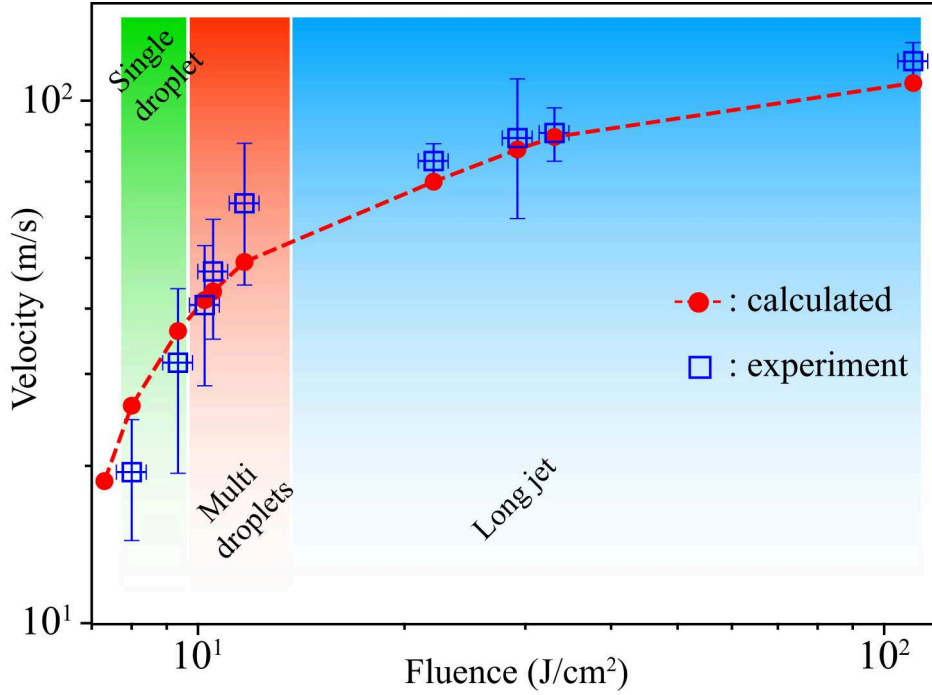
FIGURE 6.7: Ejection velocity variation against femtosecond laser fluence.

escaped from the free surface at $\tau \sim 450$ ns. The above three conditions show the trend of the response of the initial ejection velocity to the laser fluence. However, for further interpretation, the initial ejection velocities under a large range laser fluences are summarized in figure 6.7. From femtosecond laser fluence of 8.0 J/cm^2 to 110.0 J/cm^2, the ejection velocities V_{ej} at $\tau = 100$ ns varied from 19.2±5 m/s to 117.5±10 m/s. To understand this trend, an energy balance relation is considered. Conservation of the total energy (E_T) for the system of ejection can be written as:

$$\Delta E_T = \Delta E_k + \Delta E_s + \Delta E_d. \tag{6.8}$$

Since we have only varied the femtosecond pulse energy for each condition, any increase of the total energy ΔE_T is balanced by an increase of kinetic energy

$$\Delta E_k = \frac{1}{2}\rho d_l A_{ej} V_{ej}^2, \tag{6.9}$$

or of surface energy $\Delta E_s = \gamma \Delta A$, or convert heat through viscous dissipation ΔE_d. Here, ρ is the density, d_l is the liquid donor thickness, A_{ej} is the surface area of ejection and ΔA the increase in surface area. Under those jetting regimes, the initial energy of the ejection is assumed to be driven by the femtosecond pulse induced vapor. This vapor energy is estimated as the incident laser energy minus the energy required for heating the material to the boiling temperature. Therefore, the vapor energy can be determined as:

$$E_{vap} = E_{abs} - A_{femto}(d_v L_m + d_v C_p(T_v - T)) = \Delta E_T, \tag{6.10}$$

where E_{abs} is the femtosecond laser energy absorbed by the donor film, A_{femto}

is the femtosecond pulse irradiated surface area, T is the temperature of copper donor film at the LIFT moment, T_v is the boiling temperature of the donor, C_p is the heat capacity of copper and L_m is the evaporation enthalpy of copper. As pointed out by Brown et al [45], at the early times of ejections ($\tau \leq 300$ ns) very little kinetic energy is viscously dissipated. Thus, the viscous dissipation ΔE_d is neglected in the discussion presented here. And by combining equation 6.8 and 6.10, the ejection velocity is resulted as:

$$V_{ej} = \sqrt{\frac{2CA_{femto}[F_{abs} - \rho d_v L_m - \rho d_v C_p(T_v - T)] - \gamma \Delta A)}{\rho d_l A_{ej}}}, \qquad (6.11)$$

here we assume that $\Delta A = A_{ej}$, and a fitting factor $C = 0.06$ is used for the quantitative agreement. Similar fitting factor has also been reported by another group when investigating the vapor driven LIFT process [23]. From equation 6.11 the initial velocity of ejections can be predicted.

6.4.2   Jetting regimes

In figure 6.8, we present sequences of time-resolved images of the ejections under different fluences and with a frame-to-frame interval of 100 ns. First, at 7.3 J/cm^2 (first column), the initial ejection velocity is predicted as 9.4 m/s, thus the Weber number can be predicted as $We_{ej} = \frac{\rho d V_{ej}^2}{\gamma} \sim 0.5$. For such low Weber number, the kinetic energy of the initial protrusion is not high enough to overcome the pull-off force. That is experimentally confirmed by the observation of figure 6.8, where one can observe that ejections under this condition would not lead to the detachment from the liquid film and the protrusion is pull-back to the free surface within 700 ns. Here, we called this jetting regime as the trapped regime.

When the laser fluence increased to 9.4 J/cm^2, the kinetic energy is then high enough to overcome the pull-off force and finally, a pinch-off of the jet occurs at $\tau \sim 400$ ns. When this ejection escapes from the free surface, with an initial aspect ratio $L_0 \sim 4$, it rapidly evolves into a spherical sphere, which corresponds to the minimum internal energy. As the Ohnesorge number of those liquid copper jets can be characterized as:

$$Oh = \frac{\eta}{\sqrt{\rho \gamma l}} \sim 10^{-2}, \qquad (6.12)$$

where η is the liquid copper viscosity, ρ the density, γ the surface tension and l the jet diameter, this observation is in agreement with the theoretical predictions of Notz et al [127], in which the final shape of the filament is predicted as a function of L_0 and Oh. At a higher fluence of 18.7 J/cm^2, the pinch-off occurred at $\tau \sim 450$ ns and when the ejection escaped from the free surface it has a higher aspect ratio $L_0 \sim 10$. In this case, according to the prediction of Notz et al [127], the jet can no longer evolve into an equilibrium spherical sphere but exhibits a series of complex oscillations and ultimately breaks-up. The images of the figure 6.8 acquired with this fluence confirm
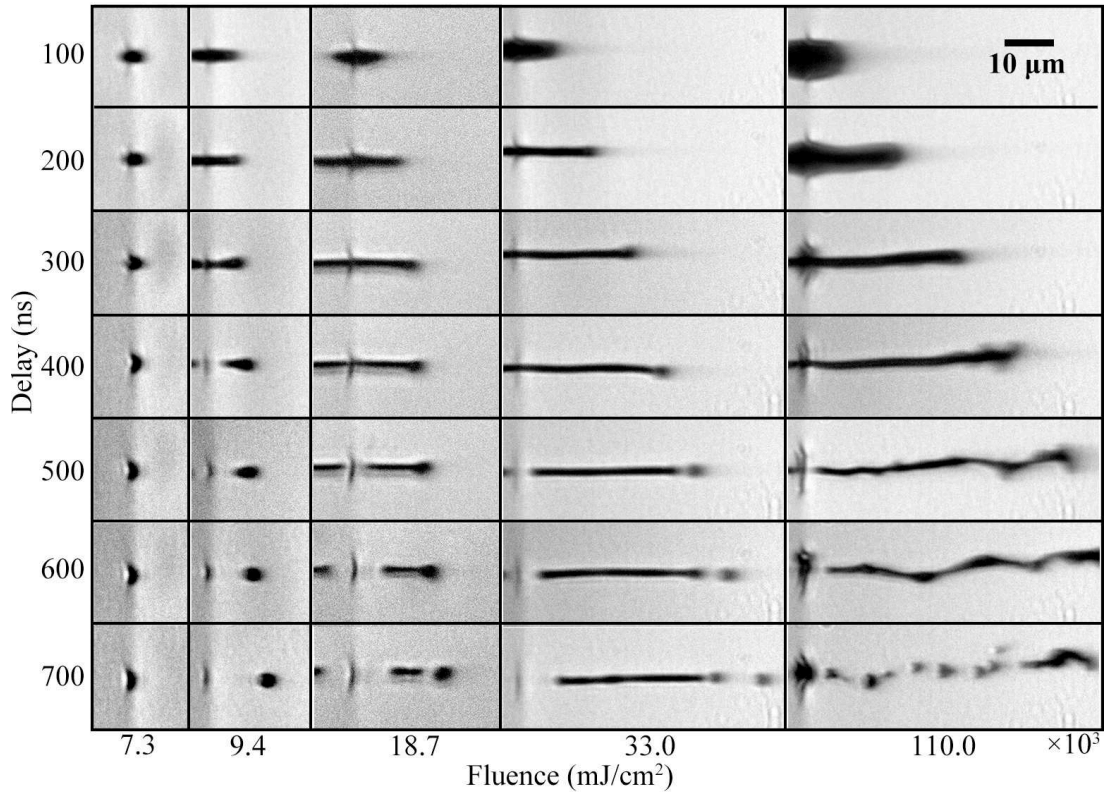
FIGURE 6.8: Time resolved shadowgraphic observation of ejections under different femtosecond laser fluences.

this theoretical prediction. At an even higher fluence 33.0 J/cm^2, the initial liquid protrusion has a higher aspect ratio. When the jet escaped from the free surface at $\tau \sim 450$ ns, the initial aspect ratio L_0 of the jet was ~ 19. And, as predicted, a so-called end-pinching mechanism occurs during the propagation leading to the pinch-off of daughter drops from its end. Finally, as the fluence increased to as high as 110.0 J/cm^2, a strong turbulent behavior is observed and the jet is no more stable as it propagates.

So, when the femtosecond laser fluence is varied different jetting regimes are observed, including trapped, single droplet, multi droplets, long jet and turbulent. The three middle regimes allow having a reliable control of the deposition process. Therefore we performed some printing in these conditions and the results are presented on figure 6.9. This approach should allow us to reach a significant range of deposit dimensions without changing the donor thickness. The following part investigates this feature.

6.4.3 Printed copper microstructures

By placing a silicon substrate at 50 μm in front of the donor film, ejected materials are collected. Then, 2D patterns with controlled pixel diameters have been realized by varying the femtosecond laser fluence.
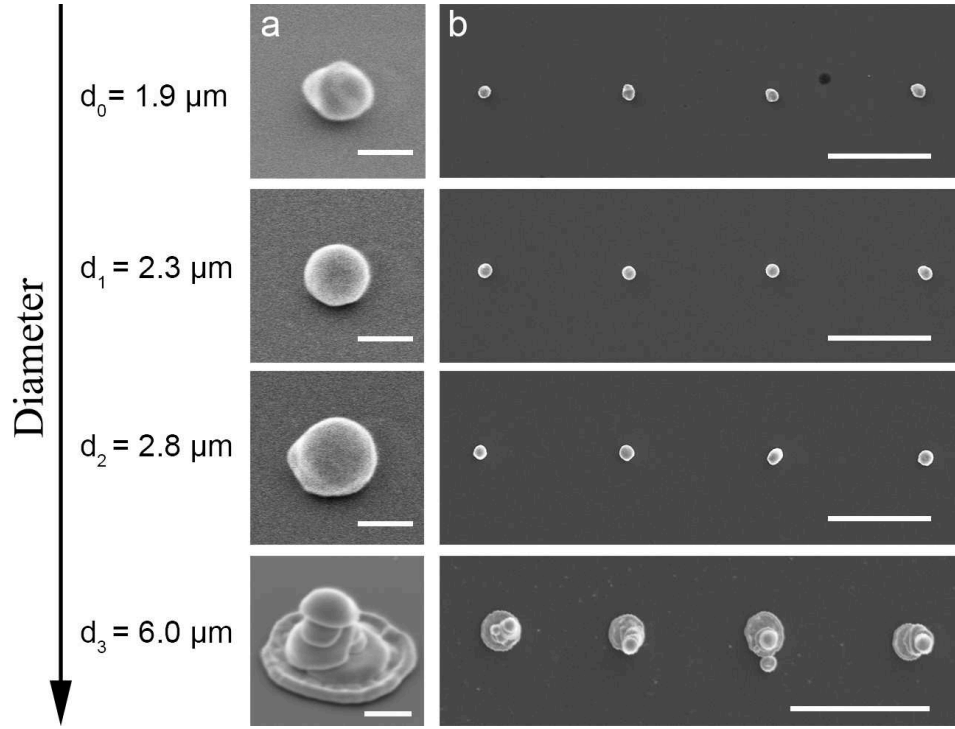
FIGURE 6.9: Laser pulse fluence dependence of the micro-deposit diameter. (a) SEM side views of droplets printed under different femtosecond laser fluences, scale bar: 2 μm. (b) SEM top views of droplets array, scale bar: 20 μm. Each line, the applied laser fluences are kept the same.

Droplets array printed with under different fluence:

First, we investigated the morphologies of deposits collected under the jetting regime of "single droplet". As shown in the first line of figure 6.9, for laser fluence of 8.2 J/cm^2, after one DP-LIFT process a single droplet with a diameter of 1.9 μm can be collected onto the receiver. a small increase of the fluence up to 8.8 J/cm^2 lead to the transfer of single droplet with a bigger diameter of 2.3 μm. The collected deposits under those laser fluence show features of continuous surface and spherical shape, which is consistent with the jetting features presented in our previous observations. With laser fluence of 11.7 J/cm^2, the jetting occurs in the "multi droplets" regime. As shown in the third line of figure 6.9, the deposit exhibits discontinuities at the surface. This indicates that before the ejected material reaches the receiver, the jet has broken-up during the transfer, and the re-solidification stage suffers from the merging of those segmented droplets at the receiver surface. By further increasing the laser fluence to 29.3 J/cm^2, the jetting is performed in the "long jet" regime. As shown in the last line of figure 6.9(a), the material in contact with the receiver surface a deposit is widely spread as a disk. Upon this disk, droplets piled onto each other. In fact, this is evidence which indicate that during transfer the jet start to pinch-off into daughter drops from its end. And when they reached to the receiver, the main jet first arrived on the receiver and widely spread into a disk shape due to the high impact velocity and later those daughter drops pinched from the tail of the main jet arrived
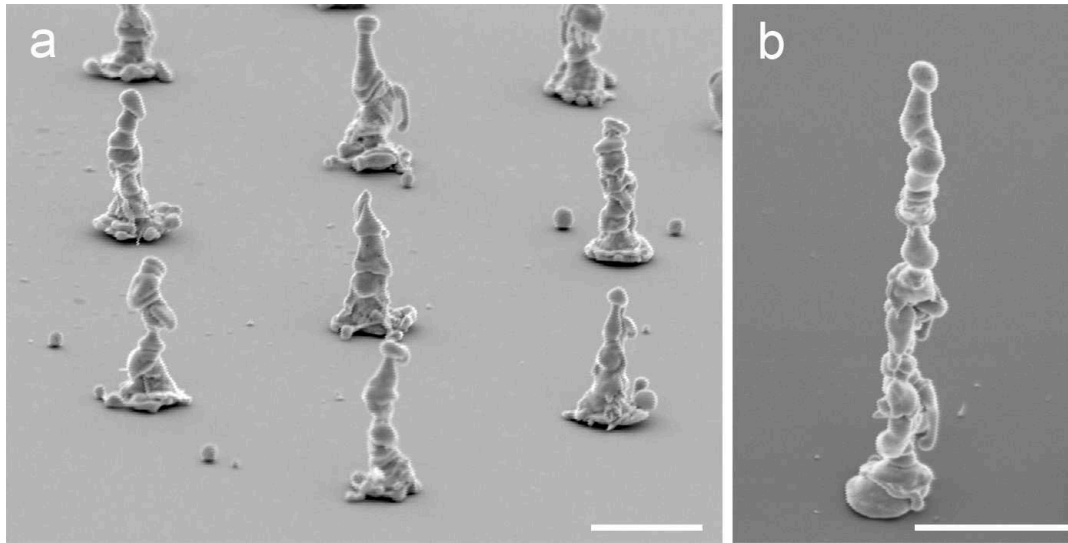
FIGURE 6.10: 2.5 D microstructures printed by DP-LIFT process. (a) SEM image of a micro-column array, each column is stacked by three deposits, scale bar: 10 μm. (b) A micro-column with an aspect ratio of 19 stacked by nine deposits, scale bar: 10 μm.

and piled on top of this disk. Those postmortem SEM analyses confirm the feature of each jetting regimes which have been investigated by the previous time-resolved shadowgraphy studies.

2.5 D pillars matrix:

Furthermore, we demonstrated the ability to print high aspect ratio structures. In order to get a stable structure, a relatively large base is desired and we chose a femtosecond laser fluence of 29.3 J/cm^2 to benefit from the feature of "long jet"jetting. The array of pillars printed in these conditions is shown in figure 6.10(a). In this printed micro-column array, each column is stacked by three deposits, and it worth to notice that, even both three deposits are initiated by the same laser conditions, the later deposits suffer a faster quenching process due to the higher thermal conductivity of copper compared to silicon. Therefore, when the first ejection reaches the silicon surface, due to the low thermal conductivity of silicon, liquid copper has enough time to spread out before getting solidified. However, when the laser deposits stacked onto the first one with a copper-to-copper contact, they quickly got solidified and stop their spreading. Finally, with nine stacked deposits, a micro-column with an aspect ratio of 19 has been achieved by carefully maintaining the donor-to-receiver gap size.

6.4.4 Summary

In this section, an energy balance model is used to predict the influence of femtosecond laser fluence on the initial jetting velocity of liquid copper. Time-resolved shadowgraph observations confirmed the prediction of the

model and allow us to classify different jetting regimes for guiding multi-scales printing. By only varying the femtosecond laser fluence, droplet matrix with pixel diameters from 1.9 μm to 6.0 μm have been successfully printed. Micro-columns matrix, as well as a micro-column with an aspect ratio of 19, are printed to show the potential of this approach for the development of true-3D laser multi-scale nanoimprinting technology.

6.5   Conclusions

In chapter 5, DP-LIFT technique has been first demonstrated and as well as its strong potential as a flexible additive microfabrication process. However, the development of this promising approach requires a complete understanding of the DP-LIFT process. Compare to the single pulse situation, double-pulse process introduces further complexity not only in terms of the additional pulse but also in terms of the relations between the effects induced by the two pulses. To address this problem, we systematically investigated the double-pulse process in this chapter. It has been discovered that the QCW pulse induced heating will not only quantitatively changed the ejection due to the phase change mechanism but also qualitatively influence the jetting velocity by controlling the melting pool diameter. Meanwhile, the influence of the LIFT laser fluence on the liquid copper jetting velocity is predicted by an energy balance model. By the awareness of the impact of the different irradiation parameters of double-pulse process on the ejection dynamics, printings with controllable shapes and diameters are achieved. In this chapter, by setting a receiver at 50 μm away from the donor film and by simply varying the double-pulse irradiation parameters, droplets matrix with printed pixel diameters from 1.9 μm to 6.0 μm have been printed. 2.5 D pillar matrix has also been printed to demonstrate the potential in 3D microstructures printing.

Chapter **7**

Digital nanoprinting

This chapter will discuss the results obtained in experiments targeting the generation of jets of nanometer dimension from micrometer-thick copper films. The corresponding printed nanodot arrays will be presented.

Contents

7.1   Introduction to nano-jetting

The understanding of fluid mechanics phenomena at the nanoscale is actually an extremely challenging statistical physics problem [112]. Any solution to address this problem is of major interest not only for the fundamental understanding of Nature at a small scale but also because of its great potential for engineering and technological innovations. Theoretical investigations have been carried out for decades [129, 130] thanks to atomistic and molecular dynamics simulations. In the last decade, the development of new micromachining techniques like soft lithography and bottom-up assembly methods has made the study of nanofluidics much more accessible through experiments [131]. Indeed, nanofluidics systems lead to revolutionary applications in important fields such as bio-engineering and lab-on-chip applications. However, it provides also the possibility to investigate experimentally the fundamental aspects of fluid behaviors at the nanoscale when specifically designed systems are fabricated.

All these experimental developments are essentially nanochannel-based fluidics and one can note that controllable channel-free nanofluidics phenomena have been very rarely reported. It is only recently that nano-jetting phenomena have been experimentally observed with the development of laser-induced forward transfer (LIFT) [51, 13]. In these experiments nano-jetting is initiated by femtosecond laser irradiation from a ≈50 nm thin gold or silicon film and in the following years, this discovery has been discussed by comparison with theoretical investigations and molecular dynamics simulations [83, 119, 120]. In practice, the femtosecond pulse irradiates the thin film with a Gaussian beam profile which induces a Gaussian pressure force distribution and the local melting of the film. Then, the Gaussian pressure distribution leads to the detachment of the melted film from the substrate with the shape of a dome shell. Within the dome shell, the normal component of the capillary force decelerates the normal velocity of the shell and the parallel component leads to the displacement of the shell material towards the center. The jet starts to form when the reverse motion of the shell begins [83]. In this process, the nanoscale dimension of the jet is mainly provided by the thickness of a few tens of nanometers of the thin films that are used. The collected material takes the form of nanoparticles with diameters that are about 3-10 times larger than the thickness of the donor film.

In chapter 5 and chapter 6 the double-pulse LIFT (DP-LIFT) approach has shown its potential for generating stable jet from any type of donor films regardless of their thickness or composition. As we have shown in previous chapters, the general idea behind DP-LIFT is to use a first quasi-continuous (QCW) pulse to generate a liquid film and then use a second ultrashort pulse to initiate the ejection process. Using this technique, we have reported that jets with diameters of $\sim$2 μm can be generated from a film with a thickness of 1 μm.

In this chapter, we report on the channel-free nano-jetting phenomena occurring in the DP-LIFT technique applied to a micrometers thick copper film. To study the nano-jetting dynamics, time-resolved shadowgraphy imaging is
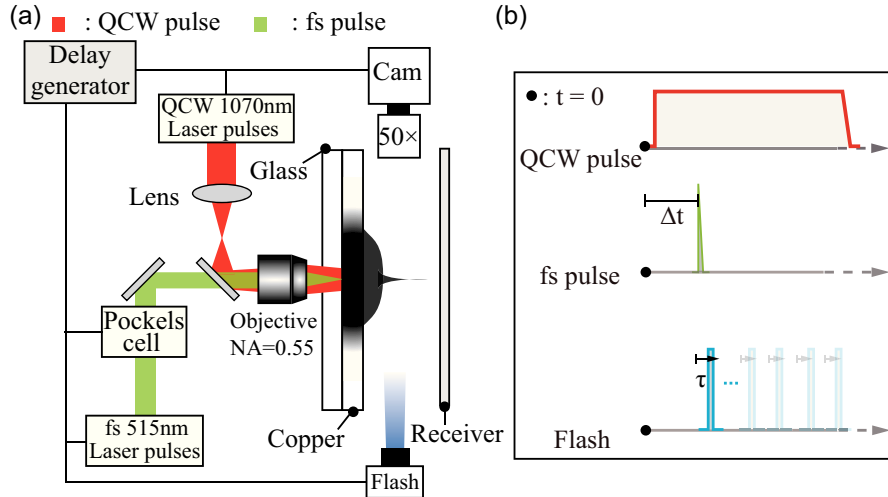
FIGURE 7.1: (a) Sketch of the experimental setup for DP-LIFT. The femtosecond LIFT laser beam is represented in green and the QCW laser beam for pre-melting of the film is represented in red. Illumination flashlight is shown by the blue color. A plano-convex lens is used to enter the focusing objective with a diverging QCW laser beam. (b) A time chart of events for synchronization of the DP-LIFT and time-resolved observations.

used to capture the flying materials. Afterward, the jet diameter information is deduced by measuring the diameters of the printed droplets. To the best of my knowledge, this is the first demonstration of controllable LIFT printing of droplets with a diameter smaller than the donor thickness. Finally, we will show that the driving mechanisms responsible for this reduced-scale jetting behavior are probably closely linked to the diameter of the melting pool induced by the QCW pulse.

7.2   Experimental setup

The details of the DP-LIFT experimental arrangement has been described in section 4.2.1. In this chapter, the experimental arrangement is depicted in figure 7.1. The laser source used to achieve the melting of the donor film is the quasi-continuous wave (QCW) laser (IPG PHOTONICS YLR-150/1500-QCW-AC-Y14) emitting, at 1070-nm wavelength, pulses of variable duration from 50 μs to the continuous wave operation. In order to achieve a relatively larger melting pool, a plano-convex lens with 300 mm focus length can be used to prefocus the QCW laser beam. Followed by this first QCW laser irradiation, a AMPLITUDE SYSTEMES S-Pulse HP femtosecond (fs) LIFT laser delivers, at a 515 nm wavelength (second harmonic), pulses of 500 fs duration (FWHM) that are focused at the center of the melted region to induce the material ejections. To do so, the diverged QCW laser beam and the collimated fs laser beams enter coaxially through a long working distance MITUTOYO M Plan Apo 50× (NA=0.55) objective lens. The beam waist at the copper-donor interface with the femtosecond laser is measured as 1.6 μm.

And at this interface QCW beam diameter is measured as 62 μm (with prefocusing) and 9.8 μm (without prefocusing). For experiments presented in this chapter, similar to chapter 6, a 1000 nm copper film with 20 nm chromium interlayer (magnetron sputtering onto a 1-mm-thick glass substrate) is used as donor layer. The time-resolved shadowgraphy imaging setup is also kept as described in chapter 6.

7.3 Results

In order to determine the working windows for nano-jetting, parametric studies were first performed by varying the fluences of both lasers. Under some specific DP-LIFT configurations, nano-jetting phenomena are rapidly observed and the jetting behaviors are investigated by time-resolved shadowgraphy. Then, the characteristics of the metal film before the ejection are modified by varying the LIFT to QCW delay and the ejection dynamics is studied for different melting pool diameters. To demonstrate the reproducibility and the potential of this approach for nanofabrication applications, droplets matrix has been printed on a receiver substrate set ~50 μm in front of the donor.

7.3.1 Parameters studies

In previous chapters, jetting behaviors generated by DP-LIFT have been systematically studied. By taking advantage from the stable jetting process using a 1 μm copper film as the donor, arrays of single droplets with diameters varying from 1.9 μm to 6.0 μm have been successfully printed onto a receiver placed 50 μm away. In this section, in order to explore the printing limits, we have carried out parametric studies in which the energy of the QCW and fs pulses are varied. Depending on the beam shaping of the QCW pulse, managed by the use or not of a prefocusing lens, experimental series are classified as "Large QCW spot size" and "Small QCW spot size".

Large QCW laser spot size

In chapter 6, the laser spot diameters of the QCW and short pulse laser used in the sequences are measured at 9.8 μm and 1.6 μm respectively. Here, we show the results obtained for a larger melting pool. As shown in figure 7.1, a plano-convex lens with 300 mm focus length was used to produce a divergent QCW laser beam before the focusing optics. In this configuration, at the carrier-donor interface, the QCW laser spot diameter is measured at 63.0 μm. The duration of QCW pulses are set as 400 μs, and for DP-LIFT process the delay with the femtosecond pulse is set at 275 μs.

Figure 7.2 shows the results of a parametric study where the fluences of both lasers are varied. To analyze the influence of the QCW laser fluence at a given femtosecond laser fluence, we can look at the images vertically. The first column corresponds to the situation where the femtosecond pulse is not triggered and then only the QCW pulse irradiated the donor film. Figure

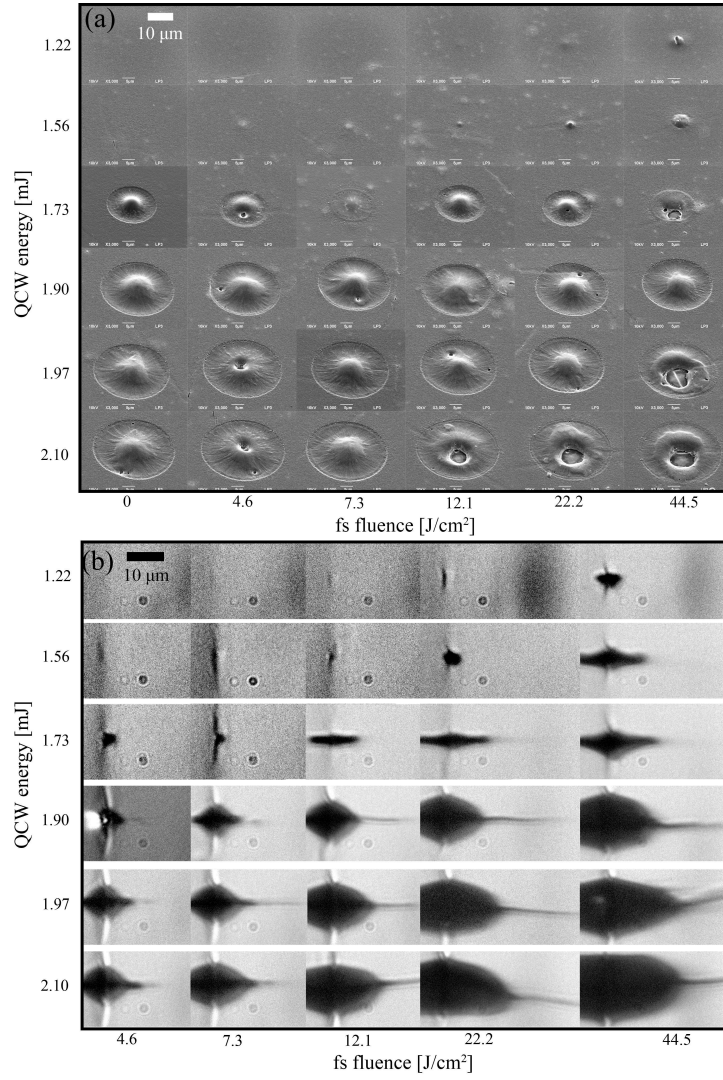**FIGURE 7.2:** Results of DP-LIFT experiments with different combinations of QCW pulse energies and femtosecond laser fluences when the QCW laser spot diameter is set at 63.0 μm. (a) SEM images of remaining structures on the donor film after each DP-LIFT sequence. (b) Shadowgraphy images of ejections induced by each DP-LIFT configurations, captured for a delay of 150 ns after the femtosecond laser pulse irradiation.

7.2(a) shows the SEM images of this donor film observed after the irradiation. When the QCW pulse energy is low, no visible deformation is induced at the free surface. As the QCW pulse energy increases to 1.73 mJ, a circular surface deformation with a diameter of $\approx 21\ \mu$m appears at the center of the irradiated zone. In this melted volume, the liquid copper moves towards the central region and forms a bump when it solidifies. The surface is then convex in the center and concaves between the bump and the outer part of the melted area. The lateral dimensions of the deformation increase with the QCW pulse energy. By analyzing Figure 7.2 horizontally, one can study the influence of the ultrashort pulse laser fluence. For QCW pulse energy of 1.22 mJ, at low fs laser fluence, there is no visible bump appearing on the free surface. However, when the fs laser fluence reaches 22.2 J/cm^2, that is the fs laser irradiation that initiates the formation of small surface deformation. For QCW pulse energy of 1.56 mJ, this transition shift towards lower fs laser fluences and a detectable bump appear for a fluence as low as 4.6 J/cm^2. When the QCW energy is above 1.73 mJ, the copper film is melted over its full thickness and the topography of the free surface deformation controlled by the QCW laser irradiation. For instance, at a QCW pulse energy of 1.90 mJ, even though the fs laser fluence varies from 0 to 44.5 J/cm^2, the morphology of the remaining structures on the donor film after DP-LIFT remains almost identical. However, for high QCW energy such as 2.10 mJ, one can observe that the central bump starts to break (sometimes off to the center) for fs laser fluences above 12.1 J/cm^2. This could be induced by the ablation of the glass substrate.

For each SEM image presented in figure 7.2 (a), a corresponding shadowgraphy image is shown in figure 7.2 (b). Each image was captured for a delay of 150 ns after the irradiation by the femtosecond laser. One can notice that for the sites corresponding to the case where the central bumps were broken (refer to the sites shown at the bottom right corner of figure 7.2 (a) and (b)), the shadowgraphy images reveal tilted unstable ejections. When the QCW pulse energy is low ($<$ 1.73 mJ), ejections are visualized only when applying high fs laser fluence (for instance: 44.5 J/cm^2). In those cases, the visualized ejections exhibit features which are similar to the DP-LIFT induced jetting reported in chapter 6 and the jet diameter is $\approx 2\ \mu$m. When the QCW laser pulse energy of 1.90 mJ is used to pre-heat the copper film, the typical surface deformation, previously described, is observed whatever the fs laser fluence, and it is striking to note that in these conditions, shadowgraphy images point out the formation of a focused nanojet initiated by the fs laser irradiation. The diameter of this jet is below the diffraction limit of our observation system, which is of the order few hundreds of nanometers. As the fs laser fluence increases, the length of the focused jet increases. Behind this first nanojet, one can note that a 'normal' liquid copper jet (similar to those reported in chapter 6) also formed with a lower jetting velocity. In comparison with figure 7.2 (a), one can see that this focused nano-jetting phenomenon always appears for cases where the QCW pulse can induce a surface deformation by itself. Also, a window for stable transfer with such focused jetting can be found at the bottom left corner of figure 7.2 (a). From

this observation, one question arises: 'What is the key features that lead to the generation of such focused jetting behavior?'. The response is obviously of major importance for the development of high-resolution printing technology. Even if the surface topographies observed after the copper solidification are different than those formed when the fs laser irradiated the surface, one can suppose that there is a link between the topography of the donor free surface when the femtosecond pulse hits the sample and the formation of these nanojets. To investigate this hypothesis, a similar parametric study has been performed with a more focused QCW laser beam.

Small QCW laser spot size

In these experiments, the QCW laser spot diameter is reduced down to 9.8 μm at the carrier-donor interface by simply removing the plano-convex lens on the beam path before the focusing optics. In chapter 5, the importance of the lateral temperature distribution has been discussed. It has been shown that: to initiate a stable liquid jet from the free surface of the donor film, the donor has to be melted through its whole thickness meanwhile a proper pressure gradient should be produced. In this section, to find the driving mechanisms of focused nano-jetting, we want first to verify the influence of the lateral temperature distribution and the pressure gradient on this phenomenon. For a direct and fair comparison with the situations reported in chapter 6, the laser spot diameters of the double-pulse sequence are set as 1.6 μm and 9.8 μm for the femtosecond laser and QCW laser respectively. The duration of QCW pulses is set as 400 μs and the delay of the femtosecond pulse is set at 275 μs for the DP-LIFT process.

Figure 7.3 shows the results obtained under such DP-LIFT configuration. As previously, the first column of figure 7.3(a) gives the SEM images of the surface topography of the donor film after the irradiation with the QCW pulse only. When the QCW laser pulse energy is low, no deformation can be induced on the free surface, and as the QCW pulse energy increases to 0.88 mJ, it generates a bump with a diameter of ≈ 4 μm. The main difference with the deformations shown in figure 7.2 is the "purely" convex shape of the bump formed at the free surface. It can be seen that under this condition, the melted copper expands vertically to the free surface. However, due to the constrained lateral dimensions, the centripetal movement in the melting pool is less important and the liquid copper cannot accumulate significantly at the center. Despite this limitation, we still note that the dimension of the bump increases with the QCW pulse energy but when the energy is increased to 1.26 mJ, the bump starts to break from its center area. By applying the femtosecond laser pulses, ejections can be initiated as shown by the corresponding shadowgraphy images presented in figure 7.3 (b) which have been captured with a delay of 150 ns after the fs laser pulse irradiation. Comparing all results together, one observes that, for a QCW pulse energy of 0.77 mJ, there is no visible bump at the free surface for low fs laser fluence, but a significant tip starts to form for fs laser fluence above 22.2 J/cm^2. That is confirmed by the corresponding shadowgraphy images. For a QCW pulse of 0.88 mJ, stable ejections are established for fluences higher than 22.2 J/cm^2,

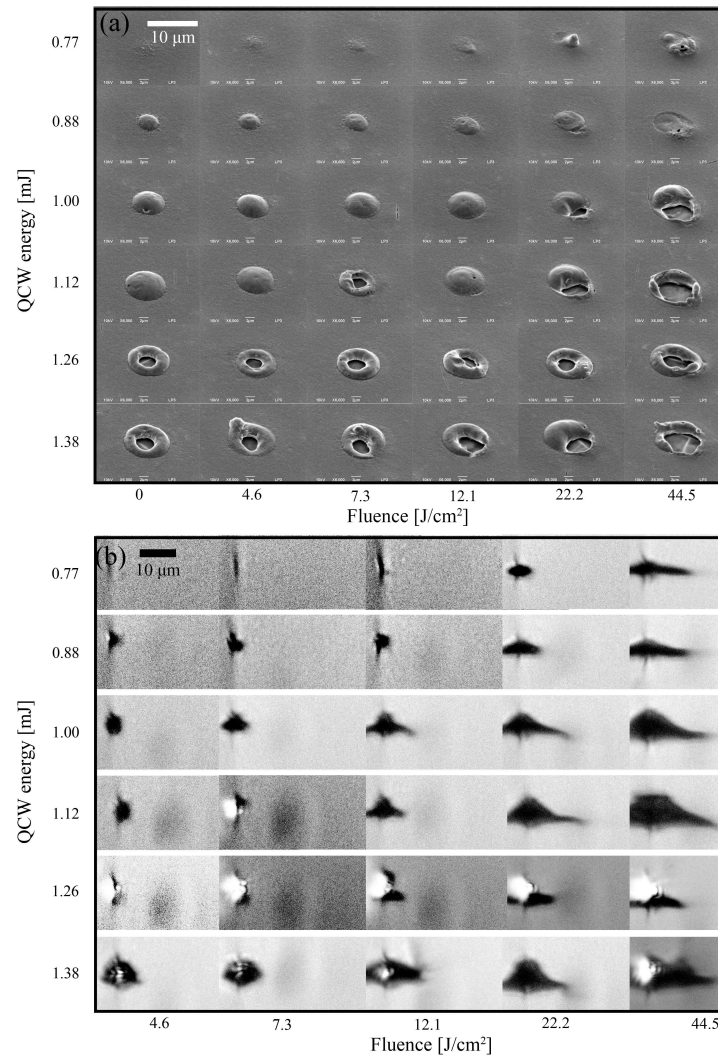**FIGURE 7.3:** Results of DP-LIFT experiments with different combinations of QCW pulse energies and femtosecond laser fluences when the QCW laser spot diameter is set at 9.8 μm. (a) SEM images of remaining structures on the donor film after each DP-LIFT sequence. (b) Shadowgraphy images of ejections induced by each DP-LIFT configurations, captured for a delay of 150 ns after the femtosecond laser pulse irradiation.
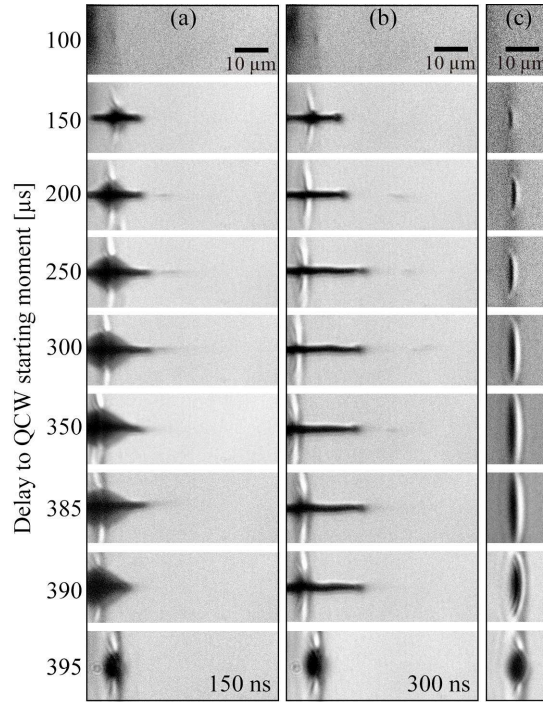
FIGURE 7.4: Shadowgraphy images of ejections captured with for different delays. For (a) and (b) The QCW laser spot diameter and the pulse energy are set at 63.0 μm and 1.90 mJ. The fs laser fluence is set at 5.4 J/cm^2 and observation are done at delays of 150 ns (a) and 300 ns (b). For comparison, (c) give shadowgraphy images of induced surface deformations by the QCW laser only. (delay of 150 ns)

as observed with shadowgraphy images, even for larger delays (not shown). For the highest fs laser fluence, 44.5 J/cm^2, the SEM image shows that the copper surface solidifies with a slightly concave shape and this is due to a large amount of liquid copper eject at this fluence compared to the melting pool volume achieved with low QCW laser energy. When the QCW laser energy is higher than 1.00 mJ, ejections occur at even lower fs laser fluences, and for the QCW energy of 1.38 mJ, the ejections start to become unstable as can be seen with the shadowgraphy images.

Under this DP-LIFT configuration, more parametric studies have been performed (not presented here). However, none of our observations shows evidence of focused nanojet generation. These negative results force us to conclude that the generation of the focused nanojet is somehow linked to the characters of the molten pool. At this stage, we anticipate the probably important role of either the pool diameter or the melting pool topography, two factors which are in our case closely connected.

7.3.2 Jetting under different melting pool diameters

In order to investigate how the melting pool diameter influences the jetting behavior, the first challenge is to estimate the pool diameter in the experiments. To do so, a time-resolved shadowgraphy study of the surface deformations induced by a single QCW laser pulse is performed. QCW laser

pulses with a duration of 376 μs (set at 400 μs with the control unit), energy of 1.90 mJ and spot diameter of 63 μm were applied in these investigations. As shown in figure 7.4 (c), significant shades start to appear with 150 μs delay with respect to the QCW pulse rising time. Those shades are most probably due to the inflation of the liquid copper layer. Also, it should be noticed that this inflated area may have a size smaller than the melting pool. As the QCW pulse continuously heat the copper film, the dimension of the inflated area extents, and correspondingly the dimension of the melting pool should also extend. By firing fs laser pulses with a fluence of 5.4 J/cm^2 at different moments, jetting under different surface deformation conditions and molten pool diameters are presented in figure 7.4 (a) and (b). At delay of 100 μs, the copper film has not reached the melting point and no ejection is observed. At delay of 150 μs, as the copper film starts to melt and to generate a slightly inflated area (a similar dimension to the one reported in chapter 6), the fs pulse irradiation generates an ejection. This ejection exhibits the same features as our previous reported liquid copper jets in DP-LIFT process. At 150 ns after the ejection, the parallel component of the capillary force leads to the displacement of the shell material toward the center and consequently a protrusion with a triangle base is formed on the free surface. At 300 ns after the fs irradiation, the protrusion is further elongated and the centripetal movement of the shell material leads to the thinning of the jet waist. However, under this DP-LIFT conditions, there is no evidence supporting the hypothesis of focused nanojet formation in these images.

After 200 μs of heating with the QCW laser pulse, the inflation is further enlarged whereas the curvature of the expanded surface is only modestly larger in comparison with the situation after 150 μs. Under this DP-LIFT configuration, at 150 ns after the ejection, a protrusion with a triangle base can also be visualized on the free surface. However, in front of this protrusion, the focused nanojet is observed. At 300 ns after the ejection, similar to the previous discussion, the protrusion is further prolongated and the centripetal movement of the shell material leads the thinning of the jet waist. The focused nanojet is then further elongated during flying, and the average flying velocity is ≈ 80 m/s.

After 250 μs and 300 μs of heating, the size of the melting pool continuously increases. Under those DP-LIFT configurations, it is striking to see that focused nanojets are always generated. However, after ≈ 350 μs, even the size of the melting pool continuously increases, the generation of focused nanojets becomes progressively more difficult to establish. After $385-\mu$s heating, the melting pool reaches its largest dimensions, however, no focused nanojet are observed under this condition (see figure 7.4).

During the falling time of the QCW pulse intensity, at 390 μs, it is shown in figure 7.4 (c-390) that the melting pool starts to shrink. Under this condition, the melting pool exhibits a larger surface curvature and, as shown in figure 7.4 (a-390) and (b-390), the process of 'normal' surface jetting occurs without any observable generation of focused nanojets. At 395 μs, the melting pool is further shrunk and starts to get resolidified. Accordingly, at larger times the shadowgraphy images of the surface deformations always keep the

same feature than the one shown in figure 7.4 (c-395).

7.3.3 Nano-jetting under different femtosecond laser fluences

According to the previous investigations, it is known that in the DP-LIFT process, a focused nanojet can be generated from an inflated melting pool with a diameter from $\approx$10 μm to $\approx$20 μm. This illustrates the importance of the QCW laser pre-heating. However, the influence of the femtosecond laser fluence on the focused nano-jetting behaviors is still unknown at this stage of the study. In this section, QCW laser pulses with a duration of 376 μs and pulse energy of 1.9 mJ are used to heat up the donor film. Femtosecond pulses with fluences varying from 2.6 J/cm^2 to 22.5 J/cm^2 irradiates the center of the melting pool after $275 - \mu$s heating with the QCW laser pulse (during the pulse) in order to initiate jetting events.

As presented in the first row of figure 7.5, when the fs laser fluence is as low as 2.6 J/cm^2, at a 100 ns delay after femtosecond pulse irradiation, the liquid copper forms a triangle dome and tends to leave the free surface. However, due to the low kinetic energy of the liquid copper, the material cannot escape the free surface. After $\sim$300 μs, we observed that the liquid dome has returned back to the donor.

By increasing the fs laser fluence up to 3.8 J/cm^2, at 100 ns after femtosecond pulse irradiation, we observe that the focused nanojet starts to form from the melting pool. Following the nanojet, the movement of the liquid shell is controlled by the balance between the pressure force and the capillary force. At 200 ns, the nanojet starts to disconnect from the liquid shell and evolves into a single droplet perpendicularly flying away from the free surface with an average velocity of 46 m/s. Meanwhile, one note that the kinetic energy of the moving liquid shell cannot overcome the surface energy at this fluence, which finally prevents its escape. Therefore and interestingly, only a droplet with diffraction limited dimension is transferred under this DP-LIFT conditions. When the fs fluence is increased to 4.8 J/cm^2, at 100 ns, a longer focused nanojet forms. It is also disconnected to the liquid shell at $\approx$200 ns and flies away from the free surface with an average velocity of 69 m/s as a single sub-micron droplet. Under this fs laser fluence, the liquid shell will finally evolve into an equilibrium spherical shape. As the fs laser fluence is increased up to 7.6 J/cm^2 the focused nanojet still disconnects to the liquid shell at $\approx$200 ns, but during propagation, starts (at $\approx$300 ns) to break-up into two droplets. Meanwhile, the liquid shell transforms into a jet with a higher initial aspect ratio to finally break into two spherical particles. Finally, at the highest laser fluence of 22.5 J/cm^2, the focused jet can be elongated up to $\approx$ 20 μm. The liquid shell also develops into a long jet, starting to encounter end-pinching as it expands.

7.3.4 Droplet arrays

The previous investigations are of interest not only because a novel nano-jetting phenomenon has been highlighted, but also because some working
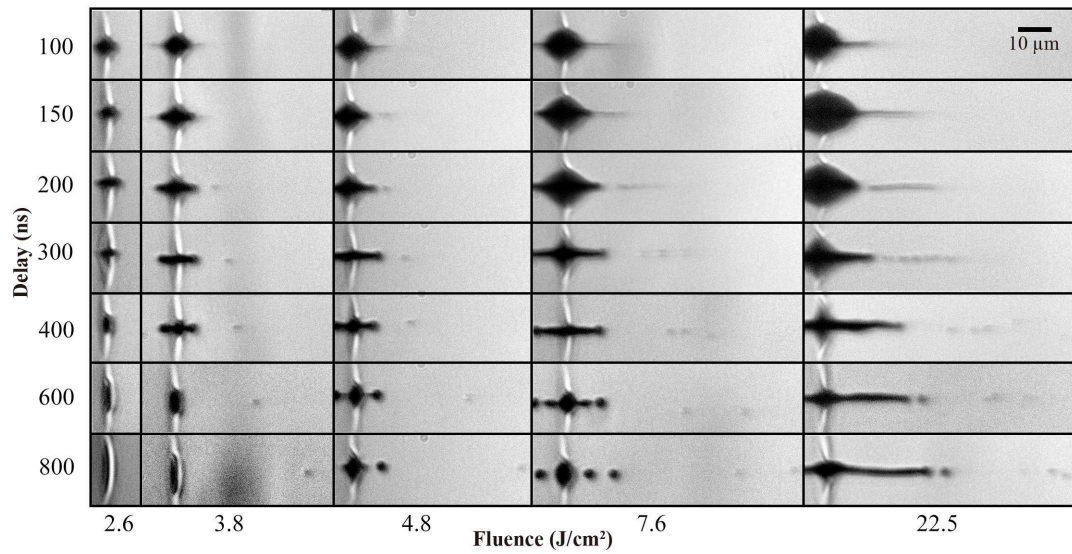
FIGURE 7.5: Time-resolved shadowgraphic observation of ejections under different femtosecond laser fluences. In all cases, the femtosecond laser pulse irradiates the center of the melting pool after $275 - \mu$s heating with the QCW laser pulse.
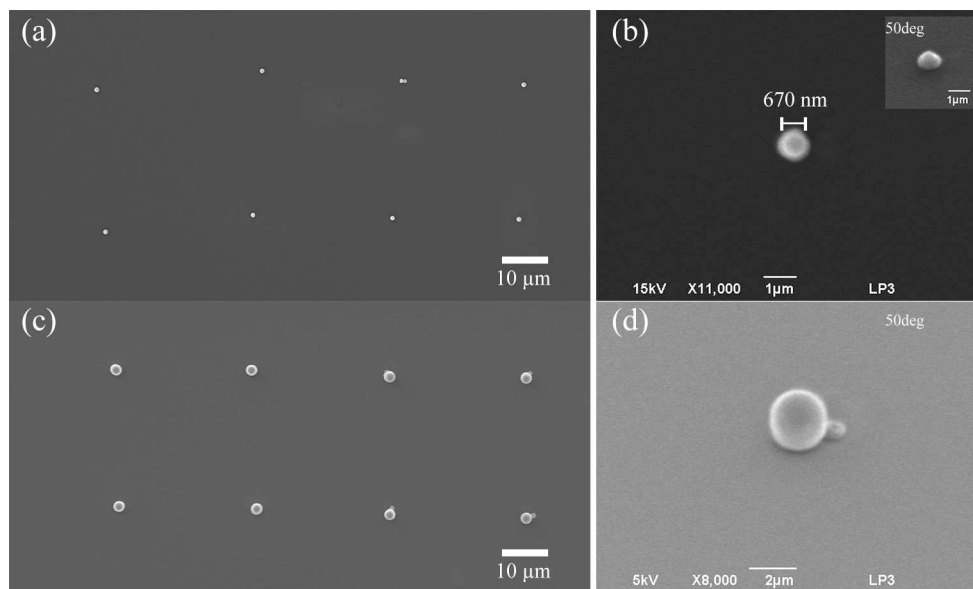
FIGURE 7.6: (a) Nanodroplet array and (b) image of a single nanodroplet printed with the fs laser fluence of 3.8 J/cm^2. (c) Nanodroplet array and (d) image of a single pixel which includes a single nanodroplet and a micro-sphere printed with the fs laser fluence of 4.8 J/cm^2.

windows for single nanodroplet transfer have been found. This leads us to propose a new engineering practice for additive nano-printing. In this section, by placing a silicon substrate at 50 μm in front of the copper donor film successful transfer of the nanodroplets are reported. A direct consequence is that desired patterns can then be printed by appropriate motion control of the receiver. As shown in figure 7.6 (a), by applying the same DP-LIFT conditions than those presented in figure 7.5 (3.8 J/cm^2) a nanodroplet array was successfully printed. From the image of a single pixel shown in figure 7.6 (b), one can see that the printed nanodroplets have a diameter of $\approx$ 670 nm. This directly suggests that the corresponding focused nanojet diameter (while not measurable) should be smaller than this dimension.

By applying the DP-LIFT conditions presented in figure 7.5 (4.8 J/cm^2), as shown in figure 7.6 (c), an array with pixels of micrometer dimension was successfully printed. As previously described, under this condition an equilibrium spherical particle will also be ejected from the free surface. Accordingly, it is finally also collected by the receiver. From the image of a single pixel shown in figure 7.6 (d), one can see that it is actually composed of a nanodroplet and a micro-sphere next to each other in perfect agreement with the flying materials observed by shadowgraphy under these conditions. It is worth to note that, in figure 7.6 (c) the top view of some pixel shows only one sphere which is most probably due to the overlap between the first printed nanodroplet and the following printed micro-sphere.

7.4   Discussions and conclusions

In this chapter, we have reported on a focused nanojetting phenomena. To investigate the driving mechanism of such focused nanojets, parametric studies have been carried out. With copper donor films of 1 μm thickness, it has been found that the focused jetting behavior can only be generated from an inflated melting pool with diameters from $\approx$ 10 μm to $\approx$ 20 μm. By varying the femtosecond laser fluence from 2.6 J/cm^2 to 22.5 J/cm^2, working windows for single nanodroplet transfer, single nanodroplet -plus- single micro-droplet transfer and other combinations have been determined by time-resolved shadowgraphy. Based on these first investigations, it is not possible to provide a definitive explanation of the origin of this nanojet formation. When the 1 μm thick copper film is irradiated in appropriate conditions, two similar jetting dynamics are induced: one at the microscale and one at the nanoscale. The fluid motions have the same behavior but the amount of fluid is much smaller for the nanojet. This means that the forces that induce this fluid motion are different. It is known that the microjet is generated by the reverse movement of the liquid dome shell formed by a pushing force induced by local vaporization with the ultrashort laser pulse, and the relation between the jet velocity and the pulse fluence is correlated by an energy balance that can be modeled (section 6.4). However, the origin of the focused nanojet is still unclear. With this study, we revealed that focused jetting is very sensitive to the inflated melting pool diameter and it generates earlier than the formation of the liquid dome shell. Accordingly, one

reasonable hypothesis of its origin can be related to the surface singularities leading the collapsing depression of standing waves [132]. Flow focusing has already been reported when fluid motion is generated by laser irradiation [133, 134, 135]. However, this phenomena has always been reported for concave free surface. This makes sense because when a plane wave approaches a concave surface, an overpressure is generated at the center of the curved surface, which is closer to the plane wave. However, the curvature of the QCW leaser heated surface is most probably convex, and then the flow focusing effect should not be observed. On the other hand, that is, to the best of my knowledge, the first time a so small fs laser spot (1.6 μm) is used in combination with a 1 μm thick donor film. In such a situation, the shock wave generated by the fs laser irradiation cannot be considered anymore as a plane wave but as a spherical wave. Then, if the surface curvature is not too strong, as for large QCW spot instead of small one, for instance, the flow focusing could be induced by curved shock wave approaching an almost flat surface. This hypothesis clearly needs to be confirmed.

For technological considerations, the focused nanojet response associated with large working distance (50 μm) open a direct way toward a new practical solution for additive nanoprinting. Combining these results with those of the previous chapter (chapter 6), we have shown that it is possible to print debris-free droplets with diameter from 670 nm to 6.0 μm from a copper film with a thickness of 1 μm by simply adjusting the irradiation parameters in double-pulse sequences. The high reproducibility reported for the printed structures shows the potential of the DP-LIFT technique to bridge the gap between "nano-manufacturing" and "micro-manufacturing" without any change on the experimental arrangement. Finally, the potential versatility of this laser technique holds promises to bring more nano-sciences concepts into practice.

Chapter **8**

Conclusions

In this chapter, based on the research objectives, conclusions are addressed. Outlooks about the future works are also provided.

Contents

8.1   Conclusions

- Objective 1: Investigate the driving mechanisms of single pulse LIFT.

In order to investigate the driving mechanisms of single pulse LIFT, we first used a picosecond laser with pulse duration of 50 ps. In this regime, the relation between the donor film thicknesses and the ejection behaviors have been determined. Varying the donor thickness d from 180 nm to 620 nm, ejection behaviors under different laser fluences have been studied by time-resolved shadowgraphy imaging and analyzed by two-temperature modeling (TTM). It is shown that, for donor film thinner than 410 nm, a careful choice of the laser fluence allows the selection of the ejection regime among "cap", "jet-like" and "spray" mode. However, as the film thickness increased, the regimes of "cap" and "jet-like" ejection start to shrink and the printed pixel is accompanied with a large amount of debris. The analysis performed thanks to the two-temperature model shows that the laser-induced ejection in the liquid phase from a solid thin film requires a sufficient temperature gradient along the film thickness. The melting temperature needs to be reached at the free surface and the vaporization temperature must be reached at the interface between the donor film and the glass substrate. A too thin film doesn't allow to achieve a temperature gradient high enough. The laser energy required to melt the film over its full thickness is too high and that leads to the vaporization of a strong volume of the donor film at its interface with the substrate and the generation of a large amount of debris.

- Objective 2: Develop a new LIFT process by using a double pulse.

In order to achieve stable and debris-free transfers over a large process windows the new DP-LIFT process has been developed. In this thesis, we proposed to use first a QCW pulse to melt the donor film, and then an ultrashort pulse to initiate the ejection. Based on this prototype DP-LIFT induced ejection has been systematically compared to the ejections induced by single pulse LIFT. We demonstrated that DP-LIFT widely enlarges the working windows of the jet regime. Long and stable liquid metal jets have been observed for a wide range of irradiation conditions, the formation and expansion of liquid metal jets from solid metal films has been investigated by the time-resolved imaging technique. Successful jet transfers of different donor films such as Au, Cu, Ag, and Ni-Cu point out the universality of this new double pulse laser printing technique.

- Objective 3: Investigate the driving mechanism of DP-LIFT.

The strong potential of DP-LIFT being demonstrated, we investigated its driving mechanisms. It has been shown that the effects of QCW pulse irradiation are not limited to a binary effect related to the local phase change of the metal film, but the increase of the energy deposited in the metal layer also induces an increase of the jetting velocity. It appears that this effect is not related to the temperature dependence of the metal film, but most probably to the variation of the melting pool diameter by lateral thermal diffusion.

- Objective 4: Explore the ejection dynamics of DP-LIFT and find the critical parameters for controlling the printing results.

An energy balance model is used to predict the influences of ultrashort laser fluence on the initial jetting velocity. These numerical results are in good agreement with the experimental measurements performed by time-resolved shadowgraph. Based on these results, different jetting regimes of DP-LIFT have been classified and that also provide some guidelines to achieve multi-scales printing. Indeed, by varying only the parameters of the two lasers and their synchronization, a matrix of the pixel with diameters varying from 1.9 μm to 6.0 μm have been printed from a 1 μm thick copper donor film. Moreover, the matrix of vertical pillars have also been printed and that demonstrates the potential of 3D micro-structures printing.

- Objective 5: Explore the way to deliver nanometer scale jets from a thick donor film through DP-LIFT

When a 1 μm copper film is irradiated by a 63 μm QCW laser spot, melting pools with diameters ranging from $\sim$10 μm to $\sim$20 μm are generated and their free surfaces exhibit a concave shape. In these conditions, focused nanojets have been generated by a focused ultrashort pulse. The process windows, in terms of ultrashort laser fluence, to transfer nanodroplets has been determined, and arrays of nanodroplets with a diameter of $\sim$670 nm has been printed.

Thanks to the DP-LIFT technique, the working distance of stable transfer can be extended up to $\sim$ 100 μm. Moreover, from a donor film with a given thickness, the debris-free single droplet with diameters from 670 nm to 6.0 μm can be successfully printed with high reproducibility. Those results prove the high potential of the DP-LIFT technique, and successfully bridge the "nano-manufacturing" and the "macro-manufacturing". This development should help to bring more nano-science concepts into practice.

8.2 Outlooks

The further developments of DP-LIFT rely on knowledge improvements in both engineering and physics. The investigations should be focused on the following two points.

- The first one is to further investigate the physics of the focused nanojet, as the driving mechanisms are still unclear.

- The second one would be to upgrade the controlling units of the prototype (beams and motions) in order to further improve the precision of the energy deposition and the printing resolution.

Bibliography

[1] L. J. Guo. "Nanoimprint Lithography: Methods and Material Requirements". In: *Advanced Materials* 19.4 (Feb. 2007), pp. 495–513.

[2] Thomas Bottein et al. "Environment-controlled sol-gel soft-NIL processing for optimized titania, alumina, silica and yttria-zirconia imprinting at sub-micron dimensions". In: *Nanoscale* 10.3 (Jan. 2018), pp. 1420–1431.

[3] Sami Alom Ruiz and Christopher S. Chen. "Microcontact printing: A tool to pattern". In: *Soft Matter* 3.2 (Jan. 2007), pp. 168–177.

[4] Huacun Wang et al. "Nanoscale Printing Technique and its Applications in Nanophotonics". In: *Nano* 11.09 (Sept. 2016), p. 1630002.

[5] Yueh Lin Loo et al. "Interfacial chemistries for nanoscale transfer printing". In: *Journal of the American Chemical Society* 124.26 (2002), pp. 7654–7655.

[6] J. Rühe. "And There Was Light: Prospects for the Creation of Micro- and Nanostructures through Maskless Photolithography". In: *ACS Nano* 11.9 (2017), pp. 8537–8541.

[7] C. Vieu et al. "Electron beam lithography - Resolution limits and applications". In: *Applied Surface Science* 164 (2000), pp. 111–117.

[8] M. Feinaeugle et al. "Time-resolved shadowgraph imaging of femtosecond laser-induced forward transfer of solid materials". In: *Applied Surface Science* 258.22 (2012), pp. 8475–8483.

[9] Alberto Piqué. "Digital Microfabrication by Laser Decal Transfer". In: *Journal of Laser Micro/Nanoengineering* 3.3 (2008), pp. 163–169.

[10] M. Duocastella et al. "Time-resolved imaging of the laser forward transfer of liquids". In: *Journal of Applied Physics* 106.8 (Oct. 2009), p. 084907.

[11] J. Bohandy, B. F. Kim, and F. J. Adrian. "Metal deposition from a supported metal film using an excimer laser". In: *Journal of Applied Physics* 60.4 (1986), pp. 1538–1539.

[12] David P. Banks et al. "Nanodroplets deposited in microarrays by femtosecond Ti:sapphire laser-induced forward transfer". In: *Applied Physics Letters* 89.19 (2006), pp. 87–90.

[13] Urs Zywietz et al. "Generation and patterning of Si nanoparticles by femtosecond laser pulses". In: *Applied Physics A: Materials Science and Processing* 114.1 (Jan. 2014), pp. 45–50.

[14] Ludovic Rapp et al. "Pulsed-laser printing of organic thin-film transistors". In: *Applied Physics Letters* 95.17 (Oct. 2009), pp. 1–4.

[15] M. Makrygianni et al. "Laser printing and characterization of semiconducting polymers for organic electronics". In: *Applied Physics A: Materials Science and Processing* 110.3 (Mar. 2013), pp. 559–563.

[16] Romain Fardel et al. "Fabrication of organic light-emitting diode pixels by laser-assisted forward transfer". In: *Applied Physics Letters* 91.6 (Aug. 2007), p. 061103.

[17] Nicholas T. Kattamis et al. "Ambient laser direct-write printing of a patterned organo-metallic electroluminescent device". In: *Organic Electronics: physics, materials, applications* 12.7 (2011), pp. 1152–1158.

[18] F. Di Pietrantonio et al. "Volatile toxic compound detection by surface acoustic wave sensor array coated with chemoselective polymers deposited by laser induced forward transfer: Application to sarin". In: *Sensors and Actuators, B: Chemical* 174 (2012), pp. 158–167.

[19] Christos Boutopoulos et al. "Direct laser immobilization of photosynthetic material on screen printed electrodes for amperometric biosensor". In: *Applied Physics Letters* 98.9 (Feb. 2011), p. 093703.

[20] Andrew J. Birnbaum et al. "Laser printing of multi-layered polymer/metal heterostructures for electronic and MEMS devices". In: *Applied Physics A: Materials Science and Processing* 99.4 (June 2010), pp. 711–716.

[21] Lothar Koch et al. "Skin tissue generation by laser cell printing". In: *Biotechnology and Bioengineering* 109.7 (July 2012), pp. 1855–1863.

[22] Sylvain Catros et al. "Laser-assisted bioprinting for creating on-demand patterns of human osteoprogenitor cells and nano-hydroxyapatite." In: *Biofabrication* 3.2 (June 2011), p. 025001.

[23] Ralph Pohl et al. "Ejection regimes in picosecond laser-induced forward transfer of metals". In: *Physical Review Applied* 3.2 (2015), pp. 1–9.

[24] M Zenou, A Sa'ar, and Z Kotler. "Laser jetting of femto-liter metal droplets for high resolution 3D printed structures." In: *Scientific reports* 5.February 2016 (2015), p. 17265.

[25] Claas Willem Visser et al. "Toward 3D Printing of Pure Metals by Laser-Induced Forward Transfer". In: *Advanced Materials* 27.27 (July 2015), pp. 4087–4092.

[26] Romain Fardel et al. "Shadowgraphy investigation of laser-induced forward transfer: Front side and back side ablation of the triazene polymer sacrificial layer". In: *Applied Surface Science* 255.10 (Mar. 2009), pp. 5430–5434.

[27]   Romain Fardel et al. "Laser-Induced Forward Transfer of Organic LED Building Blocks Studied by Time-Resolved Shadowgraphy". In: *The Journal of Physical Chemistry C* 114.12 (Apr. 2010), pp. 5617–5636.

[28]   D M Karnakis et al. *Laser induced molecular transfer using ablation of a triazeno-polymer*. Tech. rep. 1998, pp. 781–786.

[29]   Ludovic Rapp et al. "Laser printing of a semiconducting oligomer as active layer in organic thin film transistors: Impact of a protecting triazene layer". In: *Thin Solid Films* 520.7 (Jan. 2012), pp. 3043–3047.

[30]   Ludovic Rapp et al. "Smart beam shaping for the deposition of solid polymeric material by laser forward transfer". In: *Applied Physics A* 117.1 (Oct. 2014), pp. 333–339.

[31]   James Shaw Stewart et al. "Red-green-blue polymer light-emitting diode pixels printed by optimized laser-induced forward transfer". In: *Applied Physics Letters* 100.20 (May 2012), p. 203303.

[32]   Ludovic Rapp et al. "Functional multilayered capacitor pixels printed by picosecond laser-induced forward transfer using a smart beam shaping technique". In: *Sensors and Actuators, A: Physical* 224.April 2015 (2015), pp. 111–118.

[33]   Ludovic Rapp et al. "Laser-induced forward transfer of polythiophene-based derivatives for fully polymeric thin film transistors". In: *Organic Electronics* 15.8 (Aug. 2014), pp. 1868–1875.

[34]   A. Pearson et al. "Bubble interactions near a free surface". In: *Engineering Analysis with Boundary Elements* 28.4 (2004), pp. 295–313.

[35]   M. Duocastella et al. "Sessile droplet formation in the laser-induced forward transfer of liquids: A time-resolved imaging study". In: *Thin Solid Films* 518.18 (2010), pp. 5321–5325.

[36]   E Biver et al. "High-speed multi-jets printing using laser forward transfer: Time-resolved study of the ejection dynamics". In: *Optics Express* 22.14 (2014), pp. 17122–17134.

[37]   Christos Boutopoulos et al. "Laser-induced forward transfer of silver nanoparticle ink: Time-resolved imaging of the jetting dynamics and correlation with the printing quality". In: *Microfluidics and Nanofluidics* 16.3 (2014), pp. 493–500.

[38]   J.M. Fernández-Pradas et al. "Laser-induced forward transfer of biomolecules". In: *Thin Solid Films* 453-454 (Apr. 2004), pp. 27–30.

[39]   I. Zergioti et al. "Femtosecond laser microprinting of biomaterials". In: *Applied Physics Letters* 86.16 (Apr. 2005), p. 163902.

[40]   F. Guillemot et al. "High-throughput laser printing of cells and biomaterials for tissue engineering". In: *Acta Biomaterialia* 6.7 (July 2010), pp. 2494–2500.

[41]   Bradley R. Ringeisen et al. "Laser Printing of Pluripotent Embryonal Carcinoma Cells". In: *Tissue Engineering* 10.3-4 (Mar. 2004), pp. 483–491.

[42] C Florian et al. "Conductive silver ink printing through the laser-induced forward transfer technique". In: *Applied Surface Science* 336 (2015), pp. 304–308.

[43] M. Makrygianni et al. "Laser induced forward transfer of Ag nanoparticles ink deposition and characterization". In: *Applied Surface Science* 297 (Apr. 2014), pp. 40–44.

[44] D. Puerto et al. "Single step high-speed printing of continuous silver lines by laser-induced forward transfer". In: *Applied Surface Science* (Nov. 2015).

[45] Matthew S. Brown et al. "Impulsively actuated jets from thin liquid films for high-resolution printing applications". In: *Journal of Fluid Mechanics* 709 (2012), pp. 341–370.

[46] Emre Turkoz et al. "Impulsively Induced Jets from Viscoelastic Films for High-Resolution Printing". In: *Physical Review Letters* 120.7 (2018), p. 074501.

[47] Yoshiki Nakata, Tatsuo Okada, and Mitsuo Maeda. "Nano-sized hollow bump array generated by single femtosecond laser pulse". In: *Japanese Journal of Applied Physics, Part 2: Letters* 42.12 A (2003), pp. 10–13.

[48] Yoshiki Nakata, Noriaki Miyanaga, and Tatsuo Okada. "Effect of pulse width and fluence of femtosecond laser on the size of nanobump array". In: *Applied Surface Science* 253.15 (2007), pp. 6555–6557.

[49] F. Korte, J. Koch, and B.N. Chichkov. "Formation of microbumps and nanojets on gold targets by femtosecond laser pulses". In: *Applied Physics A* 79.4-6 (2004), pp. 879–881.

[50] Joseph P. Moening, Sachin S. Thanawala, and Daniel G. Georgiev. "Formation of high-aspect-ratio protrusions on gold films by localized pulsed laser irradiation". In: *Applied Physics A: Materials Science and Processing* 95.3 (2009), pp. 635–638.

[51] Claudia Unger et al. "Time-resolved studies of femtosecond-laser induced melt dynamics". In: *Optics Express* 20.22 (2012), pp. 24864–24872.

[52] Arseniy I. Kuznetsov et al. "Laser-induced jet formation and droplet ejection from thin metal films". In: *Applied Physics A: Materials Science and Processing* 106.3 (2012), pp. 479–487.

[53] Qingfeng Li et al. "Generating liquid nanojets from copper by dual laser irradiation for ultra-high resolution printing". In: *Optics Express* 25.20 (Oct. 2017), p. 24164.

[54] Arseniy I. Kuznetsov et al. "Laser-induced transfer of metallic nanodroplets for plasmonics and metamaterial applications". In: *Journal of the Optical Society of America B* 26.12 (Dec. 2009), B130.

[55] V. Sametoglu, V. Sauer, and Y. Y. Tsui. "Nanoscale laser-induced forward transfer through patterned Cr films". In: *Applied Physics A: Materials Science and Processing* 110.4 (2013), pp. 823–827.

[56] M. Zenou, A. Sa'ar, and Z. Kotler. "Supersonic laser-induced jetting of aluminum micro-droplets". In: *Applied Physics Letters* 106.18 (May 2015), p. 181905.

[57] M. Colina et al. "Laser-induced forward transfer of liquids: Study of the droplet ejection process". In: *Journal of Applied Physics* 99.8 (2006).

[58] Matthew S. Brown, Nicholas T. Kattamis, and Craig B. Arnold. "Time-resolved study of polyimide absorption layers for blister-actuated laser-induced forward transfer". In: *Journal of Applied Physics* 107.8 (2010).

[59] C Sun et al. "Projection micro-stereolithography using digital micro-mirror dynamic mask". In: *Sensors and Actuators A* 121 (2005), pp. 113–120.

[60] Norihiro Fukuchi et al. "Oblique-Incidence Characteristics of a Parallel-Aligned Nematic-Liquid-Crystal Spatial Light Modulator". In: *Optical Review* 12.5 (Sept. 2005), pp. 372–377.

[61] R. C. Y. Auyeung et al. "Laser forward transfer based on a spatial light modulator". In: *Applied Physics A* 102.1 (2011), pp. 21–26.

[62] Raymond C. Y. Auyeung et al. "Spatially modulated laser pulses for printing electronics". In: *Applied Optics* 54.31 (2015), F70.

[63] Raymond C. Y. Auyeung et al. "Laser forward transfer using structured light". In: *Optics Express* 23.1 (2015), p. 422.

[64] R. Pohl et al. "Solid-phase laser-induced forward transfer of variable shapes using a liquid-crystal spatial light modulator". In: *Applied Physics A: Materials Science and Processing* 120.2 (2015), pp. 427–434.

[65] Marti Duocastella and Craig B. Arnold. "Bessel and annular beams for materials processing". In: *Laser and Photonics Reviews* 6.5 (2012), pp. 607–621.

[66] R Stoian and M Wollenhaupt. *Temporal Pulse Tailoring in Ultrafast Laser Manufacturing Technologies*. 2010, Chapter 5.

[67] R. N. Zare et al. "Control of Chemical Reactions by Control of Chemical Reactions by Feedback-Optimized Phase-Shaped Femtosecond Laser Pulses". In: *Science* 282.5390 (Mar. 1998), pp. 919–922.

[68] A.M. Weiner. "Femtosecond optical pulse shaping and processing". In: *Progress in Quantum Electronics* 19.3 (1995), pp. 161–237.

[69] A. Klini et al. "Laser induced forward transfer of metals by temporally shaped femtosecond laser pulses". In: *Optics Express* 16.15 (July 2008), pp. 11300–11309.

[70] S. Eiselen et al. "The role of temporal energy input in laser micro machining using nanosecond pulses". In: *Physics Procedia* 41 (2013), pp. 683–688.

[71] Sami T Hendow et al. "Percussion drilling of metals using bursts of nanosecond pulses." In: *Optics express* 19.11 (2011), pp. 10221–10231.

[72] Aiko Narazaki et al. "On-demand deposition of functional oxide microdots by double-pulse laser-induced dot transfer". In: *Journal of Laser Micro Nanoengineering* 9.1 (2014), pp. 10–14.

[73] Dao Vu Truong Son et al. "Toward 100 Mega-frames per second: Design of an ultimate ultra-high-speed image sensor". In: *Sensors* 10.1 (2010), pp. 16–35.

[74] M. Duocastella et al. "Jet formation in the laser forward transfer of liquids". In: *Applied Physics A: Materials Science and Processing* 93.2 (2008), pp. 453–456.

[75] D. G. Papazoglou et al. "Shadowgraphic imaging of the sub-ps laser-induced forward transfer process". In: *Applied Physics Letters* 81.9 (2002), pp. 1594–1596.

[76] Matthew S. Brown, Nicholas T. Kattamis, and Craig B. Arnold. "Time-resolved dynamics of laser-induced micro-jets from thin liquid films". In: *Microfluidics and Nanofluidics* 11.2 (2011), pp. 199–207.

[77] Emeric Biver et al. "Multi-jets formation using laser forward transfer". In: *Applied Surface Science* 302 (2014), pp. 153–158.

[78] Maxim V. Shugaev and Nadezhda M. Bulgakova. "Thermodynamic and stress analysis of laser-induced forward transfer of metals". In: *Applied Physics A: Materials Science and Processing* 101.1 (2010), pp. 103–109.

[79] Yuri P. Meshcheryakov et al. "Role of thermal stresses on pulsed laser irradiation of thin films under conditions of microbump formation and nonvaporization forward transfer". In: *Applied Physics A: Materials Science and Processing* 113.2 (2013), pp. 521–529.

[80] N. Seifert, G. Betz, and W. Husinsky. "Droplet formation on metallic surfaces during low-fluence laser irradiation". In: *Applied Surface Science* 103.1 (1996), pp. 63–70.

[81] N. Seifert and G. Betz. "Computer simulations of laser-induced ejection of droplets". In: *Applied Surface Science* 133.3 (1998), pp. 189–194.

[82] David A. Willis and Vicentiu Grosu. "The effect of melting-induced volumetric expansion on initiation of laser-induced forward transfer". In: *Applied Surface Science* 253.10 (2007), pp. 4759–4763.

[83] S I Anisimov et al. "Formation and crystallisation of a liquid jet in a film exposed to a tightly focused laser beam *". In: 47.6 (2017), pp. 509–521.

[84] A M Fox. *Optical Properties of Solids*. Oxford master series in condensed matter physics. Oxford University Press, Oct. 2010.

[85] Dieter Bäuerle. *Laser Processing and Chemistry*. 2011.

[86] X. Gonze et al. "First-principles computation of material properties: The ABINIT software project". In: *Computational Materials Science* 25.3 (2002), pp. 478–492.

[87] P. Balling and J. Schou. "Femtosecond-laser ablation dynamics of dielectrics: Basics and applications for thin films". In: *Reports on Progress in Physics* 76.3 (2013).

[88] L. V. Keldysh. "Ionization in the field of a strong electromagnetic wave". In: *Soviet Physics JETP* 20.5 (1965), pp. 1307–1314.

[89] B. Rethfeld et al. "Timescales in the response of materials to femtosecond laser excitation". In: *Applied Physics A* 79 (2004), pp. 767–769.

[90] An-Chun Tien et al. "Short-Pulse Laser Damage in Transparent Materials as a Function of Pulse Duration". In: *Physical Review Letters* 82.19 (1999), pp. 3883–3886.

[91] Aleksandar D Rakić et al. "Optical properties of metallic films for vertical-cavity optoelectronic devices". In: *Applied Optics Optics* 37.22 (1998), pp. 5271–5283.

[92] J. Hohlfeld et al. "Electron and lattice dynamics following optical excitation of metals". In: *Chemical Physics* 251.1-3 (2000), pp. 237–258.

[93] Sudhanshu Jha. "Interband contribuitions to optical harmonic generation at a metal surface". In: *Physical Review* 153.3 (1967).

[94] Y Siegal et al. "Laser-Induced Phase Transitions in Semiconductors". In: *Annual Review of Materials Science* 25.1 (Aug. 1995), pp. 223–247.

[95] D Von Der Linde, K Sokolowski-Tinten, and J Bialkowski. *Laser-solid interaction in the femtosecond time regime*. Tech. rep. 110. 1997, pp. 1–10.

[96] Laurent J. Lewis and Danny Perez. "Theory and Simulation of Laser Ablation – from Basic Mechanisms to Applications". In: Springer, Berlin, Heidelberg, 2010, pp. 35–61.

[97] S.I. Anisimov, B.L. Kapeliovich, and T.L. Perel-man. "Electron emission from metal surfaces exposed to ultrashort laser pulses". In: *Journal of Experimental and Theoretical Physics* 66 (1974), pp. 375–377.

[98] ASTM International. *ASTM E438-92 (2018) Standard Specification for Glasses in Laboratory Apparatus*. 2018.

[99] Marc J. Assael et al. "Reference data for the density and viscosity of liquid copper and liquid tin". In: *Journal of Physical and Chemical Reference Data* 39.3 (2010), pp. 1–8.

[100] Claus Cagran. *Thermal conductivity and thermal diffusivity of liquid copper*. Institut fur Experimentalphysik, Technische Universitat Graz, 2000.

[101] Michalis N. Zervas and Christophe A. Codemard. "High Power Fiber Lasers: A Review". In: *IEEE Journal of Selected Topics in Quantum Electronics* 20.5 (2014), pp. 219–241.

[102] E. Snitzer et al. "Double clad, offset core Nd fiber laser". In: *Optical Fiber Sensors* 2 (1988), PD5.

[103] A Agnesi, M Fogliani, and G C Reali. "Theory and experiments of passive negative feedback pulse control in active / passive mode-locked solid-state lasers. In: Modeling and Simulation of Laser Systems II 1415 (1991), pp. 242–247.

[104] M J Liu. "Simple technique for measurements of pulsed Gaussian-beam spot sizes". In: *Optics letters* 7.5 (1982), pp. 196–198.

[105] Tobias C. Röder and Jürgen R. Köhler. "Physical model for the laser induced forward transfer process". In: *Applied Physics Letters* 100.7 (2012), pp. 2012–2015.

[106] Q. Li et al. "Quantitative-phase microscopy of nanosecond laser-induced micro-modifications inside silicon". In: *Applied Optics* (2016).

[107] Qingfeng Li et al. "Laser-induced nano-jetting behaviors of liquid metals". In: *Applied Physics A: Materials Science and Processing* 123.11 (2017), p. 0.

[108] Aiko Narazaki et al. "Nano- and microdot array formation by laser-induced dot transfer". In: *Applied Surface Science* 255.24 (2009), pp. 9703–9706.

[109] Norman Chigier and Rolf D Reitz. "Regimes of jet breakup and breakup mechanisms (physical aspects)". In: *Recent advances in spray combustion: spray atomization and droplet burning phenomena* 166 (1995), pp. 109–136.

[110] L. Battezzati and a.L. Greer. "The viscosity of liquid metals and alloys". In: *Acta Metallurgica* 37.7 (1989), pp. 1791–1802.

[111] Dirkjan B. van Dam and Christophe Le Clerc. "Experimental study of the impact of an ink-jet printed droplet on a solid substrate". In: *Physics of Fluids* 16.9 (2004), pp. 3403–3414.

[112] Jens Eggers. "Nonlinear dynamics and breakup of free-surface flows". In: *Reviews of Modern Physics* 69.3 (1997), pp. 865–929.

[113] Pradeep P. Bhat et al. "Formation of beads-on-a-string structures during break-up of viscoelastic filaments". In: *Nature Physics* 6.8 (2010), pp. 625–631.

[114] Claudia Unger et al. "Time-resolved imaging of hydrogel printing via laser-induced forward transfer". In: *Applied Physics A: Materials Science and Processing* 103.2 (2011), pp. 271–277.

[115] Emeric Bourasseau et al. "Calculation of the surface tension of liquid copper from atomistic Monte Carlo simulations To cite this version : Calculation of the surface tension of liquid copper from atomistic Monte Carlo simulations ." In: *European physical Journal B: condensed matter and complex systems* 86 (2013), p. 251.

[116] Y. Nakata et al. "Solid-liquid-solid process for forming free-standing gold nanowhisker superlattice by interfering femtosecond laser irradiation". In: *Applied Surface Science* 274 (2013), pp. 27–32.

[117] A. A. Kuchmizhak et al. "Plasmon-mediated Enhancement of Rhodamine 6G Spontaneous Emission on Laser-spalled Nanotextures". In: *Physics Procedia* 86.June 2015 (2017), pp. 66–71.

[118] Dirk Wortmann et al. "Experimental and theoretical investigation on fs-laser-induced nanostructure formation on thin gold films". In: *Journal of Laser Applications* 24.4 (2012), p. 042017.

[119] Nail A. Inogamov et al. "Solitary Nanostructures Produced by Ultrashort Laser Pulse". In: *Nanoscale Research Letters* 11.1 (2016), p. 177.

[120] N. A. Inogamov, V. V. Zhakhovskii, and V. A. Khokhlov. "Jet formation in spallation of metal film from substrate under action of femtosecond laser pulse". In: *Journal of Experimental and Theoretical Physics* 120.1 (2015), pp. 15–48.

[121] Ivan Egry, Georg Lohoefer, and Gerd Jacobs. "Surface tension of liquid metals: Results from measurements on ground and in space". In: *Physical Review Letters* 75.22 (1995), pp. 4043–4046.

[122] Yuya Baba et al. "Thermal conductivity measurement of molten copper using an electromagnetic levitator superimposed with a static magnetic field". In: *Measurement Science and Technology* 23.4 (2012), p. 045103.

[123] Juan J. Valencia and Peter N. Quested. "Thermophysical Properties". In: *ASM Hadbook, Volume 15: Casting* 15.1981 (2011), pp. 468–481.

[124] Kikuo Ujihara. "Reflectivity of metals at high temperatures". In: *Journal of Applied Physics* 43.5 (1972), pp. 2376–2383.

[125] W Bendick and W Pepperhoff. "The heat capacity of Ti, V and Cr". In: 12 (1982), pp. 1085–1090.

[126] D. P. Jackson. "Approximate calculation of surface Debye temperatures". In: *Surface Science* 43.2 (1974), pp. 431–440.

[127] Patrick K. Notz and Osman A. Basaran. "Dynamics and breakup of a contracting liquid filament". In: *Journal of Fluid Mechanics* 512 (2004), pp. 223–256.

[128] Urs Zywietz et al. "Generation and patterning of Si nanoparticles by femtosecond laser pulses". In: *Applied Physics A* 114.1 (Jan. 2014), pp. 45–50.

[129] Michael Moseler and Uzi Landman. "Formation, stability, and breakup of nanojets". In: *Science* 289.August (2000), pp. 1165–1169.

[130] Jens Eggers. "Dynamics of Liquid Nanojets". In: *Physical Review Letters* 89.8 (2002), p. 084502.

[131] W. Sparreboom, A. Van Den Berg, and J. C.T. Eijkel. "Principles and applications of nanofluidic transport". In: *Nature Nanotechnology* 4.11 (2009), pp. 713–720.

[132] Benjamin W. Zeff et al. "Singularity dynamics in curvature collapse and jet eruption on a fluid surface". In: *Nature* 403.6768 (2000), pp. 401–404.

[133] Yoshiyuki Tagawa et al. "Highly Focused Supersonic Microjets". In: *Physical Review X* 2.3 (July 2012), p. 031002.

[134] Ivo R. Peters et al. "Highly focused supersonic microjets: Numerical simulations". In: *Journal of Fluid Mechanics* 719 (2013), pp. 587–605.

[135] Emre Turkoz et al. "Subthreshold laser jetting via flow-focusing in laser-induced forward transfer". In: *Physical Review Fluids* 3 (2018), p. 82201.